Planetary and Space Science

Equatorial grooves distribution on Ganymede: length and self-similar clustering analysis

--Manuscript Draft--

Manuscript Number:	PSS_2020_130R1
Article Type:	Research Paper
Keywords:	Satellites, surfaces; Tectonics; geological processes; Ganymede; Jupiter, satellites
Corresponding Author:	Alice Lucchetti INAF - OAPD Astronomical Observatory of Padova Padova, Italy
First Author:	Alice Lucchetti
Order of Authors:	Alice Lucchetti
	Costanza Rossi
	Francesco Mazzarini
	Maurizio Pajola
	Riccardo Pozzobon
	Matteo Massironi
	Gabriele Cremonese
Abstract:	Grooves represent the evidence of tectonic activity that deformed Ganymede surface during its geologic evolution. In this work, we investigate the main characteristics of Ganymede's grooves populations on four different areas located at the equatorial region of the satellite (Uruk Sulcus, Babylon Sulci, Phrygia Sulcus and Mysia Sulci). Specifically, we analyse i) the grooves length distribution to provide a framework for their evolution and ii) the grooves self-similar clustering to infer their vertical penetration inside Ganymede icy shell. For each dataset, we find that the grooves distribution is well fitted by an exponential-law and a power-law distribution depending on the structure length. This implies the presence of confined structures in a shallow layer of the icy crust (relatively shorter, exponentially-fitted structures) and crustal-scale structures that could theoretically reach the crust-ocean interface (relatively longer, power law-fitted structures). In addition, the existence of two exponential distributions for few datasets suggest that there could be two differently systems of structure confined within specific mechanical crust layers. The thickness of the penetrated icy shell is retrieved through the self-similar clustering analysis and ranges between 105 and 130 km for the examined datasets. This value agrees with independent estimates of the icy shell thickness, ranging between 80 and 150 km. Moreover, our results support the hypothesis that a large number of grooves penetrate the brittle icy crust, with sets of fractures vertically confined in different mechanical layers, while the penetration of few interconnected faults underlying longer grooves may interest the whole icy crust above the liquid ocean.
Suggested Reviewers:	Paola Cianfarra paola.cianfarra@unige.it She is expert of the topic developed in this work
	Ernst Hauber Ernst.Hauber@dlr.de
	Chloe Beddingfield chloe.b.beddingfield@nasa.gov
	August Gudmundsson August.Gudmundsson@rhul.ac.uk
	Akos Kereszturi kereszturiakos@gmail.com

Opposed Reviewers:	Geoffrey Collins gcollins@wheatoncollege.edu conflict of interest
	William McKinnon mckinnon@wustl.edu conflict of interest
	Samuel Howell samuel.m.howell@jpl.nasa.gov conflict of interest
Response to Reviewers:	Reviewer #1: General comments The work is presenting new results on the analysis of grooves on the surface of Ganymede in order to estimate the subsurface rheological characteristics of the satellite. It presents new and interesting results, worth for publishing, especially it is closely connected to the JUICE mission main target. The structure of the manuscript is good, the language is OK, the illustration is also good. However before the acceptance several small aspects should be improved, thus the referee suggests moderate revision. We thank the referee for the positive and constructive revision. We answered below to the major points raised by the referee and we modified the manuscript accordingly to the suggestions. The main general comments are: · The authors argue that the statistical analysis of the grooves might provide information on the depth of the subsurface ocean, what is true, however they do not give such an estimation. Probably the results are not enough to make such an estimation however some argumentation on it, at least as a minimal or scale of depth would be useful, including its comparison to other estimations in the discussion section. With the fractal method we can infer the thickness at which grooves penetrated in the icy layer and, hence, provide the thickness variability of the crust of Ganymede. What the reviewer suggests makes sense considering that the derived crust thickness most likely coincides with the depth of the interface with the liquid ocean. This is also supported by previous measurements: (i) Kivelson et al., (2002) suggested the presence of a conducting layer at a depth of 150 km below the icy crust from interpretation of Galileo magnetic data. Moreover, Saur et al., (2015) stated the presence of a saline conductive ocean at a depth of 150 km. On the other hand, Schenk et al., (2002) provides an estimate of at least 80 km for the icy shell thickness by analysing the transition between depth to diameter ratio of large impact craters. This means that from our results, we expect a global ocean located at 105-130 km depth depending on the area of the satellite considered. We expanded the text in order to describe in greater details our findings. · It would be more favourable if they implement just sentences on the expected real behaviour or route of the subsurface of the faults. From the Earth we know that very deep penetrating faults became less tilted relatively to the vertical along with the increasing depth (like listric faults), or they might transit gradually from a sharp fault to a plastic deformation zone, or they might even split to more faults etc. Some short discussion on these aspects would be appreciated in the revised version. For example at 413 line and at other locations. The vertical profile of the grooves is expected to behave similarly to the Earth faults that become less tilted with the increase of the depth. Indeed, faults gradually transit from sharp geometries to gentle ones when plastic deformation zones are reached at depth. Grooves are suggested to be originated by extension and strike-slip regimes that imply different development at depth. On Earth and, hence, on the icy crust of Ganymede, extensional deformation originates faults with high dip (ideally 60°) that can decrease up to sub-horizontal geometries (listric faults, e.g. Walsh and Watterson, 1991). On the other hand, strike-slip activity form nearly vertical faults that reach high depths (e.g. Fossen, 2016). In this context, we suggest that the strike-slip grooves represent the faults that penetrate deeper and follow the power-law behavior described by our analyses, by potentially reaching the bottom of the icy crust; while the

extensional grooves are represented by the shorter faults with exponential behavior, which remain at the top layers of the icy crust. It is possible that some of them could assume listric shape at the occurrence of ductile layers and cease to vertically develop at depth. It is appropriate to clearly state that some extensional grooves may show a power-law behavior and penetrate at high depth, and, vice-versa, some strike-slip faults can show exponential behavior by reaching shallow depths.
We added these sentences in the manuscript, as suggested.

· The temporal aspect was not mentioned in the work, something about the relative or absolute age of these groove systems and their relation to the geological history of Ganymede would be useful, as if a hypothetic ocean depth would be estimated, it should be representative for the given period.
Time evolution cannot be retrieved by using self-similar clustering, indeed the actual fracture network shows a fractal behaviour consistent with an actual mechanical stratigraphy (derived by analyzing the cut-offs of the Dlog(C(l))-Dlog(l) spectrum). Hypothetically, we may forward that the main initial deformation of the crust occurred via large faults cutting across the whole crust thickness down to the crust-ocean transition. With time, minor deformation provided the development of exponential distribution of fault cutting across the crust down to the brittle-ductile transition. This can be envisaged for data sets presenting two exponential populations of grooves. In Uruk Sulcus area, we have no means for separating the large power-law fault system from the one with exponential behaviour, being likely that major faults cut across all the crust and minor faults only the brittle layer. In this way, we can assume that the longer grooves, candidates to the penetration of the icy crust, are relatively older than the minor ones. These latter may be originated at a later stage due to the activity of the main ones.
We added these sentences in the manuscript, as suggested by the referee.

· Some further references are needed for better context:
o around 40-41 lines please cite:<https://ui.adsabs.harvard.edu/abs/2015epl..book.....H/abstract>
o also put some sentences to the Introduction section on Europa (for example after the first paragraph), mentioning that magnetic field based ocean observation also happened there:<https://ui.adsabs.harvard.edu/abs/2019NatAs...3..401G/abstract> , the surface tectonic (<https://ui.adsabs.harvard.edu/abs/2013P%26SS...77...74K/abstract>) and crater structures' parameters also indicate the depth of the ocean on Europe (<https://ui.adsabs.harvard.edu/abs/2002Natur.417..419S/abstract> ,<https://ui.adsabs.harvard.edu/abs/2017JGRE..122.2685S/abstract>)
o also mentioned in the introduction that astrobiology relevance also has the supposed ocean:<https://ui.adsabs.harvard.edu/abs/2016AsBio..16..561D/abstract>
We added a sentence in the conclusion in order to consider Europa as a future target on which we can apply our methodology due to its liquid ocean. Hence, we report also the references suggested by the referee in the conclusion section and in the reference list.

Specific comments

109-11 lines
please clearly define what is the length of a lineament in the case of several interconnecting or crossing, splitting lineaments
The lineament length is the length of a detected linear feature. If the lineament abuts or is cut by other lineaments, the length of each segment is measured. The large number of lineaments reduces the effect on the analyzed data populations of a possible lineament segmentation.

112 line
"different relative age have been identified"
would it be better to write about „relative age domains or groups"
We modified the sentence as suggested.

115-116 lines
"The local scale provides spacing between the structures < 5 km and length < 50 km"
please rewrite or explain more clearly this sentence

	We rewrite the sentence as follows: “The local scale allows the identification of structures spacing < 5 km and length < 50 km..” 128-129 lines “thanks to the luminosity contrast resulting from the solar lighting conditions” do you mean shadow effect? Yes, the Ganymede map is composed of images with different illuminations condition, hence only where there is enough luminosity contrast it is possible to identify and map these structures. 133 line „The four datasets are in selected regions” consider to modify to „The four datasets are located in selected regions” We have modified the sentence accordingly. 152 line “identified grooves structures” consider to modify to „identified groove structures” Done. 255 line „does not show a regular and wide plateau” please indicate where are these visible in the diagrams, as might not be evident for all readers We report and explain later in the paper the identification of the plateau in the datasets analysed. 250 line „the better the computation of the power-law” consider to modify to „the better the computation is of the power-law” We modified the sentence as follows: “when the range is wider, the computation of the power-law distribution is better” 265 line „The minimum and maximum” please explain somewhere (maybe in the Methods section) how the minimum was measured, as for smaller lineaments are difficult to identify The minimum is the value of the shortest lineament length identified in the mapping. This value is higher than the resolution of the image, hence, the value is reliable. 266-269 line please consider to put these numbers to a table The numbers have been reported in Table 1 under the l range (km) column. 285 line „confined within specific mechanical layers in the crust” please provide a bit more detailed characterization of this „specific mechanical layer” We rephrase the sentence as follows: “layers in the crust with different mechanical properties”. 288-289 line “existence of two exponential distributions for three datasets suggest that there could be two differently confined structure systems within specific mechanical crust layers.” please consider to indicate this in the abstract too We added the statement in the abstract. 306 line “Cowie et al., 1994;” do not use italic Done. 307-308 lines „the interaction of fractures and the following linkage/growth process overcomes the nucleation of new faults (Cowie et al., 1995).”

	difficult to understand, consider reformulating We reformulate the sentence as follows: “On the contrary, the interaction of fractures and the consequent linkage/growth process dominates over the nucleation of new faults providing a power-law distribution (Cowie et al., 1995).” Table 1 1 line 3 column give some very brief explanation for the “0.47” value – it is very small relatively to the values in the other lines It is due to the higher image resolution of the Uruk Sulcus area that allows the identification of shorter lineaments. 322 line “are defined for each histogram plot.” please modify to “are defined for each histogram plot (with red text).” We modified as follows to be as complete as possible: “are defined for each histogram plot and outlined by green, blue, red and orange lines, respectively” 359 line “and required for the development of densely populated grooves at the surface.” OK, but please explain briefly why We reworded the sentence “Moreover, this suggests that this limit might be the potential thickness of the icy crust located above the deep ocean that during a phase of intense deformation and high strain rates may be cut across by very large faults”. 364 line „plateau stage of the local slope curve (green points)” please indicate in the figure, what if somebody prints in black and white We modified the Figure accordingly. 367 line „The breaking point corresponds” could you indicate these points with arrow We displayed the breaking point with the gray stripe in Figure 8. The dot line centered in the grey stripe corresponds to the breaking point. It is better this type of representation in order to consider the associated error, too. 370 line „all grooves system analysed” consider to modify to „all groove systems analysed” We modified it. 375 line „and Uco, the upper” please delete the comma Done. 377 line „reaching this maximum depth” please specify which depth, where was this mentioned before We modified as follows: “reaching this maximum depth (identified as Uco)” 381 line „by a hierarchical fracture network” please also explain briefly this A hierarchical fracture network means that we have first and second order structures. We reported it in the text. 391 line „necking instability” please explain We added after necking instability the following statement: “(i.e. modelling Ganymede's lithosphere as a brittle surface layer underlain by a viscous half-space)”.

	392 line „10-4 s-1 strain rate,” please give some explanation, what this value represents or give some context, is it large or small, relatively to what etc. We reported a wrong value, the right ones is 10^-13. We corrected it in the text, however this is the value that it is usually assumed in modelling and reported from literature. 424 line „fitted by exponential length distribution” some words would be useful for explanation If the referee agrees, we prefer to keep this sentence since the overall explanation is reported in the discussion section. 425 line „the occurrence of a” is the „a” necessary? We deleted it. 430 line „analysed length” consider to modify to „analysed the length” We added it. 432 line „grooves populations” consider to modify to „groove populations” We modified it. 434 line „the Ganymede surface” consider to modify to „the surface of Ganymede” We modified it. 437 line „are selected” consider to modify to „are from selected” We modified it. 439 line „grooves, respectively” please complete by at how large (km2) total surface area were these identified The total surface area considered for the different four dataset is 1000km x 500km, but, if the referee agrees, we do not insert this information in the manuscript since it is not important for the conclusion. 448 line „reaching the crust-ocean interface” please discuss the above listed aspect (general comments) as curving, banding, diverging, transition to deformation etc. of fault lines along with the increasing depth We discussed it as suggested in the general comments. We added few sentences, as reported in the answer to major points. 452 line „different mechanical layers” consider to modify to „layers with different mechanical properties” We modified it. 460 line please discuss the possible depth of the ocean or its scale based on your results The possible depth coincides with the estimates of the icy shell thickness. To be as complete as possible, we added in the text icy crust above the liquid ocean in order to state that the found thickness corresponds to the depth at which the liquid ocean is located.

Figure 3 and 4
please consider to improve the readability of the labelling of different units at the bottom of the images, and also consider to make them more readable for black and white printed version
We modified the figure accordingly.

Reviewer #2: Interesting manuscript. Suggest minor revision before acceptance and final publication.

We thank the referee for the very valuable and constructive revision. We modified the manuscript accordingly satisfying all the requests made in the referee pdf file. Below, we answered to the major points and modify the text accordingly.

Some minor point to discuss:

-Are grooves brittle tectonic structures of the icy crust of Ganymede? Please discuss this point into the text and then use throughout the manuscript the same terminology. In fact, grooves / faults /fractures /faults underlying grooves are used as synonyms.
We reported in the Introduction section the following definition: “Grooves are the manifestation of brittle deformation of the light terrain (i.e. faults).”
Since grooves are the surface expression of brittle deformation we refer to them as faults in the manuscript and we modified it accordingly.
In the method section, we keep the terminology “fracture” referring to the National Research Council, 1996 definition.

- Do the Authors think the entire icy crust of Ganymede deforms/deformed in a brittle fashion? Discuss this point into the manuscript.
In our case we can have also a ductile ice layer that could behave as the brittle one depending on pressure and temperature. For this reason, we prefer to maintain the generic icy crust in the text because it could interest both brittle and ductile layers (since there is not yet a comprehensive understanding of the ice behavior on these bodies).
We expect that Ganymede icy crust behaves following the rheological distribution of the internal layering at depth that includes both brittle and ductile fashions. Similarly to the Earth crust, it is expected that a brittle-ductile transition occur on Ganymede icy crust. However, its location is still unknow although authors suggested it lies at 2-3 km at depth at the time of deformation (Nimmo and Pappalardo, 2004). The self-similar clustering considers the crust involved by fault/fracture penetration. In this way, both the behaviors (brittle and ductile) are included. The brittle portion is expected wider than the ductile portion, which also can be crosscut by vertical development of grooves.

- try to better explain why the upper cutoff limit of the power law distribution of the mapped grooves should represent the crustal thickness of the icy crust.
We rephrased the sentence regarding this concept as follows:
Indeed, it has been validated that the fractal clustering is controlled by the mechanical layering of the crust as observed for earthquakes and for fault networks at basin and plate scales (Pacheco et al., 1992; Davy, 1993; Ouillon et al., 1996). Moreover, it has been observed that the thickness of the fractured/deformed layer scales as the upper cut off value (Uco) characterizing the fracture network spatial organization (Mazzarini and D’Orazio, 2003; Mazzarini and Isola, 2010; Mazzarini et al., 2013).

-Even if I am not an English mother tongue I sometimes find the writing is a lit bit cumbersome. Please check English with a mother tongue colleague/specialist.
We checked the English with a mother tongue colleague to improve the writing.

-Some suggestions are provided to improve figs 2, 3, 4 5.
We modified and improved the Figures, as suggested by the referee.

-Carefully cross check cited reference and reference lists
We modified and corrected the reference list as suggested.

	-Consider preparing a sketch to better explain the self similar clustering analysis to readers not familiar with this kind of quantitative (and effective!) approach. We added the Figure 6, as suggested by the referee, to better explain the meaning of the fractal exponent. -In the current form the conclusions are a short summary of the work. I think that in this chapter the Authors should present the main results and discuss the implication of these results for the wider audience. We added sentences in the discussion and modified the conclusion paragraph according to the referee's suggestion reported in the referee pdf file. Other comments are in the annotated pdf manuscript. All the best!

Equatorial grooves distribution on Ganymede: length and self-similar clustering analysis

A. Lucchetti[1], C. Rossi[2], F. Mazzarini[3], M. Pajola[1], R. Pozzobon[4], M. Massironi[4], G. Cremonese[1]

[1]INAF-Astronomical Observatory of Padova, Padova, Italy (alice.lucchetti@inaf.it); [2]INFN - Laboratori Nazionali di Frascati, Frascati (Roma), Italy; [3]INGV- National Institute of Geophysics and Volcanology, Pisa, Italy; [4] Geoscience Department, University of Padova, Padova, Italy.

Abstract

Grooves represent the evidence of tectonic activity that deformed Ganymede surface during its geologic evolution. In this work, we investigate the main characteristics of Ganymede's grooves populations on four different areas located at the equatorial region of the satellite (Uruk Sulcus, Babylon Sulci, Phrygia Sulcus and Mysia Sulci). Specifically, we analyse i) the grooves length distribution to provide a framework for their evolution and ii) the grooves self-similar clustering to infer their vertical penetration inside Ganymede icy shell. For each dataset, we find that the grooves distribution is well fitted by an exponential-law and a power-law distribution depending on the structure length. This implies the presence of confined structures in a shallow layer of the icy crust (**relatively** shorter, exponentially-fitted structures) and crustal-scale structures that could theoretically reach the crust-ocean interface (**relatively longer**, power law-fitted structures). **In addition, the existence of two exponential distributions for few datasets suggest that there could be two differently systems of structure confined within specific mechanical crust layers.**

The thickness of the penetrated icy shell is retrieved through the self-similar clustering analysis and ranges between 105 and 130 km for the examined datasets. This value agrees with independent estimates of the icy shell thickness, ranging between 80 and 150 km. Moreover, our results support the hypothesis that a large number of grooves penetrate the brittle icy crust, with sets of fractures

vertically confined in different mechanical layers, while the penetration of few interconnected faults underlying longer grooves may interest the whole icy crust above the liquid ocean.

1. Introduction

Ganymede is the largest of the four Jupiter's satellites with a diameter ~5262 km (Anderson et al., 2001). Its unique characteristics were first investigated by two flybys of Voyager 1 and 2 in 1979 (Smith et al., 1979a, 1979b) and subsequently, by the remote sensing instruments onboard Galileo between 1995 and 2003 (Russell et al., 2012). Ganymede was found to be the only solid body in the outer Solar System that owns an internal dynamo field (Kivelson et al., 1997). Moreover, it was discovered that Ganymede hosts a subsurface ocean (Kivelson et al., 2002). The thickness of the differentiated layers of the satellite's interior is still under investigation, even if the outer icy crust above the liquid ocean has been suggested to be 120-170 km thick (Kivelson et al., 2002; Sohl et al., 2002; Hussmann et al., 2007; Kuskov, **2010;** Saur et al., 2015). **The implication coming from the presence of an ocean are important for the evolution of the satellite, the tectonic activity shaping its surface and the stress mechanisms acting on it.**

The uniqueness of this satellite was also revealed by its surface **features**. Indeed, Ganymede's surface is subdivided into two geological domains distinguishable by albedo, morphology and crater density: dark and light terrains (Smith et al., 1979a, 1979b; Shoemaker et al. 1982; Pappalardo et al., 2004; Patterson et al., 2010; Collins et al., 2013, **Hargitai & Kereszturi, 2015**). The heavily cratered dark terrain covers 35% of the surface of the satellite (Shoemaker et al., 1982; Murchie et al., 1986, 1989; Neukum, 1997; Neukum et al., 1998; Prockter et al., 1998; Zahnle et al., 2003; Schenk et al., 2004) and it is characterized by large-scale, arcuate fracture systems termed furrows, that have been hypothesized to be the remnants of former multiring basins (McKinnon & Melosh, 1980; Murchie et al., 1990; Prockter et al., 1998; Schenk & McKinnon, 1987, **Hirata et al., 2020**). A thin **low albedo** deposit overlying the bright icy material may be responsible for the darkness of the terrain (Casacchia and Strom, 1984; Croft and Strom, 1985, Allison and Clifford, 1987; Figueredo et al., 1999; Moore

et al., 1999; Prockter et al., 2000), that is estimated to be > 4 Gyr old (Zahnle et al., 2003). The remaining 65% of the surface is covered by bright terrains which are less densely cratered, younger, heavily tectonized and mainly constituted by longitudinal swaths termed "Sulci" and polygons several tens of kilometers across (Lucchitta, 1980; Patterson et al., 2010). The light terrain may have been emplaced between 2 Gyr or even up to 4 Gyr ago, depending on the cratering model chronology used (Zahnle et al., 2003), and it is characterized by the presence of linear features called grooves (Murchie et al., 1986; Pappalardo et al., 1998; Prockter et al., 2000; Collins, 2009). Grooves are regional-scale morphotectonic structures, from linear to curvilinear, **that represent the manifestation of brittle deformation of the light terrain (i.e. fractures and faults)** (Lucchitta, 1980; Bianchi et al., 1986; Pappalardo & Greeley, 1995; Pappalardo et al., 1998, 2004). The proposed tectonic processes responsible for the groove formation include extension, e.g. horst-and-graben normal faulting pulling the terrain apart (Shoemaker et al., 1982; Belton et al., 1996, Pappalardo et al., 1998; Dombard and McKinnon, 2001; Bland and Showman, 2007), and strike-slip kinematics (e.g. Pappalardo et al., 1998, Cameron et al., 2018). In addition to these processes, local resurfacing by tectonism (Head et al., 2002) and cryovolcanic flows (Schenk and McKinnon., 2001; Showman et al., 2004) may contribute to the actual groove morphology.

Grooves represent the evidence of tectonic activity that deformed the satellite surface during its geologic evolution and may have played a key role in the possible connection between surface and the subsurface ocean (Head et al., 2002). In this context, the analysis of Ganymede deformed surface could provide hints regarding its interior, as well as its ice shell's mechanical behaviour. **Hereafter**, **since grooves are the surface expression of brittle deformation, we refer to them as faults.** Indeed, faults distribution and fault populations on icy satellites can reveal insights into the evolution of their surface that cannot be gained with other techniques. In particular, statistical characterization of fault-population attributes, such as length and **spatial** clustering, are fundamental means to explore deformation rates, stress transmission modes, rheology of the medium, and mechanical layering (Benedicto et al. 2003; Soliva and Schultz, 2008; Gudmundsson et al. 2010, Gudmundsson et al.,

2011; Schultz et al. 2010; Gudmundsson et al. 2013). The fractal analysis has been used in terrestrial planets studies to **infer** the thickness of the fractured crust (e.g., Mazzarini and D' Orazio, 2003; Mazzarini, 2004; Soliva and Schultz, 2008; Mazzarini and Isola, 2010; Pozzobon et al. 2015). In the same fashion, on icy satellites the exploration of the depth at which fractures penetrate the icy layer could be constrained investigating the main characteristics of fault populations, such as length size-distribution and clustering (Lucchetti et al., 2017).

In this work, we analyse the **the faults' length (i.e. the grooves' length)** and spatial distribution (Bonnet et al., 2001; Bour et al., 1999; Bour et al., 2002 ; Gudmundsson et al., 2013) to estimate the potential thickness of the icy crust above the deep ocean required to develop densely populated structures at the surface of Ganymede (i.e. the grooves). After analysing the global **faults** distribution, we investigate the behaviour of four regions located on the equatorial area of the satellite. Then, we analyse the **faults** length distribution and self-similar **spatial** clustering providing the vertical extension of **faults** penetration inside Ganymede icy shell.

2. Dataset

Ganymede imagery coverage comes from the data acquired by both the Wide Angle Camera (WAC) and Narrow Angle Camera (NAC) onboard Voyager 1 and 2 and the Solid State Imaging (SSI, Belton et al., 1992) camera onboard Galileo spacecraft. Specifically, the subjovian hemisphere was imaged by Voyager 1 with a resolution up to 1 km/px, while the antijovian hemisphere was imaged by Voyager 2 with a resolution up to 500 m/px. The leading and trailing hemisphere were imaged with a resolution of 2 km/px and 3.6 km/px respectively by distant encounters of Ganymede during the Galileo Jupiter tour to fill the Voyager coverage gaps (Carr et al., 1995). In addition, the six Galileo close encounters with Ganymede allowed the acquisition of high-resolution images (100 m/px and **higher**) by the SSI camera. Based on these remote sensing data, the United States Geological Survey (USGS) Astrogeology Science Centre assembled a global image mosaic of the surface resampled at 1 km/px (Becker et al., 2001, Figure 1). The map was derived combining reasonable input resolution

images (from 20 km/px for gap fill to approximately 400 m/px) and works for the global mapping of grooves.

Ganymede grooves **(faults)** are located on four different types of light material units (Collins et al., 2013): light irregular material, light subdued material, light grooved material and undivided light material (Figure 1). The light irregular material exhibits a mixture of both smooth and grooved surfaces with a relatively high to moderate albedo and it is characterized by grooves with irregular orientation and spacing (Collins et al., 2013). The light subdued material is thought to be representative of the early stage grooved terrain formation, hence displaying smooth surface and faint lineaments with similar spacing and orientations (Collins et al., 2013). The light grooved material likely formed through the modification and deformation of pre-existing materials, such as the light subdued material or dark terrain and it is mainly characterized by similarly spaced and oriented areas of closely packed troughs and lineaments. Finally, the light undivided material is identified when the other three terrains cannot be discerned (Collins et al., 2013). Three different relative age **domains** have been identified for each light terrain, except for the undivided light terrain (Patterson et al., 2010; Collins et al., 2013).

Grooved terrains represent the deformation of Ganymede's light terrains: they exhibit two superposed scales of grooves with different structure**,** spacing and length (Patterson et al., 2010). **The local scale allows the identification of structures spacing < 5 km and length < 50 km**, while grooves identified at the regional scale are usually clustered in sets of grooves with length > 100 km and average spacing of about 10 km, often displaying parallel ordered patterns (Bianchi et al., 1984; Casacchia & Strom, 1984; Collins et al., 2000, 2013; Lucchitta, 1980; Pappalardo et al., 1998, 2004; Pappalardo & Greeley, 1995; Patterson et al., 2010).

Our analysis is based on the regional scale grooves mapping (Rossi et al., 2020) that represents a useful dataset to improve the knowledge of the tectonic evolution of the satellite and to recognize the main characteristics of these features (Figure 1). In particular, grooves on Ganymede were manually mapped on the global image mosaic (Becker et al., 2001) between 60°N and 60°S and

digitized in a geographic information system (GIS) geodatabase (Rossi et al., 2020). Due to the limitation of illumination and resolution conditions of the Ganymede mosaic, grooves were mapped on approximately 36% of the light terrain. As reported in Rossi et al., (2020), mapped grooves are considered as the topographic expression of trough structures recognizing their bottom thanks to the luminosity contrast resulting from the solar lighting conditions.

Thanks to these comprehensive grooves mapping dataset, we were able to select four different type-regions located on the equatorial belt of Ganymede. The choice is based on the high density and homogeneous spatial distribution of the grooves located on those regions, which is necessary for the following analysis. The four datasets **are located** in selected regions in Uruk Sulcus, Babylon Sulci, Phrygia Sulcus and Mysia Sulci, respectively (Figure 2-5). Uruk Sulcus is centered at 0.8°N, 200°E, and exhibits different intersecting bands of light units characterized by various tectonism mechanisms, such as normal faulting, graben, domino-style faulting (Pappalardo et al., 1998; Cameron et al., 2018) and transpressional strike-slip faulting (Rossi et al., 2018). The number of grooves of the selected area is 1068 (Figure 2). The area selected in Babylon Sulci is centered at 0°N, 290°E, as shown in Figure 3, and it **includes** 882 grooves. Babylon Sulci has been inferred as an example of strike-slip setting, where grooves super-system delineates longer and sub-parallel grooves that enclose shorter grooves with different directions (Rossi et al., 2020). A similar regional setting is found in Phrygia Sulcus. Here, **the study area was centered** at 15°N, 355°E and **includes** 678 grooves (Figure 4). Finally, the fourth dataset is located in Mysia Sulci and centered at 7°N, 20°E and it is constituted by 987 grooves (Figure 5).

Figure 1: A-B) Orthographic projection of the global image mosaic of Ganymede centered at 0°N, 0°E and at 0°N, 180°E, respectively (available at https://astrogeology.usgs.gov). C-D) The orthographic projection of the Collins et al. (2013) published global geological map of Ganymede. The legend refers to the light terrain units where grooves were mapped: light subdued unit (*ls1, ls2, ls3*), light irregular unit (*li1, li2, li3*), light grooved unit (*lg1, lg2, lg3*) and light undivided unit (*l*) (Collins et al., 2013). E-F) The orthographic projection of the mapped grooves performed on Ganymede image mosaic by Rossi et al., (2020). The total number of identified **groove** structures (in orange) is 14,707 between 60°N and 60°S region. All maps report the Sulci names of the selected regions used in our analysis.

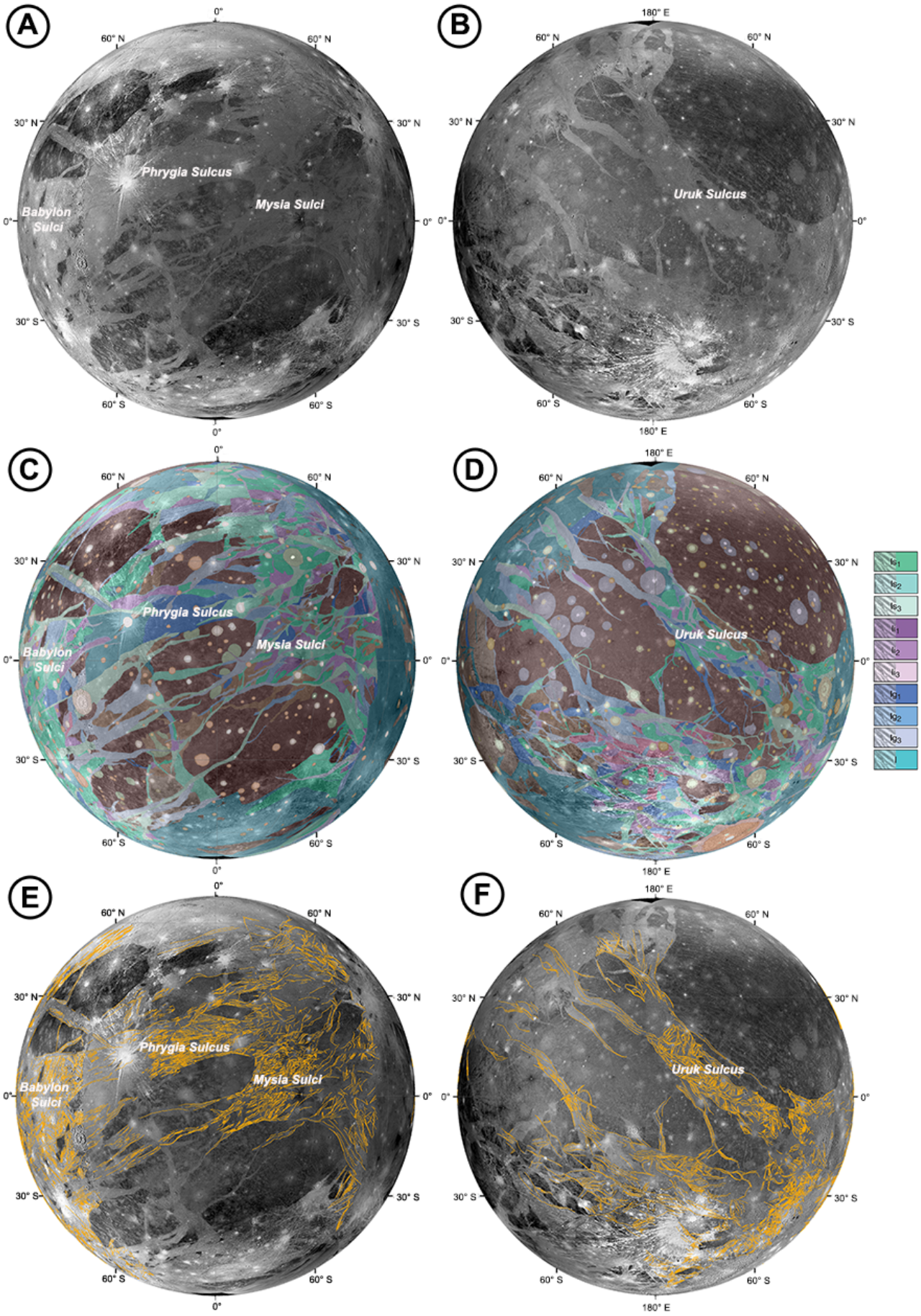
A
B
C
D
E
F
Phrygia Sulcus
Mysia Sulci
Babylon Sulci
Uruk Sulcus
0°
60° N
30° N
30° S
60° S
180° E

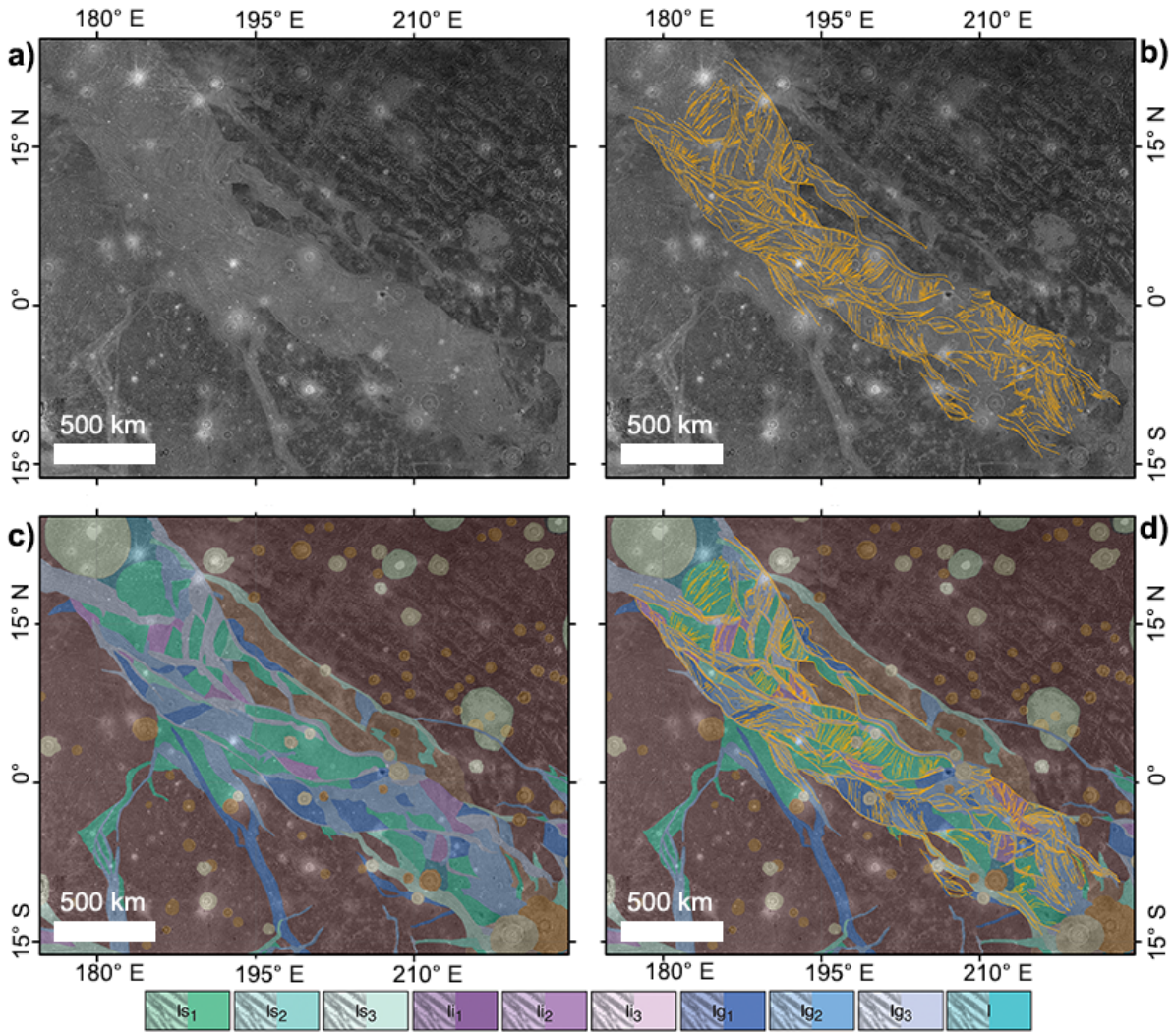

165

166 **Figure 2:** Grooves selected in Uruk Sulcus area in the region centered at 0.8°N, 200°E. A) Ganymede
167 base map (Ganymede Voyager - Galileo SSI Global Mosaic Ganymede, available at
168 https://astrogeology.usgs.gov) representing the area of Uruk Sulcus under study. B) The number of
169 grooves mapped (Rossi et al., 2020) and selected for the analysis is 1068. C) The geological map of
170 Collins et al., (2013) overlaid in transparency on the base map. D) The grooves mapped are overlaid
171 on the geological map. The legend represents the geological units corresponding to the light terrain
172 on which grooves were mapped (light subdued unit: *ls1, ls2, ls3*, light irregular unit: *li1, li2, li3*, light
173 grooved unit: *lg1, lg2, lg3* and light undivided unit *l*). For nomenclature and interpretation of the
174 geological units, we refer the reader to Collins et al., (2013).

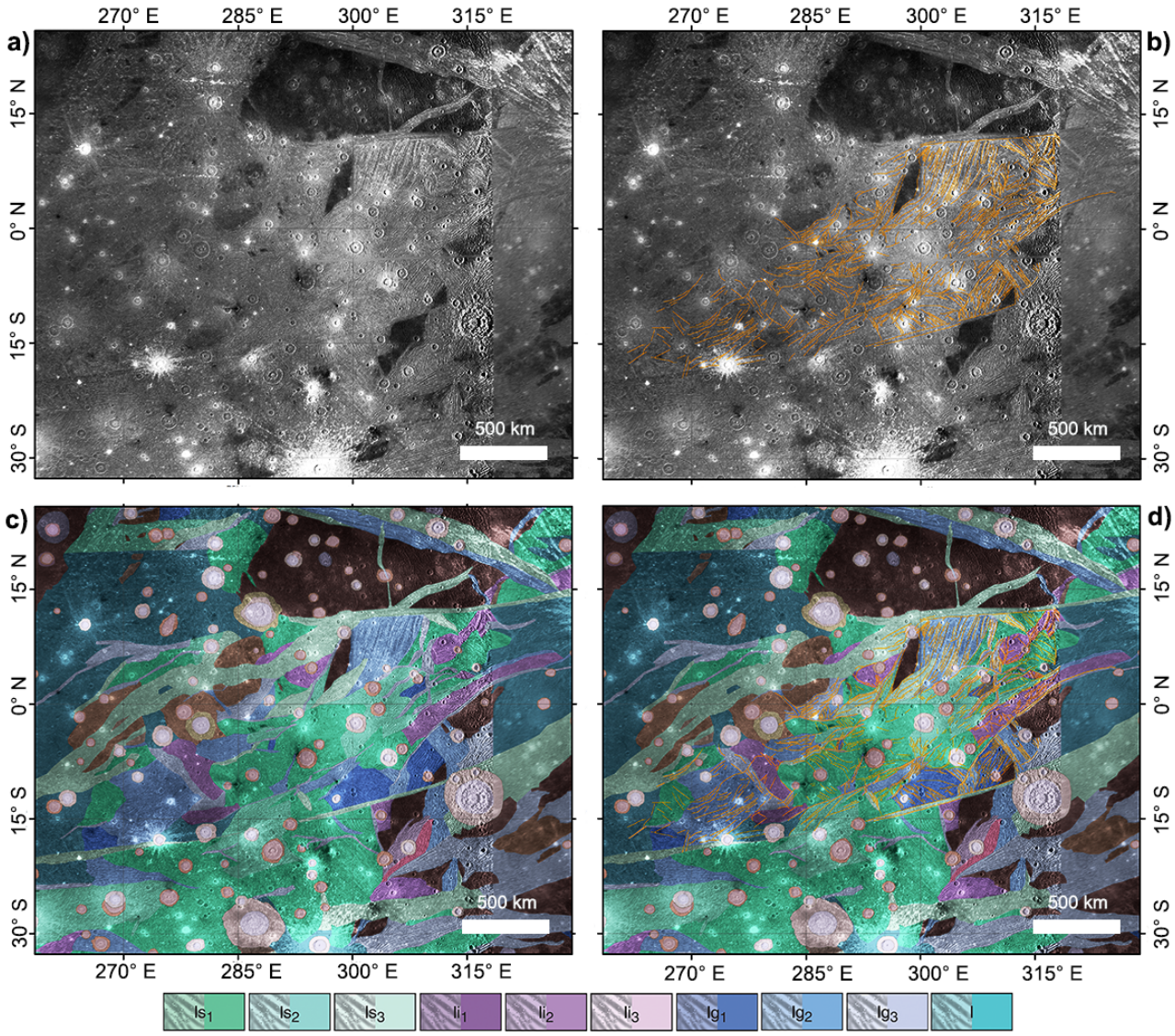

Figure 3: Grooves selected in Babylon Sulci area in the region centered at 0°N, 290°E. A) Ganymede base map (Ganymede Voyager - Galileo SSI Global Mosaic Ganymede, available at https://astrogeology.usgs.gov) representing the area of Babylon Sulci under study. B) The number of grooves mapped (Rossi et al., 2020) and selected for the analysis is 882. C) The geological map of Collins et al., (2013) overlaid in transparency on the base map. D) The grooves mapped are overlaid on the geological map. The legend represents the geological units corresponding to the light terrain on which grooves were mapped (light subdued unit: *ls1, ls2, ls3*, light irregular unit: *li1, li2, li3*, light grooved unit: *lg1, lg2, lg3* and light undivided unit *l*). For nomenclature and interpretation of the geological units, we refer the reader to Collins et al., (2013).

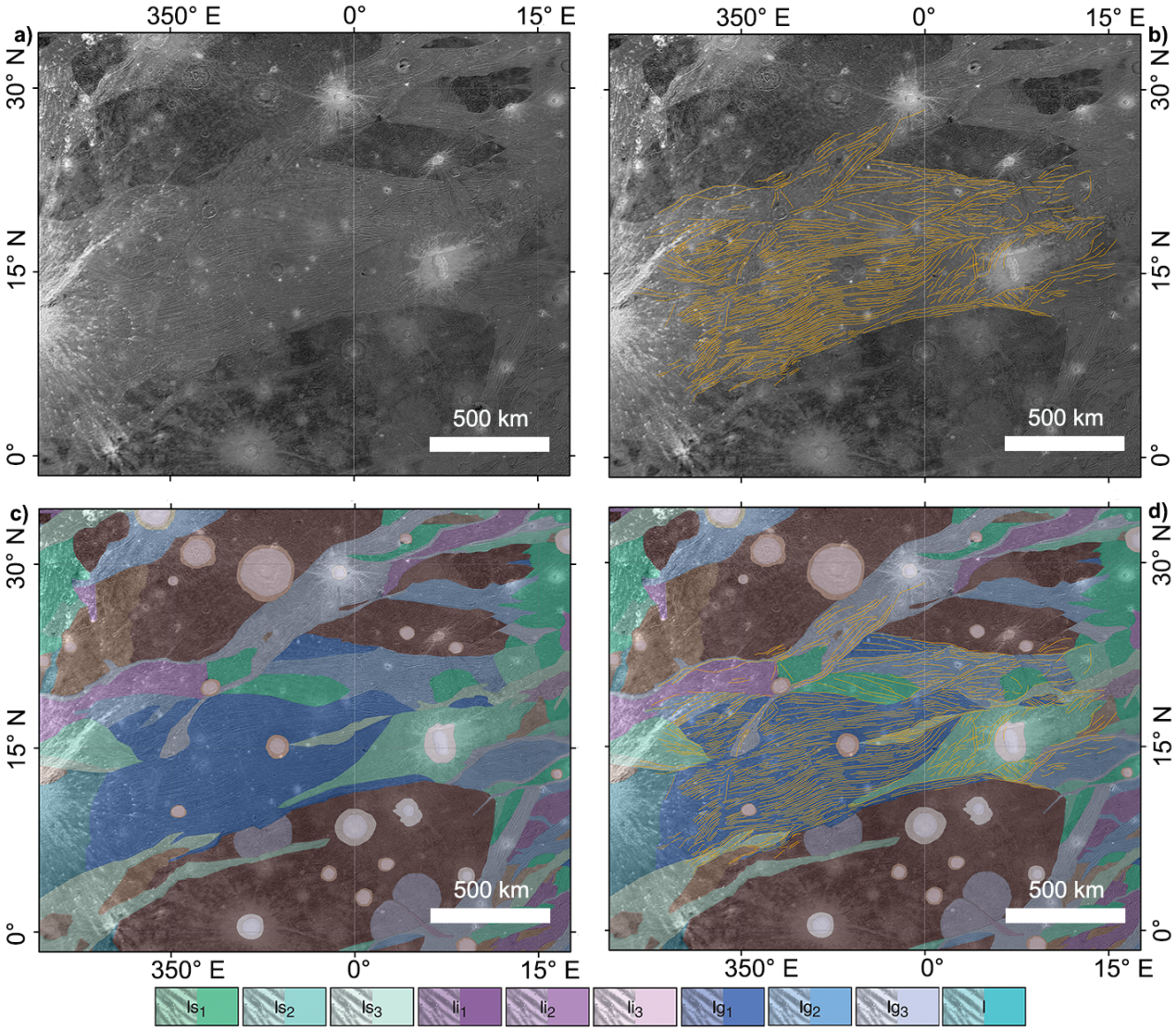

Figure 4: Grooves selected in Phrygia Sulcus area in the region centered at 15°N, 355°E. A) Ganymede base map (Ganymede Voyager - Galileo SSI Global Mosaic Ganymede, available at https://astrogeology.usgs.gov) representing the area of Phrygia Sulcus under study. B) The number of grooves mapped (Rossi et al., 2020) and selected for the analysis is 678. C) The geological map of Collins et al., (2013) overlaid in transparency on the base map. D) The grooves mapped are represented overlaid on the geological map. The legend represents the geological units corresponding to the light terrains on which grooves were mapped (light subdued unit: *ls1*, *ls2*, *ls3*, light irregular unit: *li1*, *li2*, *li3*, light grooved unit: *lg1*, *lg2*, *lg3* and light undivided unit *l*). For nomenclature and interpretation of the geological units, we refer the reader to Collins et al., (2013).

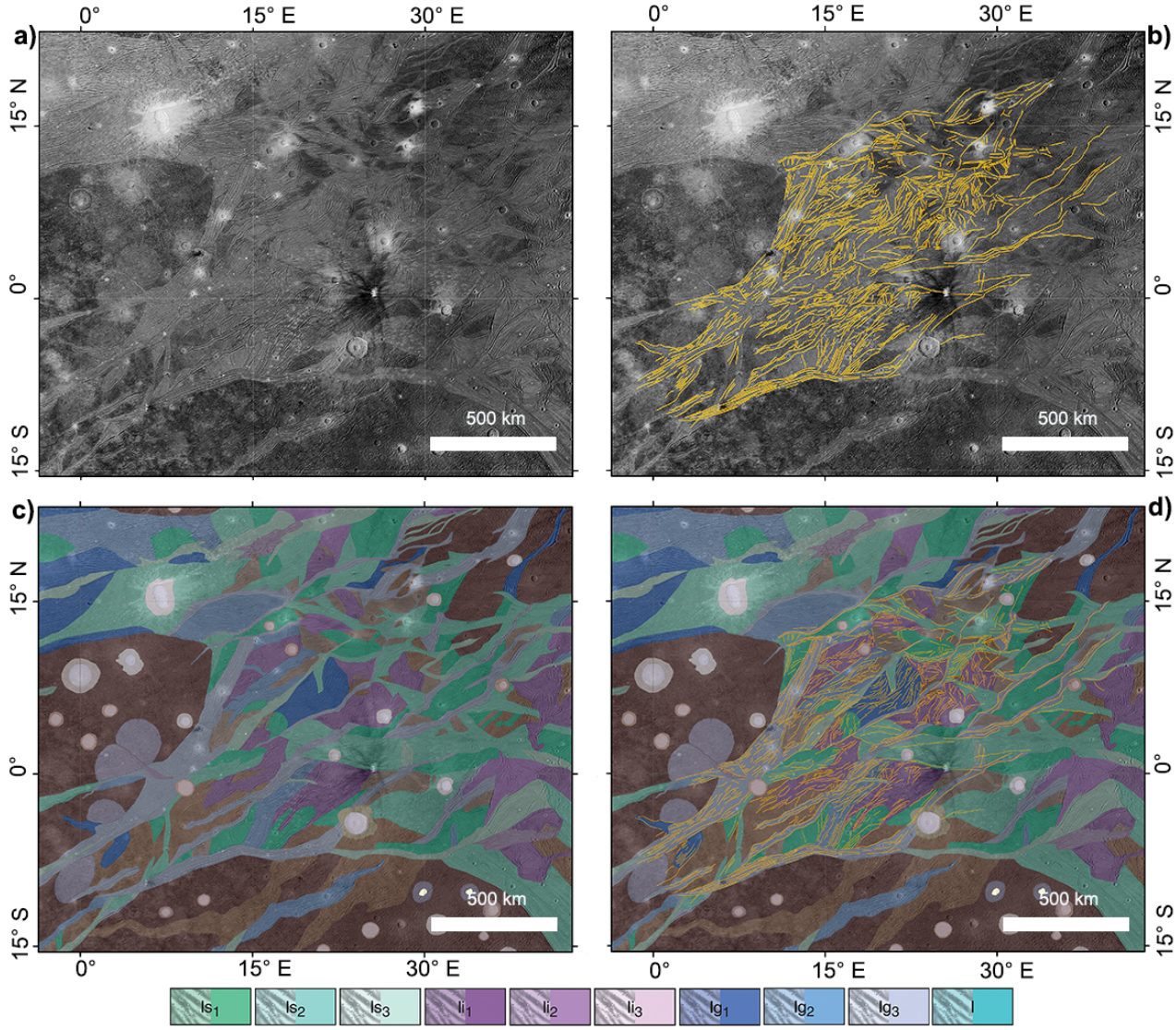

Figure 5: Grooves selected in Mysia Sulci area in the region centered at 7°N, 20°E. A) Ganymede base map (Ganymede Voyager - Galileo SSI Global Mosaic Ganymede, available at https://astrogeology.usgs.gov) representing the area of Mysia Sulci under study. B) The number of grooves mapped (Rossi et al., 2020) and selected for the analysis is 987. C) The geological map of Collins et al., (2013) overlaid in transparency on the base map. D) The grooves mapped are represented overlaid on the geological map. The legend represents the geological units corresponding to the light terrain on which grooves were mapped (light subdued unit: *ls1, ls2, ls3,* light irregular unit: *li1, li2, li3,* light grooved unit: *lg1, lg2, lg3* and light undivided unit *l*). For nomenclature and interpretation of the geological units, we refer the reader to Collins et al., (2013).

206 ## 3. Methods

207 Fault populations statistic can be analysed in terms of its size and spatial distribution (e.g., Soliva and
208 Schultz, 2008; Schultz et al., 2010; Mazzarini et al., 2013; Lucchetti et al., 2017). Size distribution
209 focuses on the properties of geometric features such as fault length, spacing and displacement, while
210 spatial distribution investigates the properties of the whole population such as fault density and
211 **spatial** clustering. We here report the two approaches used in this work to analyse Ganymede's
212 grooves.

213

214 ### 3.1 Length Distribution analysis

215 The propagation and **possible depth**'s confinement of a fault system is usually **explored** by the
216 analysis of **length** distribution (e.g. Soliva and Schultz, 2008; Schultz et al., 2010; Mohajeri and
217 Gudmundsson, 2012; Gudmundsson et al., 2013) that usually follow two different trends: **negative**
218 exponential law distribution and **negative** power law distribution. The first one is represented by the
219 following equation:

220 $N(>l) = \beta e^{-\lambda l}$,

221 where ***N(>l)* is the number of faults whose length is longer than *l*,** β and λ are the parameters of
222 the exponential distribution and l the fault length, while the second one is represented by:

223 $N(>l) = cl^{-\alpha}$,

224 where ***N(>l)* is the number of faults whose length is longer than *l***, c is the scaling factor, α the
225 exponent of the power-law distribution and l is the fault length.

226 The mechanical layering of the crust, as well as a sufficiently large **rheology** contrast in material
227 properties existing between layers, governs the vertical dimension of a fault (height) that is, in turn,
228 nearly proportional to fault length (e.g., Benedicto et al., 2003; Gudmundsson et al., 2010; Soliva and
229 Schultz, 2008). In this scenario, analysis of faults' length distribution usually identifies two end-
230 members (e.g., Soliva and Schultz, 2008; Schultz et al., 2010): (i) fault populations of regularly
231 spaced faults derived from strain partitioning within a single mechanical layer are confined in depth

and are generally characterized by negative exponential distribution (e.g., Cowie et al., 1994; Ackermann et al., 2001); (ii) fault systems, with few large well separated faults cutting across the whole crust displaying a **negative** power-law distribution.

Planetary crusts often record long tectonic evolution, leading to complex structural settings indicating multiple activation of former inherited structures as well as complex internal strain partitioning (Rossi et al., 2018). This means that fractures formed at different stages of the whole deformation history may respond to different fault length size distributions.

3.2 Self-similar Clustering analysis

A robust way to define how fractures (**sensu National Research Council, 1996)** fill space (i.e. fracture spatial distribution) is to analyse their self-similar clustering (Bonnet et al., 2001). Through this methodology it is possible to infer the vertical extension of the connected fractures network starting from the observation of fractures and, then to evaluate the scaling properties of the system (Mazzarini and Isola, 2010). The self-similar clustering of fractures is performed for a range of lengths (the size range) between a lower and an upper cutoff (L_{co} and U_{co}, respectively) by applying the two-point correlation function method to measure the fractal dimension of the fracture population.

For a population of N points (fracture's trace barycenter) the correlation integral *C(l)* is defined as the correlation sum that accounts for all the points at a distance of less than a given length *l* (Hentschel and Procaccia, 1983) by the following equation:

$$C(l)=2N(l)/N(N-1),$$

where *N(l)* is the number of pairs of points whose distance is less than *l*. The self-similar clustering **exists if the following scaling law is satisfied**:

$$C(l)\sim l^{D},$$

where *D* is the fractal exponent defined as the slope of the tangent to the *log(C(l)) vs. log(l)* curve.

A higher value of the *D* exponent implies a more homogeneous distribution of fractures, while a lower value of the *D* exponent means a higher fracture clustering (Figure 6).

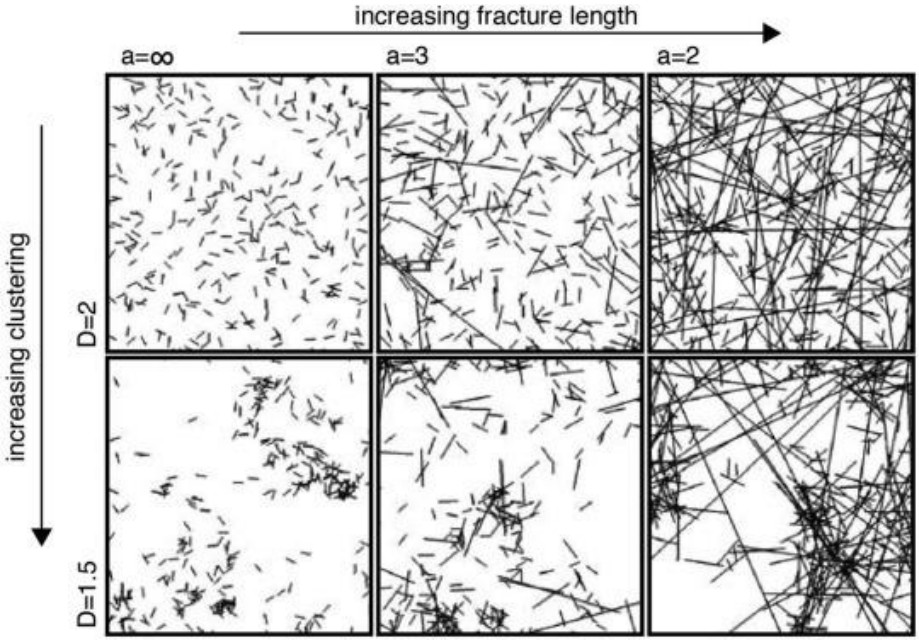

Figure 6: Simulations representing network connectivity controlled by fracture length and clustering. The parameters reported in the figure are the fractal exponent *D*, that controls the degree of self-similar clustering (D = 2 weakly clustered; D = 1.5 strongly clustered) and *a*, that controls the power-law distribution for fracture length (increasing lengths from a = ∞ -short- to a = 2 -long-). Adapted from Darcel et al. (2003) and Mazzarini and Isola, 2010.

The local slope is a point by point measure of the slope of the tangent to the curve):

local slope = $\Delta log(C(l))/\Delta log(l)$.

Self-similarity exists within a size range, bounded by a L_{co} and a U_{co}, and it is detectable as a linear fit (a plateau) in a *local slope* diagram: when the range is wider, the computation of the power-law distribution is better (Walsh and Watterson, 1993).

L_{co} and U_{co} are scale-invariant characteristics of fractures depending on both the resolution of the images used to map and detect fractures (L_{co}) and the mechanical layers and rock/ice properties (U_{co}) (Mandelbrot et al., 1982). Indeed, it has been validated that the thickness of the fractured/deformed layer is mirrored by the occurrence of a threshold value (U_{co}) in the size of the fracture network spatial organization (Pacheco et al., 1992; Davy, 1993; Ouillon et al., 1996;

Mazzarini and D'Orazio, 2003; Mazzarini and Isola, 2010; Gudmundsson et al., 2010; Gudmundsson et al., 2011, Mazzarini et al., 2013).

The derivation of the cut-offs defining the size range is not trivial, especially when the local slope does not show a regular and wide plateau. The choice of L_{co} and U_{co} was estimated by selecting the wider length range for which the correlation between *Log(C(l)) vs Log(l)* is greatest by applying the ordinary least squares fit method (Mazzarini, 2004). By knowing that the fractal behaviour is valid until a significant break in the local slope occurs, we estimate the R^2 value corresponding to the breaking point.

4. Results and Discussion

We analysed the **mapped faults** following the methodology explained in the previous section. Firstly, we obtained the length-frequency histograms **for the faults of each analysed region**, as shown in Fig. 6A-D.

The minimum and maximum length of the 1068 **faults** located in Uruk Sulcus are 0.47 km and 582 km, respectively. The mean is 62.7 km while the median length is 48 km (Figure 7A). The **faults** length size range for Babylon Sulci is between 7.2 and 656 km with a mean and a median length of 77.8 km and 57.9 km, respectively (Figure 7B). Phrygia Sulcus is characterized by a range size of 8.9 - 559 km and a mean and median length of 95.9 and 72.1 km, respectively (Figure 7C). **The** minimum and maximum length of Mysia Sulci are 6.5 and 496 km with an associated mean and median length of 66 km and 47 km (Figure 7D). As outlined in the histograms, there is a small number of **faults** with length < 20 km. This suggests that our datasets may be affected by truncation bias and implies that **relatively short faults** were hardly detectable on a regional scale **with the present day available satellite images.** Indeed, faults analyses are usually characterised by the presence of an upper and a lower bias affecting the measurements. The first is referred to as "censoring", which occurs when the sample size exceeds the dimensions of the measurement area, hence implying the

underestimation of the sample size. **On the other hand**, the second is known as "truncation" and it is related to the image resolution that may lead to small samples undercounting **(Bonnet et al., 2001)**.

After calculating the statistical attributes of **faults**, we obtained the length cumulative plot for each **faults'** network (Figure 7E-H). This analysis reveals that such distribution is characterized by different fitting curves. Indeed, the cumulative plot presents a single or multiple exponential distributions for lengths shorter than L_{th} (length threshold), while there is a power-law distribution for **faults** longer than L_{th}. The presence of both the exponential and power-law trends reflect the possible coexistence of (i) distributed fault systems, with strain regularly partitioned along evenly spaced faults and confined within specific **layers in the crust with different mechanical properties** (exponential fitting curve/curves) and (ii) localized fault systems, with few large faults cutting across the whole crust (power-law fitting curve) (e.g., Soliva and Schultz, 2008; Schultz et al., 2010). In addition, the existence of two exponential distributions for three datasets suggest that there could be two differently confined structure systems within specific mechanical crust layers.

We underline that, even if the number of samples (from 50 up to 200) fitted by a power-law is not as numerous as the ones characterized by the exponential fitting, we are confident about such distribution. Indeed, it is well known that even if the data follow a power-law distribution, it does not mean that the power-law necessarily provides the best model or fit for the data (Clauset et al., 2009; Mohajeri and Gudmundsson, 2012). For this reason, we tested the power-law distribution using the program Matlab and the statistical programing language R following the procedure of Clauset et al., (2009) (see Supplementary Material). This approach validates the existence of the power-law distribution, confirming the presence of a L_{th} separating the exponential and the power-law fitting models. The L_{th} is 93.8 km, 148 km, 238.7 km, 185 km for Uruk Sulcus, Babylon Sulci, Phrygia Sulcus and Mysia Sulci, respectively. The calculated distribution for each dataset is reported in Table 1.

These findings may represent the evolutional history of fault linkages underlying the Ganymede **surface**, where the transition between the exponential and power-law length-frequency

distributions is connected to the fault growth in a vertically confined medium. The **faults** (i.e. grooves) exponential behaviour is representative of both the nucleation of new faults during incipient phases of propagation (when mechanical layering does not have any influence) and the saturation of a vertical confined system of structures (Schultz et al., 2010; Cowie **et al.**, 1994; Ackermann et al., 2001). **On the contrary, the interaction of faults and the consequent linkage/growth process dominates over the nucleation of new faults providing a power-law distribution (Cowie et al., 1995).**

Dataset	N	l range (km)	l_{th} (km)	Distribution (N>l)	
				Exponential ($l<l_{th}$)	Power-law ($l>l_{th}$)
Uruk Sulcus	1068	0.47 - 582	93.8	$\propto e^{-0.47\,l}$ $R^2 = 0.989$ N = 798	$\propto l^{-2.66}$ $R^2 = 0.998$ N = 194
Babylon Sulci	882	7.2 – 646	148	$\propto e^{-0.48\,l}$ $R^2 = 0.991$ (l < 80km) N = 536	$\propto e^{-0.37\,l}$ $R^2 = 0.994$ (l > 80km) N = 201	$\propto l^{-2.96}$ $R^2 = 0.996$ N = 97
Phrygia Sulcus	678	8.9 – 559	238.7	$\propto e^{-0.52\,l}$ $R^2 = 0.992$ (l < 140km) N = 525	$\propto e^{-0.2\,l}$ $R^2 = 0.993$ (l > 140km) N = 73	$\propto l^{-4.35}$ $R^2 = 0.986$ N = 46
Mysia Sulci	987	6.5 – 496	185	$\propto e^{-0.51\,l}$ $R^2 = 0.989$ (l < 90km) N = 688	$\propto e^{-0.22\,l}$ $R^2 = 0.985$ (l > 90km) N = 121	$\propto l^{-3.46}$ $R^2 = 0.992$ N = 56

Table 1: Parameters for each length size distribution of the selected area, where *N* is the **total** number of **faults**, *l range* is defined between the minimum and maximum length value in km and l_{th} the threshold length value discerning between the exponential and power-law distribution of length's **faults**. The last two columns reported the exponential and power-law fitting models found for the selected region, as shown in Figure 7.

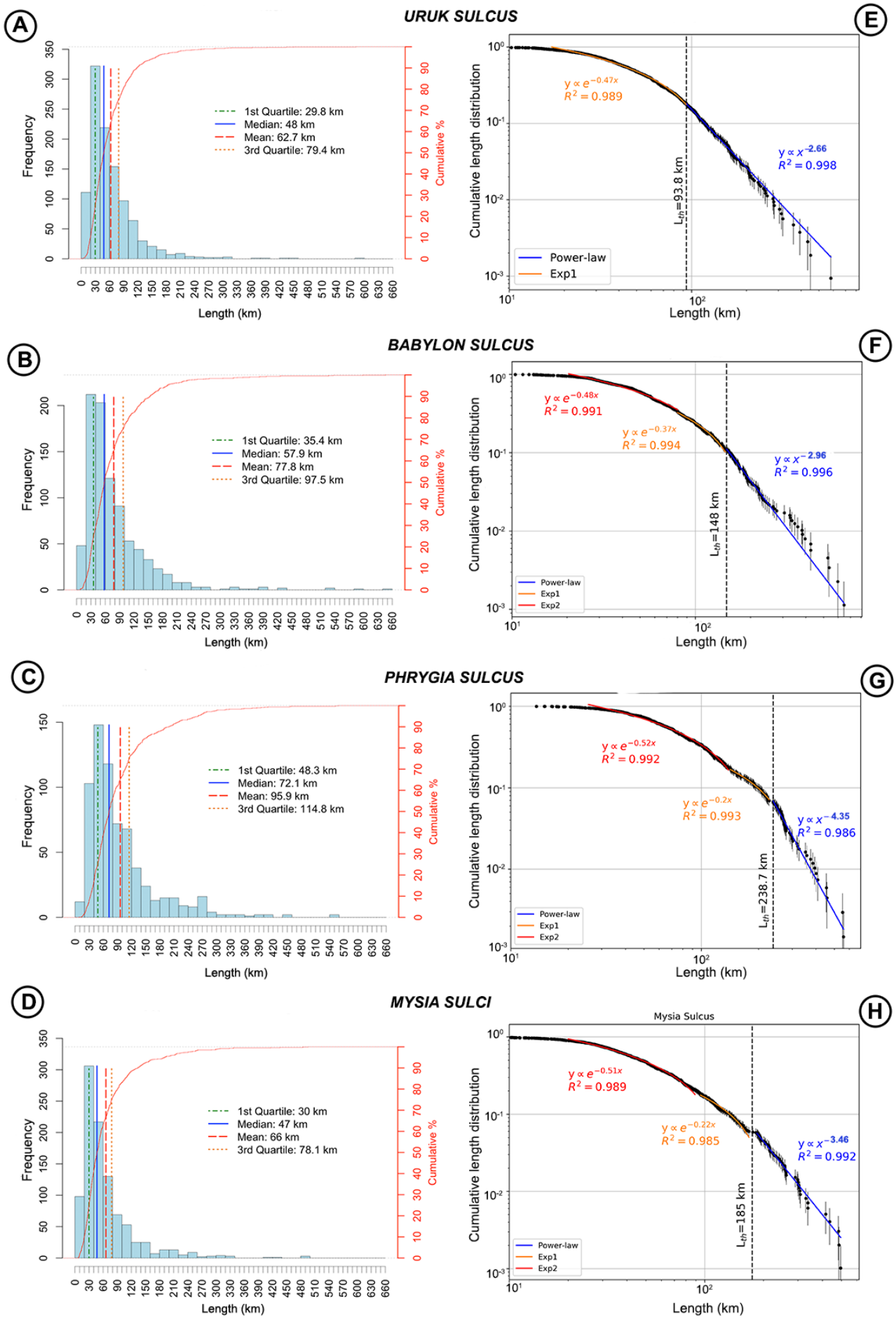
A
URUK SULCUS
E
Frequency
Cumulative %
1st Quartile: 29.8 km
Median: 48 km
Mean: 62.7 km
3rd Quartile: 79.4 km
Length (km)
Cumulative length distribution
$y \propto e^{-0.47x}$
$R^2 = 0.989$
$y \propto x^{-2.66}$
$R^2 = 0.998$
L_{th}=93.8 km
Power-law
Exp1
B
BABYLON SULCUS
F
1st Quartile: 35.4 km
Median: 57.9 km
Mean: 77.8 km
3rd Quartile: 97.5 km
$y \propto e^{-0.48x}$
$R^2 = 0.991$
$y \propto e^{-0.37x}$
$R^2 = 0.994$
$y \propto x^{-2.96}$
$R^2 = 0.996$
L_{th}=148 km
Power-law
Exp1
Exp2
C
PHRYGIA SULCUS
G
1st Quartile: 48.3 km
Median: 72.1 km
Mean: 95.9 km
3rd Quartile: 114.8 km
$y \propto e^{-0.52x}$
$R^2 = 0.992$
$y \propto e^{-0.2x}$
$R^2 = 0.993$
$y \propto x^{-4.35}$
$R^2 = 0.986$
L_{th}=238.7 km
Power-law
Exp1
Exp2
D
MYSIA SULCI
H
Mysia Sulcus
1st Quartile: 30 km
Median: 47 km
Mean: 66 km
3rd Quartile: 78.1 km
$y \propto e^{-0.51x}$
$R^2 = 0.989$
$y \propto e^{-0.22x}$
$R^2 = 0.985$
$y \propto x^{-3.46}$
$R^2 = 0.992$
L_{th}=185 km
Power-law
Exp1
Exp2

Figure 7: Length distribution analysis of A) Uruk Sulcus, B) Babylon Sulci, C) Phrygia Sulcus and D) Mysia Sulci. On the left column the length histograms (bin size =15 km) are reported, while on the right column the length cumulative plots for each dataset are presented. The statistical attributes, such 1st quartile, median, mean and 3rd quartile values, are defined for each histogram plot **and outlined by green, blue, red and orange lines, respectively**. The fitting models of cumulative length distribution are shown on the graphs (E-H) and reported in Table 1. **Faults** shorter than the threshold length L_{th} (black dashed line) are fitted by exponential distributions (red and orange curves), while **faults** longer than L_{th} are fitted by a power-law distribution (blue curve).

The self-similar clustering analysis indicate**s** that the spatial organization of **faults** in each data sets is bounded in a size range with a well-defined upper cutoff. The plateau in the fractal distribution has been inferred from the analysis of the *Log(C(l)) vs Log(l)* diagram (Bonnet et al., 2001, **Figure 8**) and its validity is bounded by a size range (L_{co} and U_{co}) detectable as a linear fit (plateau) in the *local slope vs Log(l)* diagram (Walsh and Watterson, 1993, Figure 8). The choice of L_{co} and U_{co} was estimated by selecting the wider length range for which the **linear** correlation between *Log(C(l))* **and** *Log(l)* (black points in Figure 8) is greatest, by applying the ordinary least squares fit method. Hence, the quality of the correlation was assessed using the coefficient of R^2 determination detecting the size range corresponding to the higher value of R^2. To ensure the reliability of the results, we also cross check the *local slope vs Log(l)* (green points in Figure 8) diagram with R^2 values for all possible size range combination *ΔLog(l)*. Higher R^2 value results in higher reliability of the information. **Hence, we detected the depth range corresponding to the higher values of R^2, thus describing the values of best-fit for the U_{co}, validating the robustness of the U_{co} estimates.** Moreover, the large number of samples used ensures robust estimates of the parameters with an error < 1% (as reported in Mazzarini and Isola 2010). Nevertheless, the L_{co} is very sensitive to the measurement truncation bias, which is in turn correlated with the image resolution. Given that the plateau is rather noisy close to the L_{co}, we do not attribute a reliable significance on it.

This is also supported by the fact that the histograms (Figure 7) show a small number of short **faults** due to the truncation bias mentioned above. On the other hand, the U_{co} (i.e. the highest plateau breaking point) is defined by the maximum value of the size range and it is easily recognizable by a slope break in all considered grooves systems (Figure 8).

The fractal analysis applied on all study areas show a clear plateau in the diagrams (Figure 8), hence providing the identification of the size range where the fractal behaviour is valid. A size interval for both the L_{co} and U_{co} have been outlined through gray bands on Figure 8 and reported in Table 2. Uruk Sulcus reveals a fractal behaviour between 9-11 km and 105-120 km (Figure 8A), Babylon Sulci between 10-13 km and 115-130 km (Figure 8B), Phrygia Sulcus between 10-13 km and 115-130 km (Figure 8C), and Mysia Sulci between 10-13 km and 110-125 km (Figure 8D). As stated above, the values found for L_{co} are not **reliable** due to the noisy data. On the contrary, the values of U_{co} are reliable and comparable for all datasets. The U_{co} is the vertical maximum extension of the connected grooves network (Mazzarini and Isola, 2010, Mazzarini et al., 2013) and, hence, it is directly linked to the mechanical layering of the medium. This analysis reveals that this vertical extension ranges between 105 and 130 km for the four equatorial regions considered. Moreover, this suggests that this limit might be the potential thickness of the icy crust located above the deep ocean **that during a phase of intense deformation and high strain rates may be cut across by very large faults**.

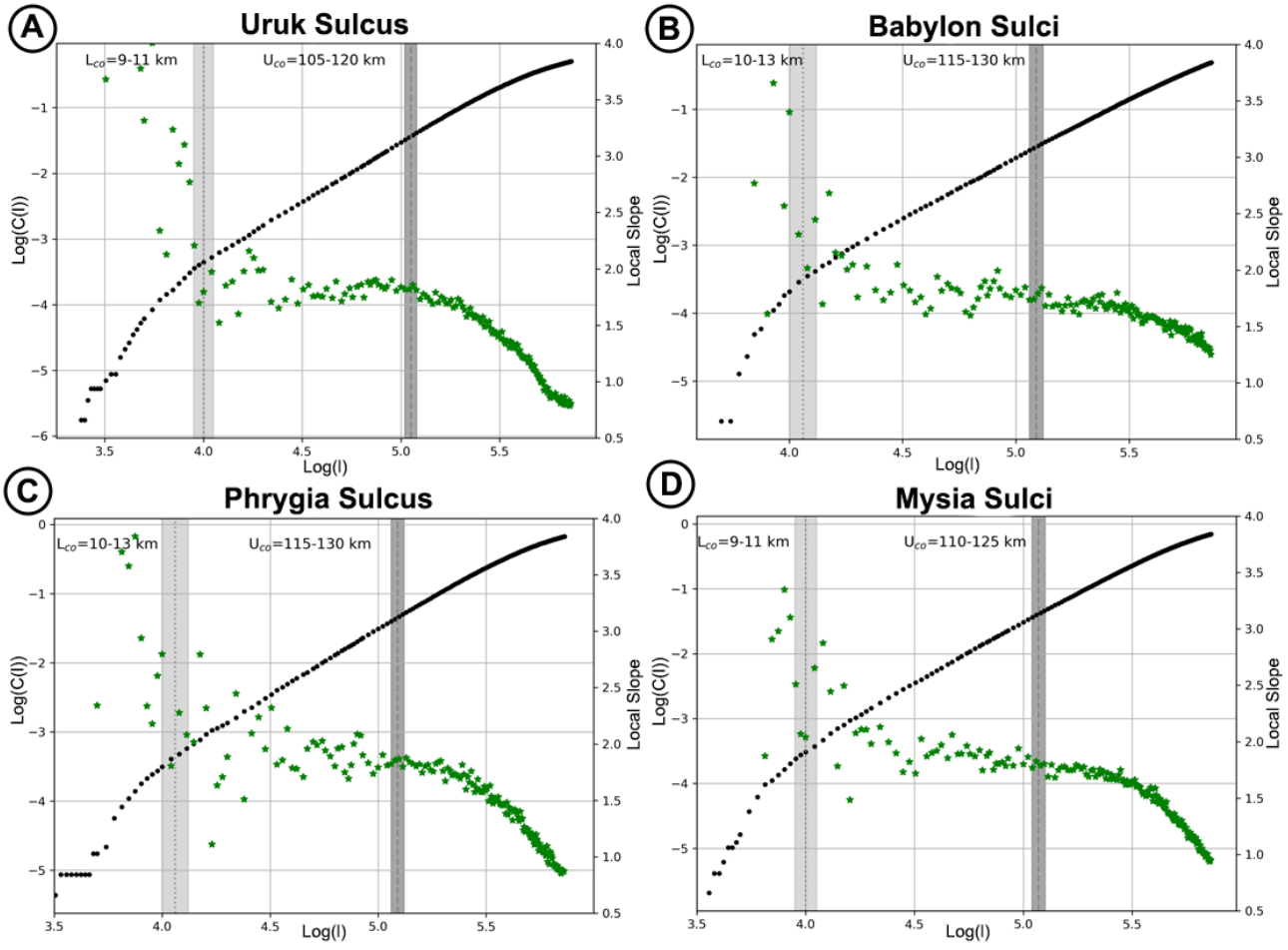

Figure 8: Self-similar clustering analysis for A) Uruk Sulcus, B) Babylon Sulci, C) Phrygia Sulcus and D) Mysia Sulci. For each dataset, it is reported the log plot of *C(l) vs l* (black points) and the *local slope vs Log(l)* plot (green points). The size range of interconnected **faults** are represented by the plateau stage of the local slope curve (green points). The gray stripes are the L_{co} and U_{co} intervals that define the size range of the fractal distribution. The slope of the curve (black points) is the fractal exponent *D* computed in the size range L_{co} - U_{co}. The distribution stops to be fractal when the local slope curve (green points) breaks. The breaking point **may** correspond to a *Log(l)* value (U_{co}) that represents the potential thickness of the icy crust above the deep ocean required for the development of densely populated structures at the surface (i.e. the grooves). U_{co} ranges between 105 km and 130 km, when considering all **fault** system analysed.

Dataset	Longitude	Latitude	N	D	R^2	U_{co}(km)
Uruk Sulcus	185°E - 220°E	15°S - 20°N	1068	1.877± 0.03	0.999	105-120
Babylon Sulci	260°E - 320°E	20°S - 15°N	882	1.847 ± 0.03	0.9991	115-130
Phrygia Sulcus	340°E - 15°E	5°N - 30°N	987	1.945 ± 0.01	0.9997	115-130
Mysia Sulci	10°E - 40°E	10°S - 20°N	678	1.95 ± 0.02	0.9991	110-125

Table 2: Parameters of spatial distribution analysis (self-similar clustering) of **faults** for each selected area with associated latitude and longitude range. *N* is the number of **faults**, *D* the fractal exponent of fractures self-similar clustering, R^2 the goodness of fit and U_{co} the upper cut-off.

We highlight that few **grooves** reaching this maximum depth **(identified as U_{co})** are expected, while a larger number remain confined at much shallower depths, as suggested by the length distribution analysis reported above. Noteworthy, in all four data sets the **faults** fractal distribution is characterized by a well-defined single plateau, suggesting that the strain redistribution at the scale of the whole crust occurs by a hierarchical fracture network where few large faults control and distribute the crustal strain. Indeed, the large **faults** (i.e. grooves) characterised by the power-law fitting behaviour can be considered as crustal-scale structures, typically with a strike slip component (as shown in Cameron et al., 2018; Rossi et al., 2018) that localizes and accommodates most of the crustal strain. Specifically, these large structures can theoretically reach the crust-ocean interface. On the contrary, the shorter **faults** populations (exponentially-fitted) may act as confined structures as response to lower strain.

We underline that time evolution of faults cannot be retrieved by using self-similar clustering, which is representative of the whole deformation that interested the icy crust through time. Indeed, what we observe is that the actual fracture network presents a fractal behaviour, consistent with an actual mechanical stratigraphy. Hypothetically, we may forward that the main initial deformation of the crust occurred via large faults cutting across the whole crust

thickness down to the crust-ocean transition. With time, minor deformation provided the development of exponential distribution of fault cutting across the crust down to the brittle-ductile transition.

The vertical profile of the faults is expected to behave similarly to the Earth faults that become less tilted with the increase of the depth. Indeed, faults gradually transit from sharp geometries to gentle ones when plastic deformation zones are reached at depth. Faults (i.e. grooves) are suggested to be originated by extension and strike-slip regimes that imply different development at depth. On Earth, and hence on the icy crust of Ganymede, extensional deformation creates faults with high dip angle (ideally 60°) that can decrease up to sub-horizontal (i.e. listric faults, e.g. Walsh and Watterson, 1991). On the other hand, strike-slip activity form nearly vertical faults that reach high depths (e.g. Fossen, 2016). In this context, we suggest that the strike-slip faults represent the faults that penetrate deeper and follow the power-law behavior described by our analyses, by potentially reaching the bottom of the icy crust; while the extensional faults are represented by the shorter faults with exponential behavior, that remain at the top layers of the icy crust. It is possible that some of them could assume listric shape at the occurrence of ductile layers and cease to vertically develop at such depth.

In this context, it is also appropriate to clearly state that some extensional faults may show a power-law behavior and penetrate at high depth, and, vice-versa, some strike-slip faults can show exponential behavior by reaching shallow depths.

We expect exponentially-fitted length distribution grooves to be confined within the brittle portion of the crust, in particular when considering crustal rifting modes affecting the opening of the lithosphere in earlier Ganymede history (Pizzi et al., 2019), i.e. when the icy crust was thought to be thinner and most of the **faults'** nucleation took place. Moreover, the vertical extent of the second order structures may be controlled by necking instability **(i.e. modelling Ganymede's lithosphere**

446 **as a brittle surface layer underlain by a viscous half-space)** occurring in Ganymede crust at
447 shallow depth at $\mathbf{10^{-13}}$ s^{-1} strain rate, as suggested by finite element method (FEM) simulations (e.g.,
448 Bland and Showman, 2007). However, the progressive thickening of Ganymede crust through time
449 and the possible effects due to tidal stress (Cameron et al., 2019) may have contributed in localizing
450 the strain within few large pre-existing structures, that may have recurrently reactivated, hence cross-
451 cutting the entire crust.

452 The spatial distribution analysis shows that only a relatively small number of **faults** is able to
453 penetrate the icy crust. Being, most of the longer structures recognized as the boundaries of strike-
454 slip corridors often delimiting the transition between the dark and light terrains, they represent the
455 lead candidates that could have penetrated the entire icy crust. On the other hand, since our data are
456 affected by truncation bias and the analysis has been performed at a regional scale, we cannot infer
457 about the behaviour of shorter **faults** nor observe the surface deformation of shorter structures
458 induced by tidal stresses (Cameron et al., 2019).

459

460 The general framework presented above may suggest two possible tectonic scenarios for
461 **faults** (i.e grooves) development: i) **synchronous** extension and strike-slip activities through time or
462 ii) two distinct evolutionary phases with extension, followed by strike-slip faulting. The occurrence
463 of a single plateau in all datasets could support the first tectonic scenario as the more plausible one.
464 Nevertheless, to fully confirm one scenario over the other, a dedicated structural investigation at
465 higher **spatial** resolution is needed.

466

467 The interpretation of few long **faults** propagating down to the liquid ocean is supported by
468 the values of U_{co} (ranging between 105 and 130 km). Such values agree with independent estimates
469 of Ganymede icy layer thickness. Through the interpretation of Galileo magnetic data, Kivelson et
470 al., (2002) suggested the presence of a conducting layer at a depth of 150 km below the icy crust.
471 Later, Saur et al., (2015) stated the presence of a saline conductive ocean at a depth of 150 km through

472 the observation and modelling of Ganymede's auroral ovals dynamics. On the other hand, Schenk et
473 al., (2002) provides an estimate of at least 80 km for the icy shell thickness by analysing the transition
474 between depth to diameter ratio of large impact craters.
475
476 To summarize, we found that (i) the grooves are the representation of a hierarchical system
477 constituted by second order structures controlled by the rheological layering of the crust (i.e. **faults**
478 fitted by exponential length distribution) and few major crustal-scale structures (i.e. **faults** fitted by
479 power-law distribution) with possible prevalence of strike-slip kinematics, (ii) the occurrence of large
480 first order tectonic structures cutting the whole icy crust that (even if limited in number) may control
481 the crustal strain distribution and (iii) the presence of icy solid crust **above the liquid ocean** with
482 thickness of 100-130 km along the equatorial belt of Ganymede which is in agreement with previous
483 measurements.
484

485 **5. Conclusion**

486 In this work we analysed **the** length size-distribution and self-similar clustering of
487 Ganymede's **groove** populations to estimate the potential thickness of the icy crust above the deep
488 ocean and potential mechanical layering within the crust. Grooves **(i.e. faults)** represent the evidence
489 of tectonic activity that deformed the surface **of Ganymede** during its geologic evolution and
490 characterize the light material unit of the satellite. Specifically, we investigated four regions located
491 on the Ganymede equatorial area by using the regional scale grooves mapping performed by Rossi et
492 al., (2020). The four chosen datasets are selected **from** regions in Uruk Sulcus, Babylon Sulci,
493 Phrygia Sulcus and Mysia Sulci centered at 0.8°N, 200°E, 0°N, 290°E, 15°N, 355°E and 7°N, 20°E
494 and containing 1068, 882, 678 and 987 **faults**, respectively. On such datasets, we firstly performed a
495 length distribution analysis to describe the depth propagation and growing evolution of the faults
496 underlying grooves systems. Then, we investigated the **faults** spatial distribution (self-similar

clustering) in order to infer the vertical extension of the connected fractures network and, hence, evaluate the scaling properties of the system.

We found that the **faults** length distribution change from exponential (shorter **faults**) to power-law (longer **faults**) at a threshold length of 93.8 km, 148 km, 238.7 km, 185 km for Uruk Sulcus, Babylon Sulci, Phrygia Sulcus and Mysia Sulci, respectively.

This means that the shorter, exponentially-fitted populations may act as confined structures, while the large grooves fitted by power-law curves can be considered as crustal-scale structures theoretically reaching the crust-ocean interface. From the self-similar clustering analysis, we estimated the potential thickness of the icy crust **above the liquid ocean** ranging between 105 and 130 km for the datasets considered. This value agrees with independent estimates of the thickness of the icy shell (from 80 to 150 km, Schenk et al., (2002); Kivelson et al., 2002; Saur et al., 2015). Hence, our results support the hypothesis of shorter structures vertically confined in **layers with different mechanical properties** within the icy crust and few very long faults propagating down to the liquid ocean underneath. The latter are likely underlying the longer grooves often associated to strike slip kinematics at the dark/light terrain boundaries, thus representing important targets in the future Ganymede exploration as potential sites of surface-ocean connections.

The structural approach used in our analysis provides new insights into the depth of faults underlying grooves and the mechanical/rheological layering of Ganymede crust. **In particular, we support the that the thickness of the Ganymede's icy crust ranges between 100 km and 130 km, which may be suggested as the depth at which a liquid water ocean is located**.

Once future mission data will be available, this investigation will be largely improved with new measurements and analysis performed at mid and high latitudes. In particular, the upcoming ESA JUICE (Jupiter ICy moons Explorer, Grasset et al., 2013) mission will provide a global coverage of the surface of Ganymede with an average resolution of 100-150 m/px thanks to the JANUS camera (Jovis, Amorum ac Natorum Undique Scrutator, Palumbo et al., 2014). This instrument will provide

the possibility to easily detect grooves and related faults and fractures over the full body. Such images, coupled with digital terrain models will be pivotal to improve the knowledge of the satellite and will provide new insights into the formation and evolution of Ganymede grooves system.

In addition, the methodology presented in this work can be also applied to other icy bodies hosting a liquid ocean being interesting target for astrobiology, such as Europa (Kereszturi and Keszthelyi, 2013; Silber and Johnson, 2017; Domagal-Goldman et al., 2016).

Data availability

Data used in this work are those published by Rossi et al., (2020).

Acknowledgments

The activity has been realized under the ASI-INAF contract 2018-25-HH.0. This manuscript is part of a project that has received funding from the European Union's Horizon 2020 research and innovation programme under grant agreement Nº776276 (PLANMAP). We made use of the ArcGIS 10.5, Matlab and R softwares to perform the presented analysis.

References

Ackermann, R.V., et al., 2001. The geometric and statistical evolution of normal fault systems: An experimental study of the effects of mechanical layer thickness on scaling laws: Journal of Structural Geology, v. 23, p. 1803–1819, doi: 10.1016/S0191-8141(01)00028-1.

Anderson, J. Det al., 2001. Shape, mean radius, gravity field and interior structure of Ganymede. In *Bulletin of the American Astronomical Society* (Vol. 33, p. 1101).

Allison, M.L, Clifford, S. M., 1987. Ice-covered water volcanism on Ganymede. J. Geophys. Res., 92(B8), 7865-7876.

Becker, T. et al., 2001. Final digital global maps of Ganymede, Europa, and Callisto. Lunar Planet. Sci. Conf. XXXII, 2009.

549 Belton, M. J. S., et al., 1992. The Galileo solid-state imaging experiment. *Space Science*
550 *Reviews*, *60*(1-4), 413-455.
551 Belton, M. J. S., et al., 1996. Galileo's first images of Jupiter and the Galilean satellites. Science,
552 274(5286), 377.
553 Benedicto, A., et al., 2003. Layer thickness and shape of faults. Geophysical Research Letters, 30,
554 20, 2076, doi:10.1029/2003GL018237.
555 Bianchi, R., et al., 1984. Tectonics of the grooved terrain on Ganymede. Lunar and Planetary Science
556 Conference, 15, 54–55.
557 **Bianchi, R., Casacchia, R., Lanciano, P., Pozio, S., & Strom, R. G., 1986. Tectonic framework**
558 **of grooved terrain on Ganymede. Icarus, *67*(2), 237-250.**
559 Bland, M. T., Showman, A. P., 2007. The formation of Ganymede's grooved terrain: Numerical
560 modeling of extensional necking instabilities. Icarus, 189(2), 439-456.
561 Bonnet, E., et al., (2001), Scaling of fracture systems in geological media: Reviews of Geophysics,
562 v. 39, p. 347–383, doi: 10.1029/ 1999RG000074.
563 Bour, O., Davy, P., 1999. Clustering and size distribution of fault patterns: Theory and measurements:
564 Geophysical Research Letters, v. 26, p. 2001–2004, doi:10.1029/1999GL900419.
565 Bour, O., et al., 2002. A statistical scaling model for fracture network geometry, with validation on a
566 multiscale mapping of a joint network (Hornelen Basin, Norway): Journal of Geophysical
567 Research, v. 107, p. 2113, doi: 10.1029/2001JB000176.
568 Cameron, M.E., et al., 2018. Morphological mapping of Ganymede: Investigating the role of strike-
569 slip tectonics in the evolution of terrain types. Icarus 315, 92–114.
570 Cameron, M. E., et al., 2019. Tidal stress modeling of Ganymede: Strike-slip tectonism and Coulomb
571 failure. *Icarus*, *319*, 99-120.
572 Carr, M. H., et al., 1995. The Galileo Imaging Team plan for observing the satellites of Jupiter. J.
573 Geophys. Res. Planets, 100(E9), 18935-18955.

574 Casacchia, R., Strom, R. G., 1984. Geologic evolution of Galileo Regio, Ganymede. Lunar Planet.
575 Sci. Conf. XIV, 1028.
576 Clauset, A., et al., 2009. Power-law distributions in empirical data. *SIAM review*, *51*(4), 661-703.
577 Collins, G. C., et al., 2000. A global database of grooves and dark terrain on Ganymede, enabling
578 quantitative assessment of terrain features. Lunar Planet. Sci. Conf. XXXI, 1034.
579 Collins, G. C., 2009. The origin of grooved terrain on Ganymede. European Planetary Science
580 Congress, 4, 516.
581 Collins, G. C., et al., 2013. Global geologic map of Ganymede. US Department of the Interior, US
582 Geological Survey. doi:10.3133/sim3237.
583 Cowie, P. A., et al., 1994. Quantitative fault studies on the East Pacific Rise: A comparison of sonar
584 imaging techniques. *Journal of Geophysical Research: Solid Earth*, *99*(B8), 15205-15218.
585 Croft, S. K., Strom, R. G., 1985. Ganymede's crust: Structural indicators in the Tiamat Sulcus
586 quadrangle. Lunar Planet. Sci. Conf. XVI, 156-157.
587 Davy, P., 1993, On the frequency-length distribution of the San Andreas fault system: Journal of
588 Geophysical Research, v. 98, p. 12,141–12,151, doi:10.1029/93JB00372.
589 **Domagal-Goldman, S. D., et al., 2016. The astrobiology primer v2. 0. Astrobiology, *16*(8), 561.**
590 Dombard, A. J., McKinnon, W. B., 2001. Formation of grooved terrain on Ganymede: Extensional
591 instability mediated by cold, superplastic creep. Icarus, 154(2), 321-336.
592 Figueredo, P. H., et al., 1999. Fracture patterns on Ganymede and the initiation of tectonic
593 resurfacing. Lunar Planet. Sci. Conf. XXX, 1832.
594 Grasset, O., et al., 2013. JUpiter ICy moons Explorer (JUICE): An ESA mission to orbit Ganymede
595 and to characterise the Jupiter system. *Planetary and Space Science*, *78*, 1-21.
596 Gudmundsson, A., et al., 2010. Effects of internal structure and local stresses on fractyre propagation,
597 deflection and arrest in fault zones. Journal of Structural Geology, 32, 1643-1655.
598 Gudmundsson, A., 2011 Rock Fractures in Geological Processes. Cambridge University Press,
599 Cambridge, UK, pp 594.

600 Gudmundsson, A., Mohajeri, N., 2013. Relations between the scaling exponents, entropies, and
601 energies of fracture networks. Bull. Géol. France, 2013, 184, 4, 377-387.
602 Gudmundsson, A., et al., 2013. Length-displacement scaling and fault growth. Tectonophysics, 608,
603 1298-1309.
604 **Hargitai, H., & Kereszturi, Á. (Eds.), 2015. Encyclopedia of planetary landforms. Springer New**
605 **York.**
606 Head, J. W., et al., 2002. Evidence for Europa-like resurfacing styles on Ganymede. Geophys. Res.
607 Lett. 29, 2151.
608 Hentschel, H. G. E., I. Proccacia, 1983. The infinite number of generalised dimensions of fractals and
609 strange attractors, Physica D: Nonlinear Phenomena, 435-444.
610 **Hirata, N., Suetsugu, R., & Ohtsuki, K., 2020. A global system of furrows on Ganymede**
611 **indicative of their creation in a single impact event. *Icarus*, 113941.**
612 Hussmann, H., et al., 2007. Interiors and evolution of icy satellites. In T. Spohn & G. Schubert (Eds.),
613 Treatise on Geophysics. 10 (pp. 509–539).
614 **Kereszturi, A., & Keszthelyi, Z., 2013. Astrobiological implications of chaos terrains on Europa**
615 **to help targeting future missions. *Planetary and Space Science, 77*, 74-90.**
616 Kivelson, M.G., et al., 1997. The magnetic field and magnetosphere of Ganymede, Geophys. Res.
617 Lett., 24, 2155-2158.
618 Kivelson, M. G., et al., 2002. The permanent and inductive magnetic moments of Ganymede. Icarus,
619 157(2), 507-522.
620 Kuskov, O. L., et al., 2010. Internal Structure of the Icy Satellites of Jupiter. In *Advances in*
621 *Geosciences: Volume 19: Planetary Science (PS)* (pp. 365-376).
622 Lucchitta, B. K., 1980. Grooved terrain on Ganymede. Icarus, 44(2), 481-501.
623 Lucchetti, A., et al., 2017. Brittle ice shell thickness of Enceladus from fracture distribution
624 analysis. *Icarus*, *297*, 252-264.
625 Mandelbrot, B.B., 1982, The Fractal Geometry of Nature: San Francisco, Freeman, 468 p.

626 Mazzarini F., D'Orazio, M., 2003. Spatial distribution of cones and satellite-detected lineaments in
627 the Pali Aike Volcanic Field (southernmost Patagonia): Insights into the tectonic setting of a
628 Neogene rift system: Journal of Volcanology and Geothermal Research, v. 125, p. 291–305, doi:
629 10.1016/S0377-0273(03)00120-3.
630 Mazzarini, F., 2004, Volcanic vent self-similar clustering and crustal thickness in the northern Main
631 Ethiopian Rift: Geophysical Research Letters, v. 31, p. L04604, doi: 10.1029/2003GL018574.
632 Mazzarini, F., Isola, I. 2010. Monogenetic vent self-similar clustering in extending continental crust:
633 Examples from the East African Rift System: Geosphere, v. 6, p. 567–582, doi: 10
634 .1130/GES00569 .1.
635 Mazzarini, F., et al., 2013 Spatial relationship between earthquakes and volcanic vents in the central-
636 northern Main Ethiopian Rift. *Journal of Volcanology and Geothermal Research* 262, 123–133.
637 McKinnon, W. B., Melosh, H. J., 1980. Evolution of planetary lithospheres: Evidence from
638 multiringed structures on Ganymede and Callisto. Icarus, 44(2), 454-471.
639 Mohajeri, N., and Gudmundsson, A., (2012). Entropies and Scaling Exponents of Street and Fracture
640 Networks. Entropy, 14, 800-833.
641 Moore, J. M., et al., 1999. Mass movement and landform degradation on the icy Galilean satellites:
642 Results of the Galileo nominal mission. Icarus, 140(2), 294-312.
643 Murchie, S. L., et al., 1986. Terrain types and local scale stratigraphy of grooved terrain on
644 Ganymede. Lunar Planet. Sci. Conf. Proceedings, 17.
645 Murchie, S. L., et al., 1989. Crater densities and crater ages of different terrain types on Ganymede.
646 Icarus, 81, 271-297.
647 Murchie, S. L., et al., 1990. Tectonic and volcanic evolution of dark terrain and its implications for
648 the internal structure and evolution of Ganymede. Journal of Geophysical Research: Solid Earth,
649 95(B7), 10743–10768. doi:10.1029/JB095iB07p10743.

National Research Council, 1996. Rock Fractures and Fluid Flow: Contemporary Understanding and Applications. The National Academies Press, Washington, DC. https://doi.org/10.17226/2309.

Neukum, G., 1997. Bombardment history of the Jovian system. The Three Galileos: The Man, the Spacecraft, the Telescope. Springer, Dordrecht, pp. 201–212.

Neukum, G., et al., 1998. Cratering chronology in the Jovian system and derivation of absolute ages. Lunar Planet. Sci. Conf. XX IX, 1742.

Ouillon, G., et al., 1996. Hierarchical geometry of faulting: Journal of Geophysical Research, v. 101, p. 5477–5487, doi:10.1029/95JB02242.

Pacheco, J.F., et al., 1992. Change in the frequency-size relationship from small to large earthquakes: Nature, v. 355, p. 71–73, doi:10.1038/355071a0.

Palumbo, P., et al., 2014. JANUS: the visible camera onboard the ESA JUICE mission to the Jovian system. In *EGU General Assembly Conference Abstracts* (Vol. 16).

Pappalardo, R. T., Greeley, R., 1995. A review of the origins of subparallel ridges and troughs: Generalized morphological predictions from terrestrial models. J. Geophys. Res.: Planets, 100(E9), 18985-19007.

Pappalardo, R. T., et al., 1998. Grooved terrain on Ganymede: First results from Galileo high-resolution imaging, Icarus, 135, 276-302.

Pappalardo, R. T., et al., 2004. Geology of Ganymede. Jupiter: Planet, Satellites, and Magnetosphere, 363-396.

Patterson, G. W., et al., 2010. Global geological mapping of Ganymede. Icarus, 207(2), 845- 867.

Pozzobon, R., et al., 2015. Self-similar clustering distribution of structural features on Ascraeus Mons (Mars): implications for magma chamber depth. *Geological Society, London, Special Publications*, *401*(1), 203-218.

Prockter, L. M., et al., 1998. Dark terrain on Ganymede: Geological mapping and interpretation of Galileo Regio at high resolution. Icarus, 135(1), 317-344.

676 Prockter, L. M., et al., 2000. Geology and mapping of dark terrain on Ganymede and implications for
677 grooved terrain formation. J. Geophys. Res.: Planets, 105(E9), 22519-22540.
678 Rossi, C., et al., (2018). Evidence of transpressional tectonics on the Uruk Sulcus region,
679 Ganymede. *Tectonophysics*, *749*, 72-87.
680 Rossi, C., et al., (2020). Structural geology of Ganymede regional groove systems (60° N–60°
681 S). *Journal of Maps*, 1-11.
682 Russell, C. T. (Ed.), 2012. *The Galileo Mission*. Springer Science & Business Media.
683 Saur, J., et al., 2015. The search for a subsurface ocean in Ganymede with Hubble Space Telescope
684 observations of its auroral ovals. Journal of Geophysical Research: Space Physics, 120(3), 1715-
685 1737.
686 Schenk, P., McKinnon, W. B., 1987. Ring geometry on Ganymede and Callisto. Icarus, 72(1), 209–
687 234. doi:10. 1016/0019-1035(87)90126-6-
688 Schenk, P. et al., 2001. Flooding of Ganymede's bright terrains by low-viscosity water-ice lavas.
689 Nature, 410(6824), 57-60.
690 Schenk, P. M., 2002. Thickness constraints on the icy shells of the Galilean satellites from a
691 comparison of crater shapes. Nature 417, 419-421.
692 Schenk, P. M., et al., 2004. Ages and interiors: The cratering record of the Galilean satellites. Jupiter:
693 The planet, satellites and magnetosphere, 427-456.
694 Schultz, R.A., et al., 2010. Fault populationsons. In: *Planetary Tectonics*, edited by Thomas R.
695 Watters and Richard A. Schultz. Cambridge University Press, Cambridge, 457-510.
696 Shoemaker, E. M., et al., 1982. The geology of Ganymede. In Satellites of Jupiter, 1, 435-520.
697 Showman, A.P., et al., 2004. On the resurfacing of Ganymede by liquid water volcanism. Icarus 172,
698 625–640. doi: 10.1016/j.icarus.2004.07.011.
699 **Silber, E. A., & Johnson, B. C., 2017. Impact crater morphology and the structure of Europa's**
700 **ice shell. Journal of Geophysical Research: Planets, *122*(12), 2685-2701.**
701 Smith, B.A., et al., 1979a, The Jupiter system through the eyes of Voyager 1, Science, 204.

Smith, B. A., et al., 1979b. The Galilean satellites and Jupiter: Voyager 2 imaging science results. Science, 206(4421), 927-950.

Sohl, F., et al., 2002. Implications from Galileo observations on the interior structure and chemistry of the Galilean satellites. *Icarus*, *157*(1), 104-119.

Soliva, R., Schultz, R.A., 2008. Distributed and localized faulting in extensional settings: Insight from the North Ethiopian Rift–Afar transition area. Tectonics, 27, TC2003, doi:10.1029/2007TC002148.

Walsh, J.J., Watterson, J., 1993. Fractal analysis of fracture pattern using the standard box-counting technique: Valid and invalid methodologies: Journal of Structural Geology, v. 15, p. 1509–1512, doi: 10.1016/0191- 8141(93)90010-8.

Zahnle, K., et al., 2003. Cratering rates in the outer Solar System. Icarus, 163(2). 263–289. doi:10.1016/S0019-1035(03)00048-4.

Reviewer #1: General comments

The work is presenting new results on the analysis of grooves on the surface of Ganymede in order to estimate the subsurface rheological characteristics of the satellite. It presents new and interesting results, worth for publishing, especially it is closely connected to the JUICE mission main target. The structure of the manuscript is good, the language is OK, the illustration is also good. However before the acceptance several small aspects should be improved, thus the referee suggests moderate revision.

We thank the referee for the positive and constructive revision. We answered below to the major points raised by the referee and we modified the manuscript accordingly to the suggestions.

The main general comments are:

· The authors argue that the statistical analysis of the grooves might provide information on the depth of the subsurface ocean, what is true, however they do not give such an estimation. Probably the results are not enough to make such an estimation however some argumentation on it, at least as a minimal or scale of depth would be useful, including its comparison to other estimations in the discussion section.

With the fractal method we can infer the thickness at which grooves penetrated in the icy layer and, hence, provide the thickness variability of the crust of Ganymede. What the reviewer suggests makes sense considering that the derived crust thickness most likely coincides with the depth of the interface with the liquid ocean. This is also supported by previous measurements: (i) Kivelson et al., (2002) suggested the presence of a conducting layer at a depth of 150 km below the icy crust from interpretation of Galileo magnetic data. Moreover, Saur et al., (2015) stated the presence of a saline conductive ocean at a depth of 150 km. On the other hand, Schenk et al., (2002) provides an estimate of at least 80 km for the icy shell thickness by analysing the transition between depth to diameter ratio of large impact craters. This means that from our results, we expect a global ocean located at 105-130 km depth depending on the area of the satellite considered. We expanded the text in order to describe in greater details our findings.

· It would be more favourable if they implement just sentences on the expected real behaviour or route of the subsurface of the faults. From the Earth we know that very deep penetrating faults became less tilted relatively to the vertical along with the increasing depth (like listric faults), or they might transit gradually from a sharp fault to a plastic deformation zone, or they might even split to more faults etc. Some short discussion on these aspects would be appreciated in the revised version. For example at 413 line and at other locations.

The vertical profile of the grooves is expected to behave similarly to the Earth faults that become less tilted with the increase of the depth. Indeed, faults gradually transit from sharp geometries to gentle ones when plastic deformation zones are reached at depth. Grooves are suggested to be originated by extension and strike-slip regimes that imply different development at depth. On Earth and, hence, on the icy crust of Ganymede, extensional deformation originates faults with high dip (ideally 60°) that can decrease up to sub-horizontal geometries (listric faults, e.g. Walsh and Watterson, 1991). On the other hand, strike-slip activity form nearly vertical faults that reach high depths (e.g. Fossen, 2016). In this context, we suggest that the strike-slip grooves represent the faults that penetrate deeper and follow the power-law behavior described by our analyses, by potentially reaching the bottom of the icy crust; while the extensional grooves are represented by the shorter faults with exponential behavior, which remain at the top layers of the icy crust. It is possible that some of them could assume listric shape at the occurrence of ductile layers and cease to vertically develop at depth. It is appropriate to clearly state that some extensional grooves

may show a power-law behavior and penetrate at high depth, and, vice-versa, some strike-slip faults can show exponential behavior by reaching shallow depths.
We added these sentences in the manuscript, as suggested.

· The temporal aspect was not mentioned in the work, something about the relative or absolute age of these groove systems and their relation to the geological history of Ganymede would be useful, as if a hypothetic ocean depth would be estimated, it should be representative for the given period.
Time evolution cannot be retrieved by using self-similar clustering, indeed the actual fracture network shows a fractal behaviour consistent with an actual mechanical stratigraphy (derived by analyzing the cut-offs of the Dlog(C(l))-Dlog(l) spectrum). Hypothetically, we may forward that the main initial deformation of the crust occurred via large faults cutting across the whole crust thickness down to the crust-ocean transition. With time, minor deformation provided the development of exponential distribution of fault cutting across the crust down to the brittle-ductile transition. This can be envisaged for data sets presenting two exponential populations of grooves. In Uruk Sulcus area, we have no means for separating the large power-law fault system from the one with exponential behaviour, being likely that major faults cut across all the crust and minor faults only the brittle layer. In this way, we can assume that the longer grooves, candidates to the penetration of the icy crust, are relatively older than the minor ones. These latter may be originated at a later stage due to the activity of the main ones.
We added these sentences in the manuscript, as suggested by the referee.

· Some further references are needed for better context:
o around 40-41 lines please cite:<https://ui.adsabs.harvard.edu/abs/2015epl..book.....H/abstract>
o also put some sentences to the Introduction section on Europa (for example after the first paragraph), mentioning that magnetic field based ocean observation also happened there:<https://ui.adsabs.harvard.edu/abs/2019NatAs...3..401G/abstract> , the surface tectonic (<https://ui.adsabs.harvard.edu/abs/2013P%26SS...77...74K/abstract>) and crater structures' parameters also indicate the depth of the ocean on Europe (<https://ui.adsabs.harvard.edu/abs/2002Natur.417..419S/abstract> ,<https://ui.adsabs.harvard.edu/abs/2017JGRE..122.2685S/abstract>)
o also mentioned in the introduction that astrobiology relevance also has the supposed ocean:<https://ui.adsabs.harvard.edu/abs/2016AsBio..16..561D/abstract>
We added a sentence in the conclusion in order to consider Europa as a future target on which we can apply our methodology due to its liquid ocean. Hence, we report also the references suggested by the referee in the conclusion section and in the reference list.

Specific comments

109-11 lines
please clearly define what is the length of a lineament in the case of several interconnecting or crossing, splitting lineaments
The lineament length is the length of a detected linear feature. If the lineament abuts or is cut by other lineaments, the length of each segment is measured. The large number of lineaments reduces the effect on the analyzed data populations of a possible lineament segmentation.

112 line
"different relative age have been identified"
would it be better to write about „relative age domains or groups"

We modified the sentence as suggested.

115-116 lines
"The local scale provides spacing between the structures < 5 km and length < 50 km"
please rewrite or explain more clearly this sentence
We rewrite the sentence as follows: "The local scale allows the identification of structures spacing < 5 km and length < 50 km.."

128-129 lines
"thanks to the luminosity contrast resulting from the solar lighting conditions"
do you mean shadow effect?
Yes, the Ganymede map is composed of images with different illuminations condition, hence only where there is enough luminosity contrast it is possible to identify and map these structures.

133 line
„The four datasets are in selected regions"
consider to modify to „The four datasets are located in selected regions"
We have modified the sentence accordingly.

152 line
"identified grooves structures"
consider to modify to „identified groove structures"
Done.

255 line
„does not show a regular and wide plateau"
please indicate where are these visible in the diagrams, as might not be evident for all readers
We report and explain later in the paper the identification of the plateau in the datasets analysed.

250 line
„the better the computation of the power-law"
consider to modify to „the better the computation is of the power-law"
We modified the sentence as follows: "when the range is wider, the computation of the power-law distribution is better"

265 line
„The minimum and maximum"
please explain somewhere (maybe in the Methods section) how the minimum was measured, as for smaller lineaments are difficult to identify
The minimum is the value of the shortest lineament length identified in the mapping. This value is higher than the resolution of the image, hence, the value is reliable.

266-269 line
please consider to put these numbers to a table
The numbers have been reported in Table 1 under the *l range (km)* column.

285 line
„confined within specific mechanical layers in the crust"
please provide a bit more detailed characterization of this „specific mechanical layer"

We rephrase the sentence as follows: "layers in the crust with different mechanical properties".

288-289 line
"existence of two exponential distributions for three datasets suggest that there could be two differently confined structure systems within specific mechanical crust layers."
please consider to indicate this in the abstract too
We added the statement in the abstract.

306 line
"Cowie et al., 1994;"
do not use italic
Done.

307-308 lines
„the interaction of fractures and the following linkage/growth process overcomes the nucleation of new faults (Cowie et al., 1995)."
difficult to understand, consider reformulating
We reformulate the sentence as follows: "On the contrary, the interaction of fractures and the consequent linkage/growth process dominates over the nucleation of new faults providing a power-law distribution (Cowie et al., 1995)."

Table 1
1 line 3 column
give some very brief explanation for the "0.47" value – it is very small relatively to the values in the other lines
It is due to the higher image resolution of the Uruk Sulcus area that allows the identification of shorter lineaments.

322 line
"are defined for each histogram plot."
please modify to "are defined for each histogram plot (with red text)."
We modified as follows to be as complete as possible: "are defined for each histogram plot and outlined by green, blue, red and orange lines, respectively"

359 line
"and required for the development of densely populated grooves at the surface."
OK, but please explain briefly why
We reworded the sentence "Moreover, this suggests that this limit might be the potential thickness of the icy crust located above the deep ocean that during a phase of intense deformation and high strain rates may be cut across by very large faults".

364 line
„plateau stage of the local slope curve (green points)"
please indicate in the figure, what if somebody prints in black and white
We modified the Figure accordingly.

367 line
„The breaking point corresponds"
could you indicate these points with arrow

We displayed the breaking point with the gray stripe in Figure 8. The dot line centered in the grey stripe corresponds to the breaking point. It is better this type of representation in order to consider the associated error, too.

370 line
„all grooves system analysed"
consider to modify to „all groove systems analysed"
We modified it.

375 line
„and Uco, the upper"
please delete the comma
Done.

377 line
„reaching this maximum depth"
please specify which depth, where was this mentioned before
We modified as follows: "reaching this maximum depth (identified as U_{co})"

381 line
„by a hierarchical fracture network"
please also explain briefly this
A hierarchical fracture network means that we have first and second order structures. We reported it in the text.

391 line
„necking instability"
please explain
We added after necking instability the following statement: "(i.e. modelling Ganymede's lithosphere as a brittle surface layer underlain by a viscous half-space)".

392 line
„10-4 s-1 strain rate,"
please give some explanation, what this value represents or give some context, is it large or small, relatively to what etc.
We reported a wrong value, the right ones is 10^-13. We corrected it in the text, however this is the value that it is usually assumed in modelling and reported from literature.

424 line
„fitted by exponential length distribution"
some words would be useful for explanation
If the referee agrees, we prefer to keep this sentence since the overall explanation is reported in the discussion section.

425 line
„the occurrence of a"
is the „a" necessary?
We deleted it.

430 line

„analysed length”
consider to modify to „analysed the length”
We added it.

432 line
„grooves populations”
consider to modify to „groove populations”
We modified it.

434 line
„the Ganymede surface”
consider to modify to „the surface of Ganymede”
We modified it.

437 line
„are selected”
consider to modify to „are from selected”
We modified it.

439 line
„grooves, respectively”
please complete by at how large (km2) total surface area were these identified
The total surface area considered for the different four dataset is 1000km x 500km, but, if the referee agrees, we do not insert this information in the manuscript since it is not important for the conclusion.

448 line
„reaching the crust-ocean interface”
please discuss the above listed aspect (general comments) as curving, banding, diverging, transition to deformation etc. of fault lines along with the increasing depth
We discussed it as suggested in the general comments. We added few sentences, as reported in the answer to major points.

452 line
„different mechanical layers”
consider to modify to „layers with different mechanical properties”
We modified it.

460 line
please discuss the possible depth of the ocean or its scale based on your results
The possible depth coincides with the estimates of the icy shell thickness. To be as complete as possible, we added in the text icy crust above the liquid ocean in order to state that the found thickness corresponds to the depth at which the liquid ocean is located.

Figure 3 and 4
please consider to improve the readability of the labelling of different units at the bottom of the images, and also consider to make them more readable for black and white printed version
We modified the figure accordingly.

Reviewer #2: Interesting manuscript. Suggest minor revision before acceptance and final publication.

We thank the referee for the very valuable and constructive revision. We modified the manuscript accordingly satisfying all the requests made in the referee pdf file. Below, we answered to the major points and modify the text accordingly.

Some minor point to discuss:

-Are grooves brittle tectonic structures of the icy crust of Ganymede? Please discuss this point into the text and then use throughout the manuscript the same terminology. In fact, grooves / faults /fractures /faults underlying grooves are used as synonyms.
We reported in the Introduction section the following definition: "Grooves are the manifestation of brittle deformation of the light terrain (i.e. faults)."
Since grooves are the surface expression of brittle deformation we refer to them as faults in the manuscript and we modified it accordingly.
In the method section, we keep the terminology "fracture" referring to the National Research Council, 1996 definition.

- Do the Authors think the entire icy crust of Ganymede deforms/deformed in a brittle fashion? Discuss this point into the manuscript.
In our case we can have also a ductile ice layer that could behave as the brittle one depending on pressure and temperature. For this reason, we prefer to maintain the generic icy crust in the text because it could interest both brittle and ductile layers (since there is not yet a comprehensive understanding of the ice behavior on these bodies).
We expect that Ganymede icy crust behaves following the rheological distribution of the internal layering at depth that includes both brittle and ductile fashions. Similarly to the Earth crust, it is expected that a brittle-ductile transition occur on Ganymede icy crust. However, its location is still unknow although authors suggested it lies at 2-3 km at depth at the time of deformation (Nimmo and Pappalardo, 2004). The self-similar clustering considers the crust involved by fault/fracture penetration. In this way, both the behaviors (brittle and ductile) are included. The brittle portion is expected wider than the ductile portion, which also can be crosscut by vertical development of grooves.

- try to better explain why the upper cutoff limit of the power law distribution of the mapped grooves should represent the crustal thickness of the icy crust.
We rephrased the sentence regarding this concept as follows:
Indeed, it has been validated that the fractal clustering is controlled by the mechanical layering of the crust as observed for earthquakes and for fault networks at basin and plate scales (Pacheco et al., 1992; Davy, 1993; Ouillon et al., 1996). Moreover, it has been observed that the thickness of the fractured/deformed layer scales as the upper cut off value (U_{co}) characterizing the fracture network spatial organization (Mazzarini and D'Orazio, 2003; Mazzarini and Isola, 2010; Mazzarini et al., 2013).

-Even if I am not an English mother tongue I sometimes find the writing is a lit bit cumbersome. Please check English with a mother tongue colleague/specialist.
We checked the English with a mother tongue colleague to improve the writing.

-Some suggestions are provided to improve figs 2, 3, 4 5.
We modified and improved the Figures, as suggested by the referee.

-Carefully cross check cited reference and reference lists
We modified and corrected the reference list as suggested.

-Consider preparing a sketch to better explain the self similar clustering analysis to readers not familiar with this kind of quantitative (and effective!) approach.
We added the Figure 6, as suggested by the referee, to better explain the meaning of the fractal exponent.

-In the current form the conclusions are a short summary of the work. I think that in this chapter the Authors should present the main results and discuss the implication of these results for the wider audience.
We added sentences in the discussion and modified the conclusion paragraph according to the referee's suggestion reported in the referee pdf file.

Other comments are in the annotated pdf manuscript.
All the best!

Manuscript Details

Manuscript number	PSS_2020_130
Title	Equatorial grooves distribution on Ganymede: length and self-similar clustering analysis

Abstract

Grooves represent the evidence of tectonic activity that deformed Ganymede surface during its geologic evolution. In this work, we investigate the main characteristics of Ganymede's grooves populations on four different areas located at the equatorial region of the satellite (Uruk Sulcus, Babylon Sulci, Phrygia Sulcus and Mysia Sulci). Specifically, we analyse i) the grooves length distribution to provide a framework for their evolution and ii) the grooves self-similar clustering to infer their vertical penetration inside Ganymede icy shell. For each dataset, we find that the grooves distribution is well fitted by an exponential-law and a power-law distribution depending on the structure length. This implies the presence of confined structures in a shallow layer of the icy crust (shorter, exponentially-fitted structures) and crustal-scale structures that could theoretically reach the crust-ocean interface (large, power law-fitted structures). The thickness of the penetrated icy shell is retrieved through the self-similar clustering analysis and ranges between 105 and 130 km for the examined datasets. This value agrees with independent estimates of the icy shell thickness, ranging between 80 and 150 km. Moreover, our results support the hypothesis that a large number of grooves penetrate the brittle icy crust, with sets of fractures vertically confined in different mechanical layers, while the penetration of few interconnected faults underlying longer grooves may interest the whole icy crust above the liquid ocean.

Submission Files Included in this PDF

File Name [File Type]

Lucchetti_highlights.docx [Highlights]

Lucchetti_Ganymede_paper_11May.docx [Manuscript File]

Lucchetti_Ganymede_Supplementary_Material_11May.docx [Supplementary Material]

To view all the submission files, including those not included in the PDF, click on the manuscript title on your EVISE Homepage, then click 'Download zip file'.

Research Data Related to this Submission

There are no linked research data sets for this submission. The following reason is given:
Data used in this work are those published by Rossi et al., (2020).

Highlights

- Ganymede's grooves are the representation of a hierarchical system
- Shorter grooves are vertically confined in the brittle icy crust
- Longer grooves are crustal-scale structures theoretically reaching the crust-ocean interface
- The icy shell thickness interested by grooves penetration is between 105 and 130 km

Equatorial grooves distribution on Ganymede: length and self-similar clustering analysis

A. Lucchetti[1], C. Rossi[2], F. Mazzarini[3], M. Pajola[1], R. Pozzobon[4], M. Massironi[4], G. Cremonese[1]

[1]INAF-Astronomical Observatory of Padova, Padova, Italy (alice.lucchetti@inaf.it); [2]INFN - Laboratori Nazionali di Frascati, Frascati (Roma), Italy; [3]INGV- National Institute of Geophysics and Volcanology, Pisa, Italy; [4] Geoscience Department, University of Padova, Padova, Italy.

Abstract

Grooves represent the evidence of tectonic activity that deformed Ganymede surface during its geologic evolution. In this work, we investigate the main characteristics of Ganymede's grooves populations on four different areas located at the equatorial region of the satellite (Uruk Sulcus, Babylon Sulci, Phrygia Sulcus and Mysia Sulci). Specifically, we analyse i) the grooves length distribution to provide a framework for their evolution and ii) the grooves self-similar clustering to infer their vertical penetration inside Ganymede icy shell. For each dataset, we find that the grooves distribution is well fitted by an exponential-law and a power-law distribution depending on the structure length. This implies the presence of confined structures in a shallow layer of the icy crust (shorter, exponentially-fitted structures) and crustal-scale structures that could theoretically reach the crust-ocean interface (large, power law-fitted structures). The thickness of the penetrated icy shell is retrieved through the self-similar clustering analysis and ranges between 105 and 130 km for the examined datasets. This value agrees with independent estimates of the icy shell thickness, ranging between 80 and 150 km. Moreover, our results support the hypothesis that a large number of grooves penetrate the brittle icy crust, with sets of fractures vertically confined in different mechanical layers, while the penetration of few interconnected faults underlying longer grooves may interest the whole icy crust above the liquid ocean.

1. Introduction

Ganymede is the largest of the four Jupiter's satellites with a diameter ~5262 km (Anderson et al., 2001). Its unique characteristics were first investigated by two flybys of Voyager 1 and 2 in 1979 (Smith et al., 1979a, 1979b) and subsequently, by the remote sensing instruments onboard Galileo between 1995 and 2003 (Russell et al., 2012). Ganymede was found to be the only solid body in the outer Solar System that owns an internal dynamo field (Kivelson et al., 1997). Moreover, it was discovered that Ganymede hosts a subsurface ocean (Kivelson et al., 2002). The thickness of the differentiated layers of the satellite's interior is still under investigation, even if the outer icy crust above the liquid ocean has been suggested to be 120-170 km thick (Kivelson et al., 2002; Sohl et al., 2002; Kuskov, 2005; Hussmann et al., 2007; Saur et al., 2015). The presence of a subsurface global ocean has important implications in constraining the evolutionary history of the satellite and its internal dynamics directly affecting its surface, as testified by the widespread tectonic structures.

The uniqueness of this satellite was also revealed by its surface appearance. Indeed, Ganymede's surface is subdivided into two geological domains distinguishable by albedo, morphology and crater density: dark and light terrains (Smith et al., 1979a, 1979b; Shoemaker et al. 1982; Pappalardo et al., 2004; Patterson et al., 2010; Collins et al., 2013). The heavily cratered dark terrain covers 35% of the surface of the satellite (Shoemaker et al., 1982; Murchie et al., 1986, 1989; Neukum, 1997; Neukum et al., 1998; Prockter et al., 1998; Zahnle et al., 2003; Schenk et al., 2004) and it is characterized by large-scale, arcuate fracture systems termed furrows, that have been hypothesized to be the remnants of former multiring basins (McKinnon & Melosh, 1980; Murchie et al., 1990; Prockter et al., 1998; Schenk & McKinnon, 1987). A thin deposit overlying the bright icy material may be responsible for the darkness of the terrain (Casacchia and Strom, 1984; Croft and Strom, 1985, Allison and Clifford, 1987; Figueredo et al., 1999; Moore et al., 1999; Prockter et al., 2000), that is estimated to be > 4 Gyr old (Zahnle et al., 2003). The remaining 65% of the surface is covered by bright terrains which are less densely cratered, younger, heavily tectonized and mainly constituted by longitudinal swaths termed "Sulci" and polygons several tens of kilometers across (Lucchitta, 1980; Patterson et al.,

2010). The light terrain may have been emplaced between 2 Gyr or even up to 4 Gyr ago, depending on the cratering model chronology used (Zahnle et al., 2003), and it is characterized by the presence of linear features called grooves (Murchie et al., 1986; Pappalardo et al., 1998; Prockter et al., 2000; Collins, 2009). Grooves are regional-scale morphotectonic structures (e.g. fractures, faults), from linear to curvilinear, that represent the brittle deformation of the light terrain (Lucchitta, 1980; Bianchi et al., 1986; Pappalardo & Greeley, 1995; Pappalardo et al., 1998, 2004). The proposed tectonic processes responsible for the groove formation include extension, e.g. horst-and-graben normal faulting pulling the terrain apart (Shoemaker et al., 1982; Belton et al., 1996, Pappalardo et al., 1998; Dombard and McKinnon, 2001; Bland and Showman, 2007), and strike-slip kinematics (e.g. Pappalardo et al., 1998, Cameron et al., 2018). In addition to these processes, local resurfacing by tectonism (Head et al., 2002) and cryovolcanic flows (Schenk and McKinnon., 2001; Showman et al., 2004) may contribute to the actual groove morphology.

Grooves represent the evidence of tectonic activity that deformed the satellite surface during its geologic evolution and may have played a key role in the possible connection between surface and the subsurface ocean (Head et al., 2002). In this context, the analysis of Ganymede deformed surface could provide hints regarding its interior, as well as its ice shell's mechanical behaviour. Indeed, faults distribution and fault populations on icy satellites can reveal insights into the evolution of their surface that cannot be gained with other techniques. In particular, statistical characterization of fault-population attributes, such as length and clustering, are fundamental means to explore deformation rates, stress transmission modes, rheology of the medium, and mechanical layering (Benedicto et al. 2003; Soliva and Schultz, 2008; Gudmundsson et al. 2010, 2011; Schultz et al. 2010; Gudmundsson et al. 2013). The fractal analysis has been used in terrestrial planets studies to determine the thickness of the fractured crust (e.g., Mazzarini and D' Orazio, 2003; Mazzarini, 2004; Soliva and Schultz, 2008; Mazzarini and Isola, 2010; Pozzobon et al. 2015). In the same fashion, on icy satellites the exploration of the depth at which fractures penetrate the icy layer could be constrained investigating

78 the main characteristics of fault populations, such as length size-distribution and clustering (Lucchetti
79 et al., 2017).
80 In this work, we analyse the grooves' length and spatial distribution (Bonnet et al., 2001; Bour
81 et al., 1999; Bour et al., 2002 ; Gudmundsson et al., 2013) to estimate the potential thickness of the
82 icy crust above the deep ocean required to develop densely populated structures at the surface of
83 Ganymede (i.e. the grooves). After analysing the global grooves distribution, we investigate the
84 behaviour of four regions located on the equatorial area of the satellite. Then, we analyse the grooves
85 length distribution and self-similar clustering providing the vertical extension of grooves penetration
86 inside Ganymede icy shell.
87
88 **2. Dataset**
89 Ganymede imagery coverage comes from the data acquired by both the Wide Angle Camera (WAC)
90 and Narrow Angle Camera (NAC) onboard Voyager 1 and 2 and the Solid State Imaging (SSI, Belton
91 et al., 1992) camera onboard Galileo spacecraft. Specifically, the subjovian hemisphere was imaged
92 by Voyager 1 with a resolution up to 1 km/px, while the antijovian hemisphere was imaged by
93 Voyager 2 with a resolution up to 500 m/px. The leading and trailing hemisphere were imaged with
94 a resolution of 2 km/px and 3.6 km/px respectively by distant encounters of Ganymede during the
95 Galileo Jupiter tour to fill the Voyager coverage gaps (Carr et al., 1995). In addition, the six Galileo
96 close encounters with Ganymede allowed the acquisition of high-resolution images (100 m/px and
97 better) by the SSI camera. Based on these remote sensing data, the United States Geological Survey
98 (USGS) Astrogeology Science Centre assembled a global image mosaic of the surface resampled at
99 1 km/px (Becker et al., 2001, Figure 1). The map was derived combining reasonable input resolution
100 images (from 20 km/px for gap fill to approximately 400 m/px) and works for the global mapping of
101 grooves.
102 Ganymede grooves are located on four different types of light material units (Collins et al.,
103 2013): light irregular material, light subdued material, light grooved material and undivided light

material (Figure 1). The light irregular material exhibits a mixture of both smooth and grooved surfaces with a relatively high to moderate albedo and it is characterized by grooves with irregular orientation and spacing. The light subdued material is thought to be representative of the early stage grooved terrain formation, hence displaying smooth surface and faint lineaments with similar spacing and orientation. The light grooved material likely formed through the modification and deformation of pre-existing materials, such as the light subdued material or dark terrain and it is mainly characterized by similarly spaced and oriented areas of closely packed troughs and lineaments. Finally, the light undivided material is identified when the other three terrains cannot be discerned (Collins et al., 2013). Three different relative age have been identified for each light terrain, except for the undivided light terrain (Patterson et al., 2010; Collins et al., 2013).

Grooved terrains represent the deformation of Ganymede's light terrains: they exhibit two superposed scales of grooves with different structure spacing and length (Patterson et al., 2010). The local scale provides spacing between the structures < 5 km and length < 50 km, while grooves identified at the regional scale are usually clustered in sets of grooves with length > 100 km and average spacing of about 10 km, often displaying parallel ordered patterns (Bianchi et al., 1984; Casacchia & Strom, 1984; Collins et al., 2000, 2013; Lucchitta, 1980; Pappalardo et al., 1998, 2004; Pappalardo & Greeley, 1995; Patterson et al., 2010).

Our analysis is based on the regional scale grooves mapping (Rossi et al., 2020) that represents a useful dataset to improve the knowledge of the tectonic evolution of the satellite and to recognize the main characteristics of these features (Figure 1). In particular, grooves on Ganymede were manually mapped on the global image mosaic (Becker et al., 2001) between 60°N and 60°S and digitized in a geographic information system (GIS) geodatabase (Rossi et al., 2020). Due to the limitation of illumination and resolution conditions of the Ganymede mosaic, grooves were mapped on approximately 36% of the light terrain. As reported in Rossi et al., (2020), mapped grooves are considered as the topographic expression of trough structures recognizing their bottom thanks to the luminosity contrast resulting from the solar lighting conditions.

Thanks to these comprehensive grooves mapping dataset, we were able to select four different type-regions located on the equatorial belt of Ganymede. The choice is based on the high density and homogeneous spatial distribution of the grooves located on those regions, which is necessary for the following analysis. The four datasets are in selected regions located in Uruk Sulcus, Babylon Sulci, Phrygia Sulcus and Mysia Sulci, respectively (Figure 2-5). Uruk Sulcus is centered at 0.8°N, 200°E, and exhibits different intersecting bands of light units characterized by various tectonism mechanisms, such as normal faulting, graben, domino-style faulting (Pappalardo et al., 1998; Cameron et al., 2018) and transpressional strike-slip faulting (Rossi et al., 2018). The number of grooves of the selected area is 1068 (Figure 2). The area selected in Babylon Sulci is centered at 0°N, 290°E, as shown in Figure 3, and it is constituted by 882 grooves. Babylon Sulci has been inferred as an example of strike-slip setting, where groove super-system delineates longer and sub-parallel grooves that enclose shorter grooves with different directions (Rossi et al., 2020). A similar regional setting is found in Phrygia Sulcus. Here, we selected an area centered at 15°N, 355°E and containing about 678 grooves (Figure 4). Finally, the fourth dataset is located in Mysia Sulci and centered at 7°N, 20°E and it is constituted by 987 grooves structures (Figure 5).

Figure 1: A-B) Orthographic projection of the global image mosaic of Ganymede centered at 0°N, 0°E and at 0°N, 180°E, respectively (available at https://astrogeology.usgs.gov). C-D) The orthographic projection of the Collins et al. (2013) published global geological map of Ganymede. The legend refers to the light terrain units where grooves were mapped: light subdued unit (*ls1, ls2, ls3*), light irregular unit (*li1, li2, li3*), light grooved unit (*lg1, lg2, lg3*) and light undivided unit (*l*) (Collins et al., 2013). E-F) The orthographic projection of the mapped grooves performed on Ganymede image mosaic by Rossi et al., (2020). The total number of identified grooves structures (in orange) is 14,707 between 60°N and 60°S region. All maps report the Sulci names of the selected regions used in our analysis.

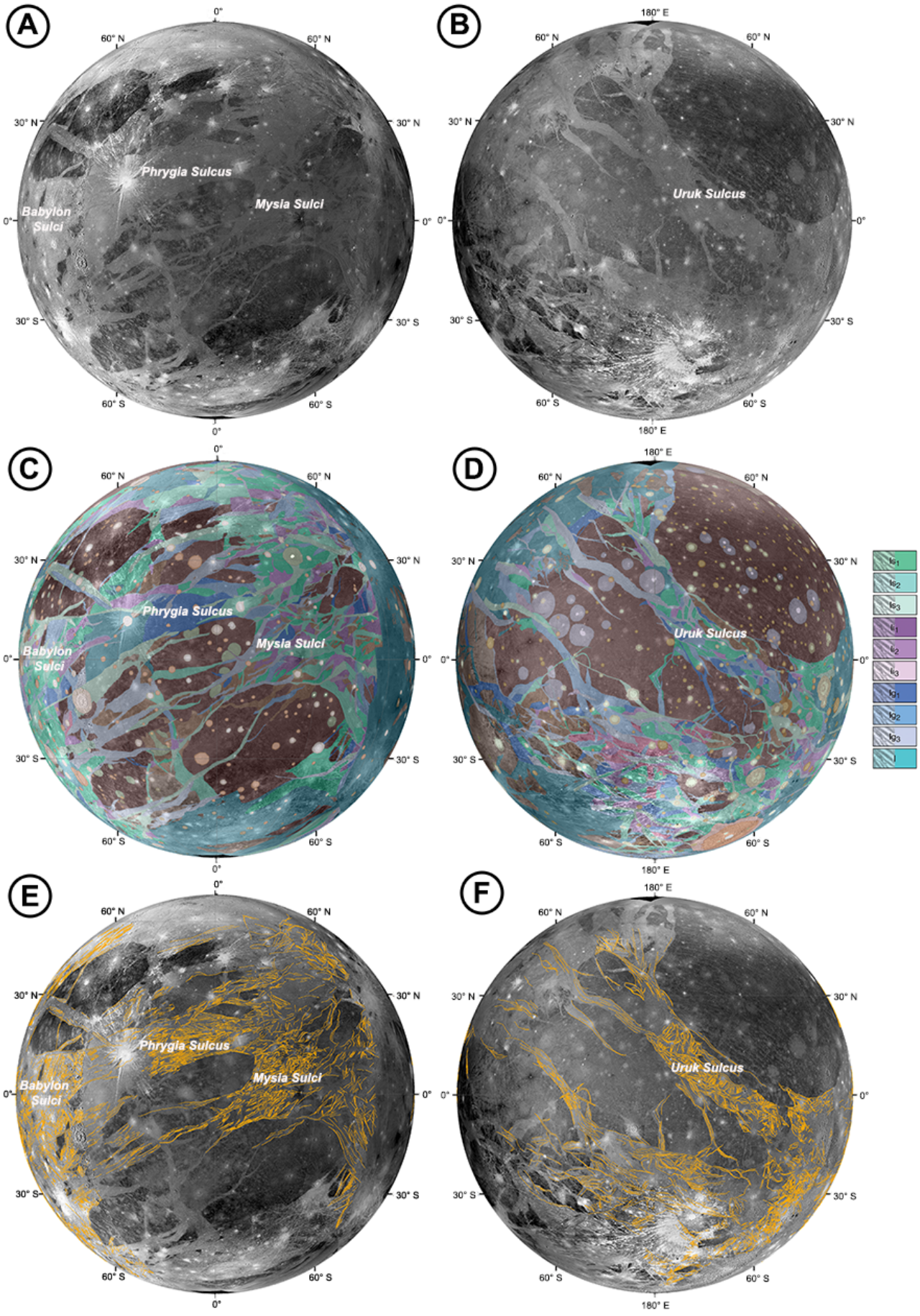
A
B
C
D
E
F
Phrygia Sulcus
Mysia Sulci
Babylon Sulci
Uruk Sulcus
0°
60° N
30° N
30° S
60° S
180° E

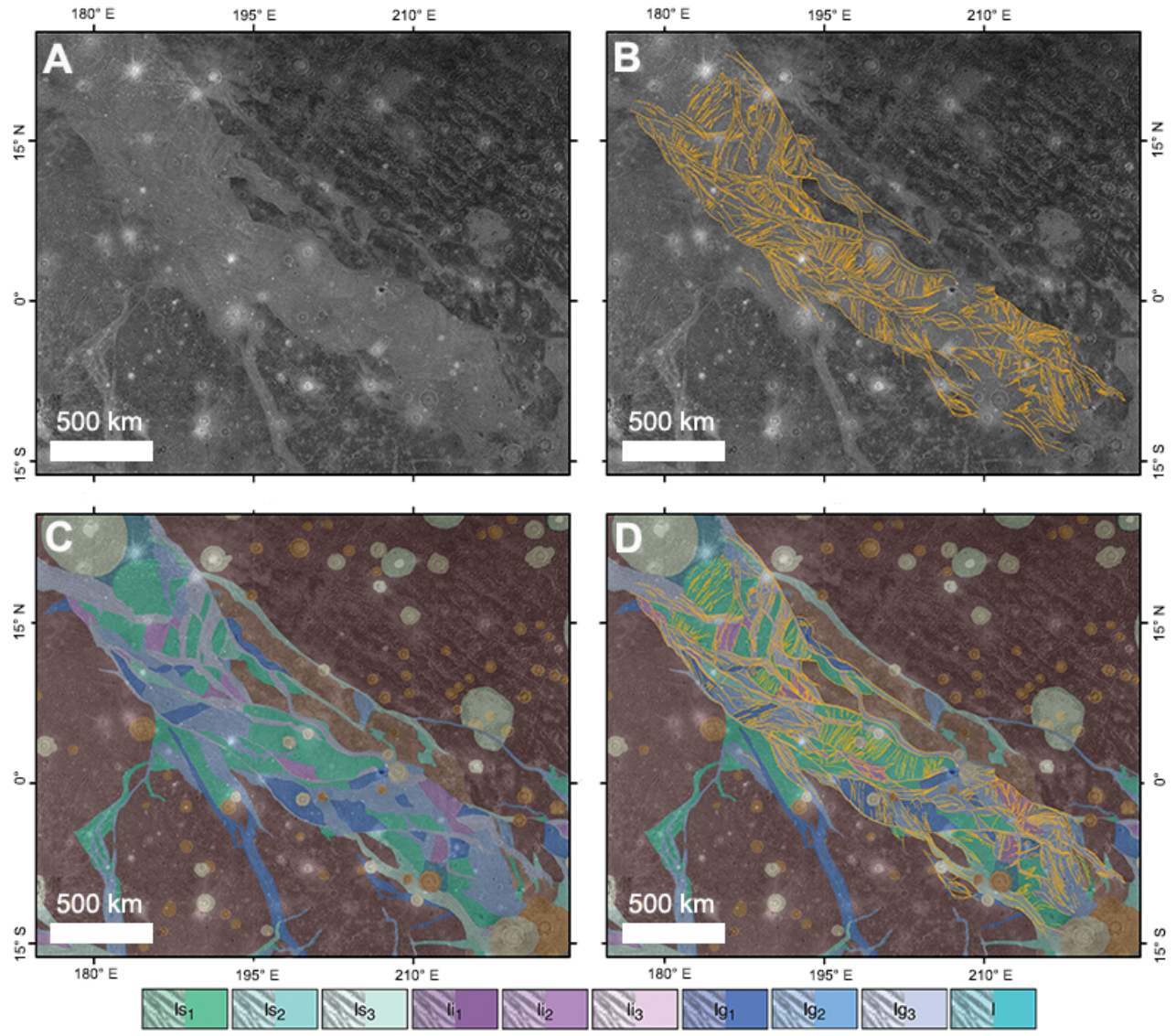

Figure 2: Grooves selected in Uruk Sulcus area in the region centered at 0.8°N, 200°E. A) Ganymede base map (Ganymede Voyager - Galileo SSI Global Mosaic Ganymede, available at https://astrogeology.usgs.gov) representing the area of Uruk Sulcus under study. B) The number of grooves mapped (Rossi et al., 2020) and selected for the analysis is 1068. C) The geological map of Collins et al., (2013) overlaid in transparency on the base map. D) The grooves mapped are overlaid on the geological map. The legend represents the geological units corresponding to the light terrain on which grooves were mapped (light subdued unit: *ls1, ls2, ls3*, light irregular unit: *li1, li2, li3*, light grooved unit: *lg1, lg2, lg3* and light undivided unit *l*). For nomenclature and interpretation of the geological units, we refer the reader to Collins et al., (2013).

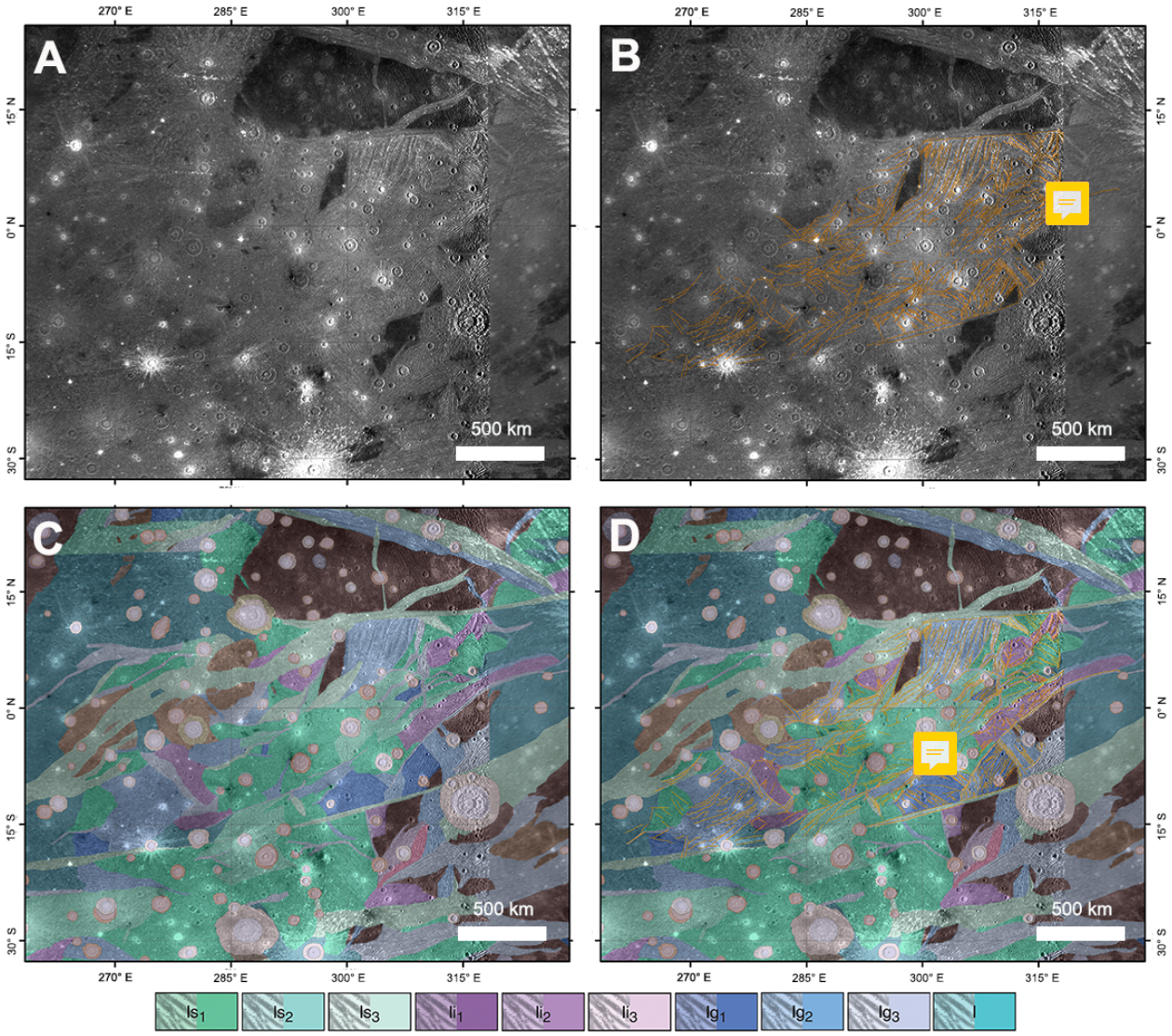

Figure 3: Grooves selected in Babylon Sulci area in the region centered at 0°N, 290°E. A) Ganymede base map (Ganymede Voyager - Galileo SSI Global Mosaic Ganymede, available at https://astrogeology.usgs.gov) representing the area of Babylon Sulci under study. B) The number of grooves mapped (Rossi et al., 2020) and selected for the analysis is 882. C) The geological map of Collins et al., (2013) overlaid in transparency on the base map. D) The grooves mapped are overlaid on the geological map. The legend represents the geological units corresponding to the light terrain on which grooves were mapped (light subdued unit: *ls1, ls2, ls3*, light irregular unit: *li1, li2, li3*, light grooved unit: *lg1, lg2, lg3* and light undivided unit *l*). For nomenclature and interpretation of the geological units, we refer the reader to Collins et al., (2013).

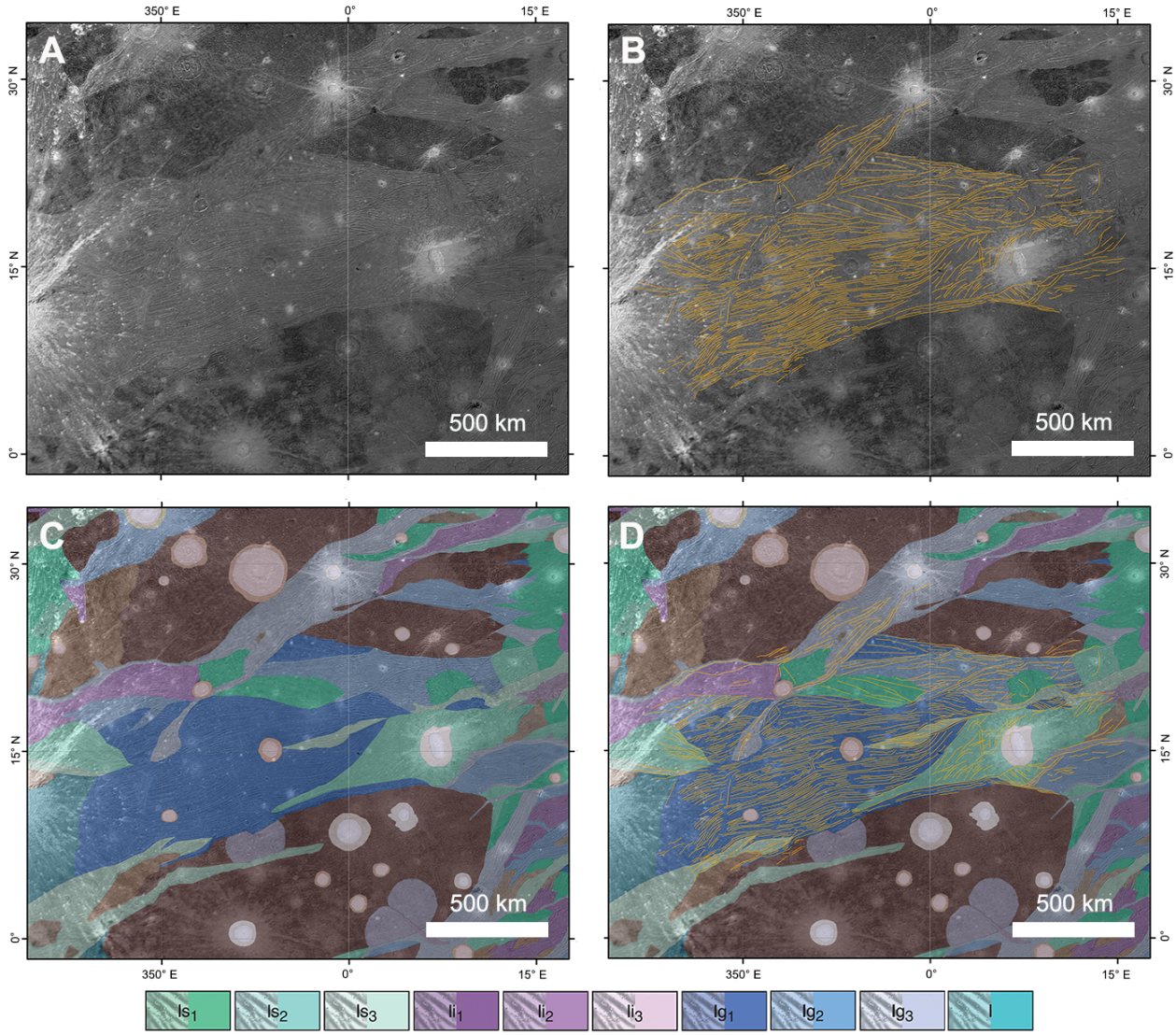

Figure 4: Grooves selected in Phrygia Sulcus area in the region centered at 0.8°N, 200°E. A) Ganymede base map (Ganymede Voyager - Galileo SSI Global Mosaic Ganymede, available at https://astrogeology.usgs.gov) representing the area of Phrygia Sulcus under study. B) The number of grooves mapped (Rossi et al., 2020) and selected for the analysis is 678. C) The geological map of Collins et al., (2013) overlaid in transparency on the base map. D) The grooves mapped are represented overlaid on the geological map. The legend represents the geological units corresponding to the light terrains on which grooves were mapped (light subdued unit: *ls1, ls2, ls3*, light irregular unit: *li1, li2, li3*, light grooved unit: *lg1, lg2, lg3* and light undivided unit *l*). For nomenclature and interpretation of the geological units, we refer the reader to Collins et al., (2013).

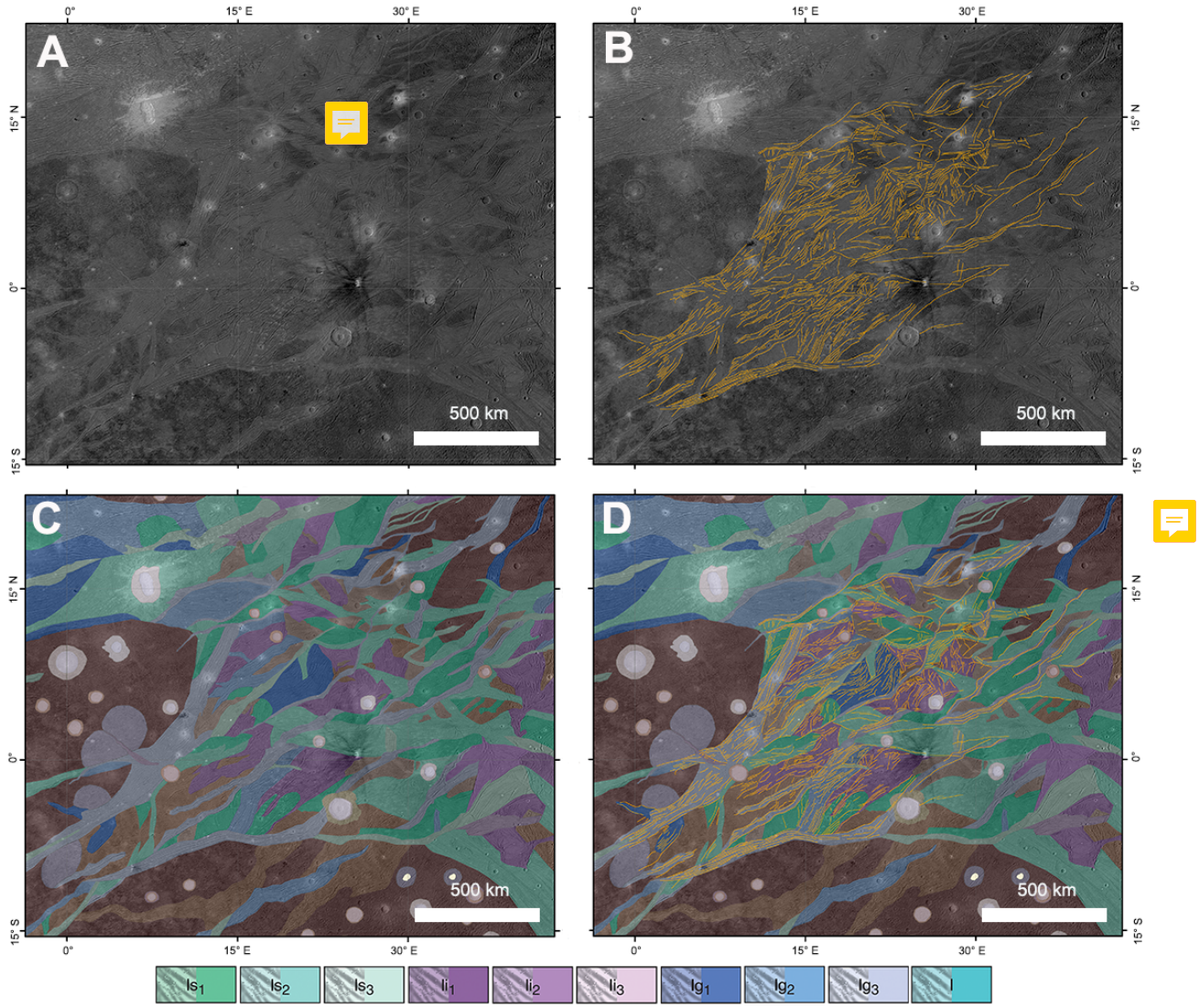

Figure 5: Grooves selected in Mysia Sulci area in the region centered at 7°N, 20°E. A) Ganymede base map (Ganymede Voyager - Galileo SSI Global Mosaic Ganymede, available at https://astrogeology.usgs.gov) representing the area of Mysia Sulci under study. B) The number of grooves mapped (Rossi et al., 2020) and selected for the analysis is 987. C) The geological map of Collins et al., (2013) overlaid in transparency on the base map. D) The grooves mapped are represented overlaid on the geological map. The legend represents the geological units corresponding to the light terrain on which grooves were mapped (light subdued unit: *ls1, ls2, ls3*, light irregular unit: *li1, li2, li3*, light grooved unit: *lg1, lg2, lg3* and light undivided unit *l*). For nomenclature and interpretation of the geological units, we refer the reader to Collins et al., (2013).

3. Methods

Fault population statistics can be analysed in terms of its size and spatial distribution (e.g., Soliva and Schultz, 2008; Schultz et al., 2010; Mazzarini et al., 2013; Lucchetti et al., 2017). Size distribution focuses on the properties of geometric features such as fault length, spacing and displacement, while spatial distribution investigates the properties of the whole population such as fault density and clustering. We here report the two approaches used in this work to analyse Ganymede's grooves.

3.1 Length Distribution analysis

The propagation and eventual deep confinement of a fault system is usually described by the analysis of length distribution (e.g. Soliva and Schultz, 2008; Schultz et al., 2010; Mohajeri and Gudmundsson, 2012; Gudmundsson et al., 2013) that usually follow two different trends: exponential law distribution and power law distribution. The first one is represented by the following equation:

$$N(>l) = \beta e^{-\lambda l},$$

where β and λ are the parameters of the exponential distribution and l the fault length, while the second one is represented by:

$$N(>l) = c l^{-\alpha},$$

where c is the scaling factor, α the exponent of the power-law distribution and l is the fault length. The mechanical layering of the crust, as well as a sufficiently large contrast in material properties existing between layers, governs the vertical dimension of a fault (height) that is, in turn, nearly proportional to fault length (e.g., Benedicto et al., 2003; Gudmundsson et al., 2010; Soliva and Schultz, 2008). In this scenario, analysis of faults' length distribution usually identifies two end-members (e.g., Soliva and Schultz, 2008; Schultz et al., 2010): (i) fault populations of regularly spaced faults derived from strain partitioning within a single mechanical layer are confined in depth and are generally characterized by negative exponential distribution (e.g., Cowie et al., 1994; Ackermann et al., 2001); (ii) fault systems, with few large well separated faults cutting across the whole crust displaying a power-law distribution. Since planetary crusts are often affected by long

tectonic and fracturing histories reworking preexisting discontinuities, as well as internal strain partitioning, it is not unusual to retrieve distributions where the same fault population shows different kind of distributions as a function of the fault length.

3.2 Self-similar Clustering analysis

A robust way to define how fractures fill space (i.e. fracture spatial distribution) is to analyse their self-similar clustering (Bonnet et al., 2001). Through this methodology it is possible to infer the vertical extension of the connected fractures network starting from the observation of fractures and, then to evaluate the scaling properties of the system (Mazzarini and Isola, 2010). The self-similar clustering of fractures is performed for a range of lengths (the size range) between a lower and an upper cutoff (L_{co} and U_{co}, respectively) by applying the two-point correlation function method to measure the fractal dimension of the fracture population. L_{co} and U_{co} are scale-invariant characteristics of fractures depending on both the resolution of the methods used to map and detect fractures (L_{co}) and the mechanical layers and rock properties (U_{co}) (Mandelbrot et al., 1982). Indeed, it has been validated that the thickness of the fractured/deformed layer is mirrored by the occurrence of a threshold value (upper cut –off) in the size of the fracture network spatial organization (Pacheco et al., 1992; Davy, 1993; Ouillon et al., 1996; Mazzarini and D'Orazio, 2003; Mazzarini and Isola, 2010; Gudmundsson et al., 2010; Gudmundsson et al., 2011, Mazzarini et al., 2013).

For a population of N points (fracture's trace barycenter) the correlation integral *C(l)* is defined as the correlation sum that accounts for all the points located at a distance of less than a given length *l* (Hentschel and Procaccia, 1983) by the following equation:

$$C(l)=2N(l)/N(N-1),$$

where *N(l)* is the number of pairs of points whose distance is less than *l*. The self-similar clustering is performed exploiting the following scaling law:

$$C(l)\sim l^{D}$$

where *D* is the fractal exponent defined as the slope of the tangent to the *log(C(l)) vs. log(l)* curve. Self-similarity exists within a size range, bounded by a L_{co} and a U_{co}, that is detectable as a linear fit (a plateau) in a *local slope* diagram: the wider the range, the better the computation of the power-law distribution (Walsh and Watterson, 1993). The local slope is a point by point measure of the slope of the tangent to the curve:

local slope = $\Delta log(C(l))/\Delta log(l)$.

The derivation of the cut-offs defining the size range is not trivial, especially when the local slope does not show a regular and wide plateau. The choice of L_{co} and U_{co} was estimated by selecting the wider length range for which the correlation between *Log(C(l)) vs Log(l)* is greatest by applying the ordinary least squares fit method (Mazzarini, 2004). By knowing that the fractal behaviour is valid until a significant break in the local slope occurs, we estimate the R^2 value corresponding to the breaking point.

4. Results and Discussion

We analysed the grooves following the methodology explained in the previous section. Firstly, we obtained the length-frequency histograms for ~~each region and corresponding grooves' network considered,~~ as shown in Fig. 6A-D.

The minimum and maximum length of the 1068 grooves located in Uruk Sulcus are 0.47 km and 582 km, respectively. The mean is 62.7 km while the median length is 48 km (Figure 6A). The grooves length size range for Babylon Sulci is between 7.2 and 656 km with a mean and a median length of 77.8 km and 57.9 km, respectively (Figure 6B). Phrygia Sulcus is characterized by a range size of 8.9 - 559 km and a mean and median length of 95.9 and 72.1 km, respectively (Figure 6C). ~~Finally~~ the minimum and maximum length of Mysia Sulci are 6.5 and 496 km with an associated mean and median length of 66 km and 47 km (Figure 6D). As outlined in the histograms, there is a small number of grooves with length < 20 km. This suggests that our datasets may be affected by truncation bias and implies that small grooves were hardly detectable on a regional scale. Indeed,

faults analyses are usually characterised by the presence of an upper and a lower bias affecting the measurements. The first is referred to as "censoring", which occurs when the sample size exceeds the dimensions of the measurement area, hence implying the underestimation of the sample size. On the contrary, the second is known as "truncation" and it is related to the image resolution that may lead to small samples undercounting.

After calculating the statistical attributes of grooves, we obtained the length cumulative plot for each grooves' network (Figure 6E-H). This analysis reveals that such distribution is characterized by different fitting curves. Indeed, the cumulative plot presents a single or multiple exponential distributions for lengths shorter than L_{th} (length threshold), while there is a power-law distribution for grooves longer than L_{th}. The presence of both the exponential and power-law trends reflect the possible coexistence of (i) distributed fault systems, with strain regularly partitioned along evenly spaced faults and confined within specific mechanical layers in the crust (exponential fitting curve/curves) and (ii) localized fault systems, with few large faults cutting across the whole crust (power-law fitting curve) (e.g., Soliva and Schultz, 2008; Schultz et al., 2010). In addition, the existence of two exponential distributions for three datasets suggest that there could be two differently confined structure systems within specific mechanical crust layers.

We underline that, even if the number of samples (from 50 up to 200) fitted by a power-law is not as numerous as the ones characterized by the exponential fitting, we are confident about such distribution. Indeed, it is well known that even if the data follow a power-law distribution, it does not mean that the power-law necessarily provides the best model or fit for the data (Clauset et al., 2009; Mohajeri and Gudmundsson, 2012). For this reason, we tested the power-law distribution using the program Matlab and the statistical programing language R following the procedure of Clauset et al., (2009) (see Supplementary Material). This approach validates the existence of the power-law distribution, confirming the presence of a L_{th} separating the exponential and the power-law fitting models. The L_{th} is 93.8 km, 148 km, 238.7 km, 185 km for Uruk Sulcus, Babylon Sulci, Phrygia

Sulcus and Mysia Sulci, respectively. The calculated distribution for each dataset is reported in Table 1.

These findings may represent the evolutional history of fault linkages underlying the Ganymede grooves, where the transition between the exponential and power-law length-frequency distributions is connected to the fault growth in a vertically confined medium. The grooves exponential behaviour is representative of both the nucleation of new faults during incipient phases of propagation (when mechanical layering does not have any influence) and the saturation of a vertical confined system of structures (Schultz et al., 2010; Cowie *et al*., 1994; Ackermann et al., 2001). On the contrary, the power-law trend occurs when the interaction of fractures and the following linkage/growth process overcomes the nucleation of new faults (Cowie et al., 1995).

Dataset	N	l range (km)	l_{th} (km)	Distribution (N>l)		
				Exponential ($l<l_{th}$)		Power-law ($l>l_{th}$)
Uruk Sulcus	1068	0.47 - 582	93.8	$\propto e^{-0.47\,l}$ $R^2 = 0.989$		$\propto l^{-2.66}$ $R^2 = 0.998$
Babylon Sulci	882	7.2 – 646	148	$\propto e^{-0.48\,l}$ $R^2 = 0.991$ ($l < 80$km)	$\propto e^{-0.37\,l}$ $R^2 = 0.994$ ($l > 80$km)	$\propto l^{-2.96}$ $R^2 = 0.996$
Phrygia Sulcus	678	8.9 – 559	238.7	$\propto e^{-0.52\,l}$ $R^2 = 0.992$ ($l < 140$km)	$\propto e^{-0.2\,l}$ $R^2 = 0.993$ ($l > 140$km)	$\propto l^{-4.35}$ $R^2 = 0.986$
Mysia Sulci	987	6.5 – 496	185	$\propto e^{-0.51\,l}$ $R^2 = 0.989$ ($l < 90$km)	$\propto e^{-0.22\,l}$ $R^2 = 0.985$ ($l > 90$km)	$\propto l^{-3.46}$ $R^2 = 0.992$

Table 1: Parameters for each length size distribution of the selected area, where *N* is the number of grooves, *l range* is defined between the minimum and maximum length value in km and l_{th} the threshold length value discerning between the exponential and power-law distribution of length's grooves. The last two columns reported the exponential and power-law fitting models found for the selected region, as shown in Figure 6.

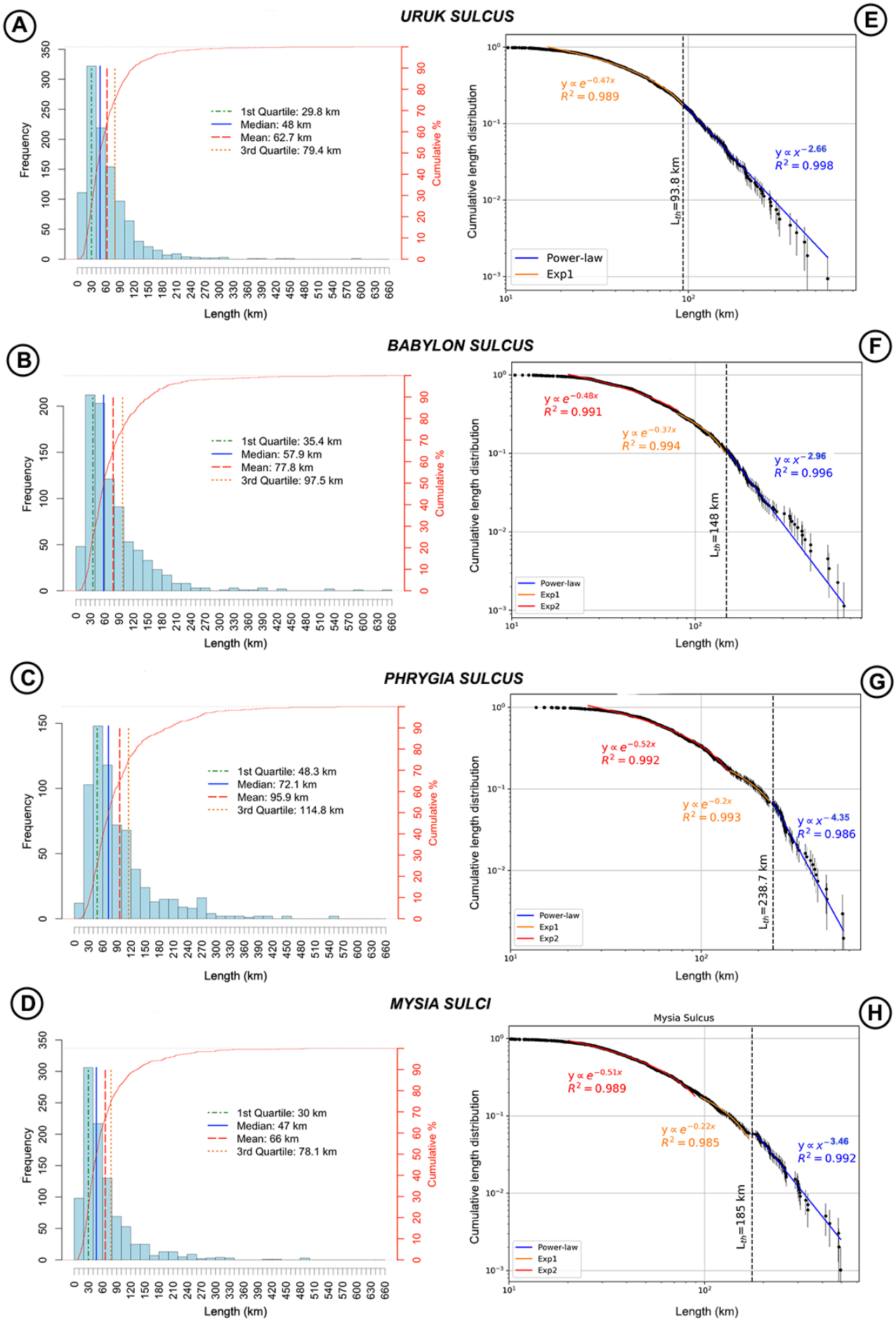
A
URUK SULCUS
E
1st Quartile: 29.8 km
Median: 48 km
Mean: 62.7 km
3rd Quartile: 79.4 km
Frequency
Cumulative %
Length (km)
$y \propto e^{-0.47x}$
$R^2 = 0.989$
$y \propto x^{-2.66}$
$R^2 = 0.998$
L_{th}=93.8 km
Cumulative length distribution
Power-law
Exp1
B
BABYLON SULCUS
F
1st Quartile: 35.4 km
Median: 57.9 km
Mean: 77.8 km
3rd Quartile: 97.5 km
$y \propto e^{-0.48x}$
$R^2 = 0.991$
$y \propto e^{-0.37x}$
$R^2 = 0.994$
$y \propto x^{-2.96}$
$R^2 = 0.996$
L_{th}=148 km
Power-law
Exp1
Exp2
C
PHRYGIA SULCUS
G
1st Quartile: 48.3 km
Median: 72.1 km
Mean: 95.9 km
3rd Quartile: 114.8 km
$y \propto e^{-0.52x}$
$R^2 = 0.992$
$y \propto e^{-0.2x}$
$R^2 = 0.993$
$y \propto x^{-4.35}$
$R^2 = 0.986$
L_{th}=238.7 km
D
MYSIA SULCI
H
Mysia Sulcus
1st Quartile: 30 km
Median: 47 km
Mean: 66 km
3rd Quartile: 78.1 km
$y \propto e^{-0.51x}$
$R^2 = 0.989$
$y \propto e^{-0.22x}$
$R^2 = 0.985$
$y \propto x^{-3.46}$
$R^2 = 0.992$
L_{th}=185 km

Figure 6: Length distribution analysis of A) Uruk Sulcus, B) Babylon Sulci, C) Phrygia Sulcus and D) Mysia Sulci. On the left column the length histograms (bin size =15 km) are reported, while on the right column the length cumulative plots for each dataset are presented. The statistical attributes, such 1st quartile, median, mean and 3rd quartile values, are defined for each histogram plot. The fitting models of cumulative length distribution are shown on the graphs (E-H) and reported in Table 1. Grooves shorter than the threshold length L_{th} (black dashed line) are fitted by exponential distributions (red and orange curves), while grooves longer than L_{th} are fitted by a power-law distribution (blue curve).

The self-similar clustering analysis indicate that the spatial organization of grooves in each data sets is bounded in a size range with a well-defined upper cutoff. The plateau in the fractal distribution has been inferred from the analysis of the *Log(C(l)) vs Log(l)* diagram (Bonnet et al., 2001) and its validity is bounded by a size range (L_{co} and U_{co}) detectable as a linear fit (plateau) in the *local slope vs Log(l)* diagram (Walsh and Watterson, 1993, Figure 7). The choice of L_{co} and U_{co} was estimated by selecting the wider length range for which the correlation between *Log(C(l))* *Log(l)* (black points in Figure 7) is greatest, by applying the ordinary least squares fit method. Hence, the quality of the correlation was assessed using the coefficient of R^2 determination detecting the size range corresponding to the higher value of R^2. To ensure the reliability of the results, we also cross check the *local slope vs Log(l)* (green points in Figure 7) diagram with R^2 values for all possible size range combination *ΔLog(l)*. Higher R^2 value results in higher reliability of the information. Hence, this analysis validates the robustness of the L_{co} and U_{co} estimates. Moreover, the large number of samples used ensures robust estimates of the parameters with an error < 1% (as reported in Mazzarini and Isola 2010). Nevertheless, the L_{co} is very sensitive to the measurement truncation bias, which is in turn correlated with the image resolution. Given that the plateau is rather noisy close to the L_{co}, we do not attribute a reliable significance on it. This is also supported by the fact that the histograms (Figure 6) show a small number of short grooves due to the truncation bias mentioned above. On the

345 other hand, the U_{co} (i.e. the highest plateau breaking point) is defined by the maximum value of the
346 size range and it is easily recognizable by a slope break in all considered grooves systems (Figure 7).
347 The fractal analysis applied on all study areas show a clear plateau in the diagrams (Figure 7),
348 hence providing the identification of the size range where the fractal behaviour is valid. A size interval
349 for both the L_{co} and U_{co} have been outlined through gray bands on Figure 7 and reported in Table 2.
350 Uruk Sulcus reveals a fractal behaviour between 9-11 km and 105-120 km (Figure 7A), Babylon
351 Sulci between 10-13 km and 115-130 km (Figure 7B), Phrygia Sulcus between 10-13 km and 115-
352 130 km (Figure 7C), and Mysia Sulci between 10-13 km and 110-125 km (Figure 7D). As stated
353 above, the values found for L_{co} are not useful due to the noisy data. On the contrary, the values of U_{co}
354 are reliable and comparable for all datasets. The U_{co} is the vertical maximum extension of the
355 connected grooves network (Mazzarini and Isola, 2010, Mazzarini et al., 2013) and, hence, it is
356 directly linked to the mechanical layering of the medium. This analysis reveals that this vertical
357 extension ranges between 105 and 130 km for the four equatorial regions considered. Moreover, this
358 suggests that this limit might be the potential thickness of the icy crust located above the deep ocean
359 and required for the development of densely populated grooves at the surface.

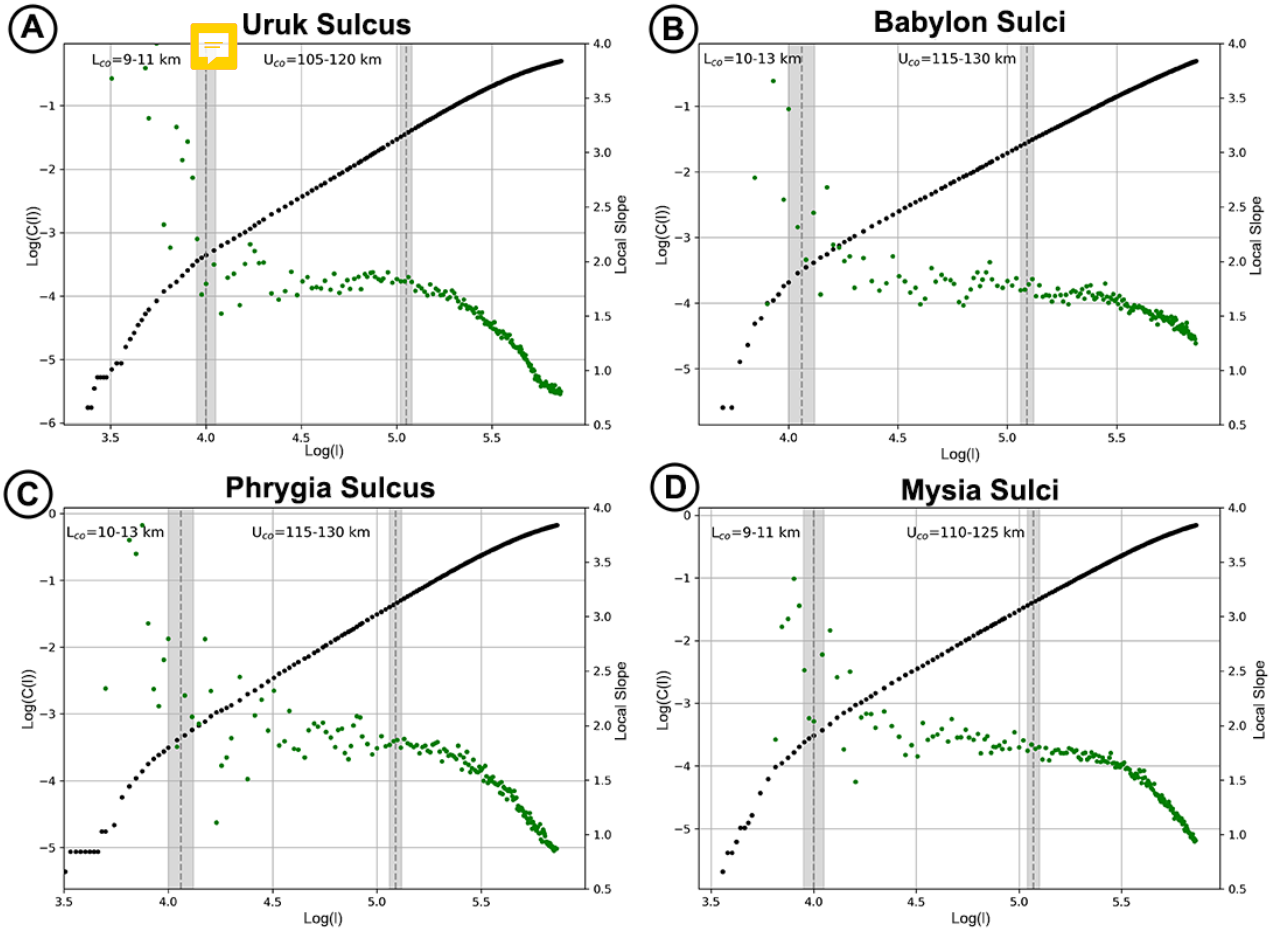

Figure 7: Self-similar clustering analysis for A) Uruk Sulcus, B) Babylon Sulci, C) Phrygia Sulcus and D) Mysia Sulci. For each dataset, it is reported the log plot of *C(l) vs l* (black points) and the *local slope vs Log(l)* plot (green points). The size range of interconnected fractures are represented by the plateau stage of the local slope curve (green points). The gray stripes are the L_{co} and U_{co} intervals that define the size range of the fractal distribution. The slope of the curve (black points) is the fractal exponent *D* computed in the size range L_{co} - U_{co}. The distribution stops to be fractal when the local slope curve (green points) breaks. The breaking point corresponds to a *Log(l)* value (U_{co}) that represents the potential thickness of the icy crust above the deep ocean required for the development of densely populated structures at the surface (i.e. the grooves). U_{co} ranges between 105 km and 130 km, when considering all grooves system analysed.

Dataset	Longitude	Latitude	N	D	R^2	U_{co}(km)
Uruk Sulcus	185°E - 220°E	15°S - 20°N	1068	1.877± 0.03	0.999	105-120
Babylon Sulci	260°E - 320°E	20°S - 15°N	882	1.847 ± 0.03	0.9991	115-130
Phrygia Sulcus	340°E - 15°E	5°N - 30°N	987	1.945 ± 0.01	0.9997	115-130
Mysia Sulci	10°E - 40°E	10°S - 20°N	678	1.95 ± 0.02	0.9991	110-125

Table 2: Parameters of spatial distribution analysis (self-similar clustering) of grooves for each selected area with associated latitude and longitude range. *N* is the number of grooves, *D* the fractal exponent of fractures self-similar clustering, R^2 the goodness of fit and U_{co}, the upper cut-off.

We highlight that few grooves reaching this maximum depth are expected, while a larger number remain confined at much shallower depths, as suggested by the length distribution analysis reported above. Noteworthy, in all four data sets the grooves fractal distribution is characterized by a well-defined single plateau, suggesting that the strain redistribution at the scale of the whole crust occurs by a hierarchical fracture network where few large faults control and distribute the crustal strain. Indeed, the large grooves characterised by the power-law fitting behaviour can be considered as crustal-scale structures, typically with a strike slip component (as shown in Cameron et al., 2018; Rossi et al., 2019) that localizes and accommodates most of the crustal strain. Specifically, these large structures can theoretically reach the crust-ocean interface. On the contrary, the shorter grooves populations (exponentially-fitted) may act as confined structures as response to lower strain.

We expect exponentially-fitted length distribution grooves to be confined within the brittle portion of the crust, in particular when considering crustal rifting modes affecting the opening of the lithosphere in earlier Ganymede history (Pizzi et al., 2019), i.e. when the icy crust was thought to be thinner and most of the grooves' nucleation took place. Moreover, the vertical extent of the second order structures may be controlled by necking instability occurring in Ganymede crust at shallow depth at 10^{-4} s^{-1} strain rate, as suggested by finite element method (FEM) simulations (e.g., Bland and

393 Showman, 2007). However, the progressive thickening of Ganymede crust through time and the
394 possible effects due to tidal stress (Cameron et al., 2019) may have contributed in localizing the strain
395 within few large pre-existing structures, that may have recurrently reactivated, hence cross-cutting
396 the entire crust.
397
398 The spatial distribution analysis shows that only a relatively small number of grooves is able to
399 penetrate the icy crust. Being, most of the longer structures recognized as the boundaries of strike-
400 slip corridors often delimiting the transition between the dark and light terrains, they represent the
401 lead candidates that could have penetrated the entire icy crust. On the other hand, since our data are
402 affected by truncation bias and the analysis has been performed at a regional scale, we cannot infer
403 about the behaviour of shorter grooves nor observe the surface deformation of shorter structures
404 induced by tidal stresses (Cameron et al., 2019).
405
406 The general framework presented above may suggest two possible tectonic scenarios for grooves
407 development: i) syn-kinematic extension and strike-slip activities through time or ii) two distinct
408 evolutionary phases with extension, followed by strike-slip faulting. The occurrence of a single
409 plateau in all datasets could support the first tectonic scenario as the more plausible one. Nevertheless,
410 to fully confirm one scenario over the other, a dedicated structural investigation at higher resolution
411 is needed.
412
413 The interpretation of few long grooves propagating down to the liquid ocean is supported by
414 the values of U_{co} (ranging between 105 and 130 km). Such values agree with independent estimates
415 of Ganymede icy layer thickness. Through the interpretation of Galileo magnetic data, Kivelson et
416 al., (2002) suggested the presence of a conducting layer at a depth of 150 km below the icy crust.
417 Later, Saur et al., (2015) stated the presence of a saline conductive ocean at a depth of 150 km through
418 the observation and modelling of Ganymede's auroral ovals dynamics. On the other hand, Schenk et

al., (2002) provides an estimate of at least 80 km for the icy shell thickness by analysing the transition between depth to diameter ratio of large impact craters.

To summarize, we found that (i) the grooves are the representation of a hierarchical system constituted by second order structures controlled by the rheological layering of the crust (i.e. grooves fitted by exponential length distribution) and few major crustal-scale structures (i.e. grooves fitted by power-law distribution) with possible prevalence of strike-slip kinematics, (ii) the occurrence of a large first order tectonic structures cutting the ~~whole~~ icy crust that (even if limited in number) may control the crustal strain distribution and (iii) the presence of icy solid crust with thickness of 100-130 km along the equatorial belt of Ganymede which is in agreement with previous measurements.

5. Conclusion

In this work we analysed length size-distribution and self-similar clustering of Ganymede's grooves populations to estimate the ~~potential~~ thickness of the icy crust above the deep ocean and potential mechanical layering within the crust. Grooves represent the evidence of tectonic activity that deformed the Ganymede surface during its geologic evolution and characterize the light material unit of the satellite. Specifically, we investigated four regions located on the Ganymede equatorial area by using the regional scale grooves mapping performed by Rossi et al., (2020). The four chosen datasets are selected regions in Uruk Sulcus, Babylon Sulci, Phrygia Sulcus and Mysia Sulci centered at 0.8°N, 200°E, 0°N, 290°E, 15°N, 355°E and 7°N, 20°E and containing 1068, 882, 678 and 987 grooves, respectively. On such datasets, we firstly performed a length distribution analysis to describe the depth propagation and growing evolution of the faults underlying grooves systems. Then, we investigated the grooves spatial distribution (self-similar clustering) in order to infer the vertical extension of the connected fractures network and, hence, evaluate the scaling properties of the system.

We found that the grooves length distribution change from exponential (shorter grooves) to power-law (longer grooves) at a threshold length of 93.8 km, 148 km, 238.7 km, 185 km for Uruk Sulcus, Babylon Sulci, Phrygia Sulcus and Mysia Sulci, respectively.

This means that the shorter, exponentially-fitted populations may act as confined structures, while the large grooves fitted by power-law curves can be considered as crustal-scale structures theoretically reaching the crust-ocean interface. From the self-similar clustering analysis, we estimated the potential thickness of the icy crust ranging between 105 and 130 km for the datasets considered. This value agrees with independent estimates of the thickness of the icy shell (from 80 to 150 km, Schenk et al., (2002); Kivelson et al., 2002; Saur et al., 2015). Hence, our results support the hypothesis of shorter structures vertically confined in different mechanical layers within the icy crust and few very long faults propagating down to the liquid ocean underneath. The latter are likely underlying the longer grooves often associated to strike slip kinematics at the dark/light terrain boundaries, thus representing important targets in the future Ganymede exploration as potential sites of surface-ocean connections.

The structural approach used in our analysis provides new insights into the depth of faults underlying grooves and the mechanical/rheological layering of Ganymede crust. ~~This analysis is however limited to the equatorial band of Ganymede, i.e. where the four regions have been chosen on the basis of the density and spatial distribution of grooves.~~

Once future mission data will be available, this investigation will be largely improved with new measurements and analysis performed at mid and high latitudes. In particular, the upcoming ESA JUICE (Jupiter ICy moons Explorer, Grasset et al., 2013) mission will provide a global coverage of the surface of Ganymede with an average resolution of 100-150 m/px thanks to the JANUS camera (Jovis, Amorum ac Natorum Undique Scrutator, Palumbo et al., 2014). This instrument will provide the possibility to easily detect grooves and related faults and fractures over the full body. Such images,

coupled with digital terrain models will be pivotal to improve the knowledge of the satellite and will provide new insights into the formation and evolution of Ganymede grooves system.

Data availability

Data used in this work are those published by Rossi et al., (2020).

Acknowledgments

The activity has been realized under the ASI-INAF contract 2018-25-HH.0. This manuscript is part of a project that has received funding from the European Union's Horizon 2020 research and innovation programme under grant agreement Nº776276 (PLANMAP). We made use of the ArcGIS 10.5, Matlab and R softwares to perform the presented analysis.

References

Ackermann, R.V., et al., 2001. The geometric and statistical evolution of normal fault systems: An experimental study of the effects of mechanical layer thickness on scaling laws: Journal of Structural Geology, v. 23, p. 1803–1819, doi: 10.1016/S0191-8141(01)00028-1.

Anderson, J. Det al., 2001. Shape, mean radius, gravity field and interior structure of Ganymede. In *Bulletin of the American Astronomical Society* (Vol. 33, p. 1101).

Allison, M.L, Clifford, S. M., 1987. Ice-covered water volcanism on Ganymede. J. Geophys. Res., 92(B8), 7865-7876.

Becker, T. et al., 2001. Final digital global maps of Ganymede, Europa, and Callisto. Lunar Planet. Sci. Conf. XXXII, 2009.

Belton, M. J. S., et al., 1992. The Galileo solid-state imaging experiment. *Space Science Reviews*, *60*(1-4), 413-455.

Belton, M. J. S., et al., 1996. Galileo's first images of Jupiter and the Galilean satellites. Science, 274(5286), 377.

494 Benedicto, A., et al., (2003). Layer thickness and shape of faults. Geophysical Research Letters, 30,
495 20, 2076, doi:10.1029/2003GL018237.
496 Bianchi, R., et al., 1984. Tectonics of the grooved terrain on Ganymede. Lunar and Planetary Science
497 Conference, 15, 54–55.
498 Bland, M. T., Showman, A. P., 2007. The formation of Ganymede's grooved terrain: Numerical
499 modeling of extensional necking instabilities. Icarus, 189(2), 439-456.
500 Bonnet, E., et al., (2001), Scaling of fracture systems in geological media: Reviews of Geophysics,
501 v. 39, p. 347–383, doi: 10.1029/ 1999RG000074.
502 Bour, O., Davy, P., (1999), Clustering and size distribution of fault patterns: Theory and
503 measurements: Geophysical Research Letters, v. 26, p. 2001–2004, doi:10.1029/1999GL900419.
504 Bour, O., et al., (2002), A statistical scaling model for fracture network geometry, with validation on
505 a multiscale mapping of a joint network (Hornelen Basin, Norway): Journal of Geophysical
506 Research, v. 107, p. 2113, doi: 10.1029/2001JB000176.
507 Cameron, M.E., et al., 2018. Morphological mapping of Ganymede: Investigating the role of strike-
508 slip tectonics in the evolution of terrain types. Icarus 315, 92–114.
509 Cameron, M. E., et al., 2019. Tidal stress modeling of Ganymede: Strike-slip tectonism and Coulomb
510 failure. *Icarus*, *319*, 99-120.
511 Carr, M. H., et al., 1995. The Galileo Imaging Team plan for observing the satellites of Jupiter. J.
512 Geophys. Res. Planets, 100(E9), 18935-18955.
513 Casacchia, R., Strom, R. G., 1984. Geologic evolution of Galileo Regio, Ganymede. Lunar Planet.
514 Sci. Conf. XIV, 1028.
515 Clauset, A., et al., 2009. Power-law distributions in empirical data. *SIAM review*, *51*(4), 661-703.
516 Collins, G. C., et al., 1998a. Formation of Ganymede grooved terrain by sequential extensional
517 episodes: Implications of Galileo observations for regional stratigraphy. Icarus, 135(1), 345-359.
518 Collins, G. C., et al., 1998b. The role of extensional instability in creating Ganymede grooved terrain:
519 Insights from Galileo high-resolution stereo imaging. Geophys. Res. Lett. 25, 233-236.

520 Collins, G. C., et al., 2000. A global database of grooves and dark terrain on Ganymede, enabling
521 quantitative assessment of terrain features. Lunar Planet. Sci. Conf. XXXI, 1034.
522 Collins, G. C., 2009. The origin of grooved terrain on Ganymede. European Planetary Science
523 Congress, 4, 516.
524 Collins, G. C., et al., 2013. Global geologic map of Ganymede. US Department of the Interior, US
525 Geological Survey. doi:10.3133/sim3237.
526 Cowie, P. A., et al., 1994. Quantitative fault studies on the East Pacific Rise: A comparison of sonar
527 imaging techniques. *Journal of Geophysical Research: Solid Earth*, *99*(B8), 15205-15218.
528 Croft, S. K., Strom, R. G., 1985. Ganymede's crust: Structural indicators in the Tiamat Sulcus
529 quadrangle. Lunar Planet. Sci. Conf. XVI, 156-157.
530 Davy, P., 1993, On the frequency-length distribution of the San Andreas fault system: Journal of
531 Geophysical Research, v. 98, p. 12,141–12,151, doi:10.1029/93JB00372.
532 Dombard, A. J., McKinnon, W. B., 2001. Formation of grooved terrain on Ganymede: Extensional
533 instability mediated by cold, superplastic creep. Icarus, 154(2), 321-336.
534 Figueredo, P. H., et al., 1999. Fracture patterns on Ganymede and the initiation of tectonic
535 resurfacing. Lunar Planet. Sci. Conf. XXX, 1832.
536 Grasset, O., et al., 2013. JUpiter ICy moons Explorer (JUICE): An ESA mission to orbit Ganymede
537 and to characterise the Jupiter system. *Planetary and Space Science*, *78*, 1-21.
538 Gudmundsson, A., et al., 2010. Effects of internal structure and local stresses on fractyre propagation,
539 deflection and arrest in fault zones. Journal of Structural Geology, 32, 1643-1655.
540 Gudmundsson, A., 2011 Rock Fractures in Geological Processes. Cambridge University Press,
541 Cambridge, UK, pp 594.
542 Gudmundsson, A., Mohajeri, N., 2013. Relations between the scaling exponents, entropies, and
543 energies of fracture networks. Bull. Géol. France, 2013, 184, 4, 377-387.
544 Gudmundsson, A., et al., 2013. Length-displacement scaling and fault growth. Tectonophysics, 608,
545 1298-1309.

546 Head, J. W., et al., 2002. Evidence for Europa-like resurfacing styles on Ganymede. Geophys. Res.
547 Lett. 29, 2151.
548 Hentschel, H. G. E., I. Proccacia, 1983. The infinite number of generalised dimensions of fractals and
549 strange attractors, Physica D: Nonlinear Phenomena, 435-444.
550 Hussmann, H., et al., (2007). Interiors and evolution of icy satellites. In T. Spohn & G. Schubert
551 (Eds.), Treatise on Geophysics. 10 (pp. 509–539).
552 Kivelson, M.G., et al., 1997. The magnetic field and magnetosphere of Ganymede, Geophys. Res.
553 Lett., 24, 2155-2158.
554 Kivelson, M. G., et al., 2002. The permanent and inductive magnetic moments of Ganymede. Icarus,
555 157(2), 507-522.
556 Kuskov, O. L., et al., 2010. Internal Structure of the Icy Satellites of Jupiter. In *Advances in*
557 *Geosciences: Volume 19: Planetary Science (PS)* (pp. 365-376).
558 Lucchitta, B. K., 1980. Grooved terrain on Ganymede. Icarus, 44(2), 481-501.
559 Lucchetti, A., et al., 2017. Brittle ice shell thickness of Enceladus from fracture distribution
560 analysis. *Icarus*, *297*, 252-264.
561 Mandelbrot, B.B., 1982, The Fractal Geometry of Nature: San Francisco, Freeman, 468 p.
562 Mazzarini F., D'Orazio, M., 2003. Spatial distribution of cones and satellite-detected lineaments in
563 the Pali Aike Volcanic Field (southernmost Patagonia): Insights into the tectonic setting of a
564 Neogene rift system: Journal of Volcanology and Geothermal Research, v. 125, p. 291–305, doi:
565 10.1016/S0377-0273(03)00120-3.
566 Mazzarini, F., 2004, Volcanic vent self-similar clustering and crustal thickness in the northern Main
567 Ethiopian Rift: Geophysical Research Letters, v. 31, p. L04604, doi: 10.1029/2003GL018574.
568 Mazzarini, F., Isola, I. 2010. Monogenetic vent self-similar clustering in extending continental crust:
569 Examples from the East African Rift System: Geosphere, v. 6, p. 567–582, doi: 10
570 .1130/GES00569 .1.

571 Mazzarini, F., et al., 2013 Spatial relationship between earthquakes and volcanic vents in the central-
572 northern Main Ethiopian Rift. *Journal of Volcanology and Geothermal Research* 262, 123–133.
573 McKinnon, W. B., Melosh, H. J., 1980. Evolution of planetary lithospheres: Evidence from
574 multiringed structures on Ganymede and Callisto. Icarus, 44(2), 454-471.
575 Mohajeri, N., and Gudmundsson, A., (2012). Entropies and Scaling Exponents of Street and Fracture
576 Networks. Entropy, 14, 800-833.
577 Moore, J. M., et al., 1999. Mass movement and landform degradation on the icy Galilean satellites:
578 Results of the Galileo nominal mission. Icarus, 140(2), 294-312.
579 Murchie, S. L., et al., 1986. Terrain types and local scale stratigraphy of grooved terrain on
580 Ganymede. Lunar Planet. Sci. Conf. Proceedings, 17.
581 Murchie, S. L., et al., 1989. Crater densities and crater ages of different terrain types on Ganymede.
582 Icarus, 81, 271-297.
583 Murchie, S. L., et al., 1990. Tectonic and volcanic evolution of dark terrain and its implications for
584 the internal structure and evolution of Ganymede. Journal of Geophysical Research: Solid Earth,
585 95(B7), 10743–10768. doi:10.1029/JB095iB07p10743
586 Neukum, G., 1997. Bombardment history of the Jovian system. The Three Galileos: The Man, the
587 Spacecraft, the Telescope. Springer, Dordrecht, pp. 201–212.
588 Neukum, G., et al., 1998. Cratering chronology in the Jovian system and derivation of absolute ages.
589 Lunar Planet. Sci. Conf. XX IX, 1742.
590 Ouillon, G., et al., 1996. Hierarchical geometry of faulting: Journal of Geophysical Research, v. 101,
591 p. 5477–5487, doi:10.1029/95JB02242.
592 Pacheco, J.F., et al., 1992. Change in the frequency-size relationship from small to large earthquakes:
593 Nature, v. 355, p. 71–73, doi:10.1038/355071a0.
594 Palumbo, P., et al., 2014. JANUS: the visible camera onboard the ESA JUICE mission to the Jovian
595 system. In *EGU General Assembly Conference Abstracts* (Vol. 16).

596 Pappalardo, R. T., Greeley, R., 1995. A review of the origins of subparallel ridges and troughs:
597 Generalized morphological predictions from terrestrial models. J. Geophys. Res.: Planets,
598 100(E9), 18985-19007.
599 Pappalardo, R. T., et al., 1998. Grooved terrain on Ganymede: First results from Galileo high-
600 resolution imaging, Icarus, 135, 276-302.
601 Pappalardo, R. T., et al., 2004. Geology of Ganymede. Jupiter: Planet, Satellites, and Magnetosphere,
602 363-396.
603 Patterson, G. W., et al., 2010. Global geological mapping of Ganymede. Icarus, 207(2), 845- 867.
604 Pozzobon, R., et al., 2015. Self-similar clustering distribution of structural features on Ascraeus Mons
605 (Mars): implications for magma chamber depth. *Geological Society, London, Special*
606 *Publications*, *401*(1), 203-218.
607 Prockter, L. M., et al., 1998. Dark terrain on Ganymede: Geological mapping and interpretation of
608 Galileo Regio at high resolution. Icarus, 135(1), 317-344.
609 Prockter, L. M., et al., 2000. Geology and mapping of dark terrain on Ganymede and implications for
610 grooved terrain formation. J. Geophys. Res.: Planets, 105(E9), 22519-22540.
611 Prockter, L. M., et al., 2000. Strike-slip duplexing on Jupiter's icy moon Europa. J. Geophys. Res.,
612 105, 9483-9488.
613 Rossi, C., et al., (2018). Evidence of transpressional tectonics on the Uruk Sulcus region,
614 Ganymede. *Tectonophysics*, *749*, 72-87.
615 Rossi, C., et al., (2020). Structural geology of Ganymede regional groove systems (60° N–60°
616 S). *Journal of Maps*, 1-11.
617 Russell, C. T. (Ed.), 2012. *The Galileo Mission*. Springer Science & Business Media.
618 Saur, J., et al., 2015. The search for a subsurface ocean in Ganymede with Hubble Space Telescope
619 observations of its auroral ovals. Journal of Geophysical Research: Space Physics, 120(3), 1715-
620 1737.

621 Schenk, P., McKinnon, W. B., 1987. Ring geometry on Ganymede and Callisto. Icarus, 72(1), 209–
622 234. doi:10. 1016/0019-1035(87)90126-6-
623 Schenk, P. et al., 2001. Flooding of Ganymede's bright terrains by low-viscosity water-ice lavas.
624 Nature, 410(6824), 57-60.
625 Schenk, P. M., 2002. Thickness constraints on the icy shells of the Galilean satellites from a
626 comparison of crater shapes. Nature 417, 419-421.
627 Schenk, P. M., et al., 2004. Ages and interiors: The cratering record of the Galilean satellites. Jupiter:
628 The planet, satellites and magnetosphere, 427-456.
629 Schultz, R.A., et al., 2010. Fault populationsons. In: *Planetary Tectonics*, edited by Thomas R.
630 Watters and Richard A. Schultz. Cambridge University Press, Cambridge, 457-510.
631 Shoemaker, E. M., et al., 1982. The geology of Ganymede. In Satellites of Jupiter, 1, 435-520.
632 Showman, A.P., et al., 2004. On the resurfacing of Ganymede by liquid water volcanism. Icarus 172,
633 625–640. doi: 10.1016/j.icarus.2004.07.011.
634 Smith, B.A., et al., 1979a, The Jupiter system through the eyes of Voyager 1, Science, 204.
635 Smith, B. A., et al., 1979b. The Galilean satellites and Jupiter: Voyager 2 imaging science results.
636 Science, 206(4421), 927-950.
637 Sohl, F., et al., 2002. Implications from Galileo observations on the interior structure and chemistry
638 of the Galilean satellites. *Icarus*, *157*(1), 104-119.
639 Soliva, R., et al., 2006. Spacing and linkage of confined normal faults: importance of mechanical
640 thickness. *Journal of Geophysical Research: Solid Earth*, *111*(B1).
641 Soliva, R., Schultz, R.A., 2008. Distributed and localized faulting in extensional settings: Insight
642 from the North Ethiopian Rift–Afar transition area. Tectonics, 27, TC2003,
643 doi:10.1029/2007TC002148.
644 Walsh, J.J., Watterson, J., 1993. Fractal analysis of fracture pattern using the standard box-counting
645 technique: Valid and invalid methodologies: Journal of Structural Geology, v. 15, p. 1509–1512,
646 doi: 10.1016/0191- 8141(93)90010-8.

647 Zahnle, K., et al., 2003. Cratering rates in the outer Solar System. Icarus, 163(2). 263–289.
648 doi:10.1016/S0019-1035(03)00048-4.

Supplementary Material

Equatorial grooves distribution on Ganymede: length and self-similar clustering analysis

A.Lucchetti[1], C. Rossi[2], F. Mazzarini[3], M. Pajola[1], R. Pozzobon[4], M. Massironi[4], G. Cremonese[1]

[1]INAF-Astronomical Observatory of Padova, Padova, Italy (alice.lucchetti@inaf.it); [2]INFN - Laboratori Nazionali di Frascati, Frascati (Roma), Italy; [3]INGV- National Institute of Geophysics and Volcanology, Pisa, Italy; [4] Geoscience Department, University of Padova, Padova, Italy.

Length distribution analysis

The length distribution analysis presented in the paper reveals both an exponential and a power-law distribution. The number of samples fitted by a power-law is not as numerous as the ones characterized by the exponential fitting, hence, we applied the Clauset et al., (2009) procedure to validate the existence of the power law fitting model. Indeed, it is well known that even if the data follow a power-law distribution, it does not imply that the power law necessarily provides the best model or fit for the data (Clauset et al., 2009; Mohajeri and Gudmundsson, 2012). A log-log plot that yields a straight line is regarded as an indication that the data follow a power-law size distribution. For a standard least-squares linear regression the goodness-of-fit between the calculated line and the actual data is obtained by considering the residuals of the curve-fitting procedure, that is, the vertical distances of all the points from the regression line. If the fit is good, the residuals should ideally have a mean of zero. Even if our datasets satisfy such condition, this approach does not ensure that the power law necessarily provides the best model or fit for the data. For this reason, we adopted the Clauset et al., (2009) procedure to verify the existence of the power-law for the length distribution analyses of the datasets.

Firstly, for each dataset, we estimated the two power law distribution parameters of *alpha* and x_{min}, where *alpha* is the scaling parameter and x_{min} the threshold value above which the power-law exists. The estimation of x_{min} is done through the Kolmogorov-Smirnoff (KS) statistic and allows to find the x_{min} value that minimizes the value of the KS statistic. After that, the scaling parameter *alpha* is determined through the maximum likelihood estimator (MLE). To test how well our power law distribution fits our observed data, Clauset et al., (2009) suggested to use a goodness of fit via a bootstrapping procedure. Hence, we performed the KS test to verify if the data generated from the power law distribution (with our chosen *alpha* and x_{min}), and the observed data come from the same distribution. Following the Clauset et al., (2009) procedure, we generated a large number of synthetic datasets from power law random generator with our chosen parameters and perform 1000 KS tests to verify if generated and observed data come from the same distribution. This methodology provides a *p-value* that can be used to quantify the plausibility of the hypothesis. Considering the significance level of 0.10, if the *p-value* is greater than 0.1, we conclude that any difference between the empirical data and the model can be explained with statistical fluctuations, while if the *p-value* is less than 0.1, we conclude that the data sets do not come from a power law distribution. In all our datasets we determine that the power law distribution with the chosen parameters is a good fit to the data (*p-value* is greater than 0.45).

For each dataset, we report a Figure containing: (i) a plot of the length cumulative distribution with the associated power-law fitting curve and the parameters for each distribution (*alpha*, x_{min} and *p-value*) and (iii) plots showing the uncertainty on *alpha* and x_{min} parameters.

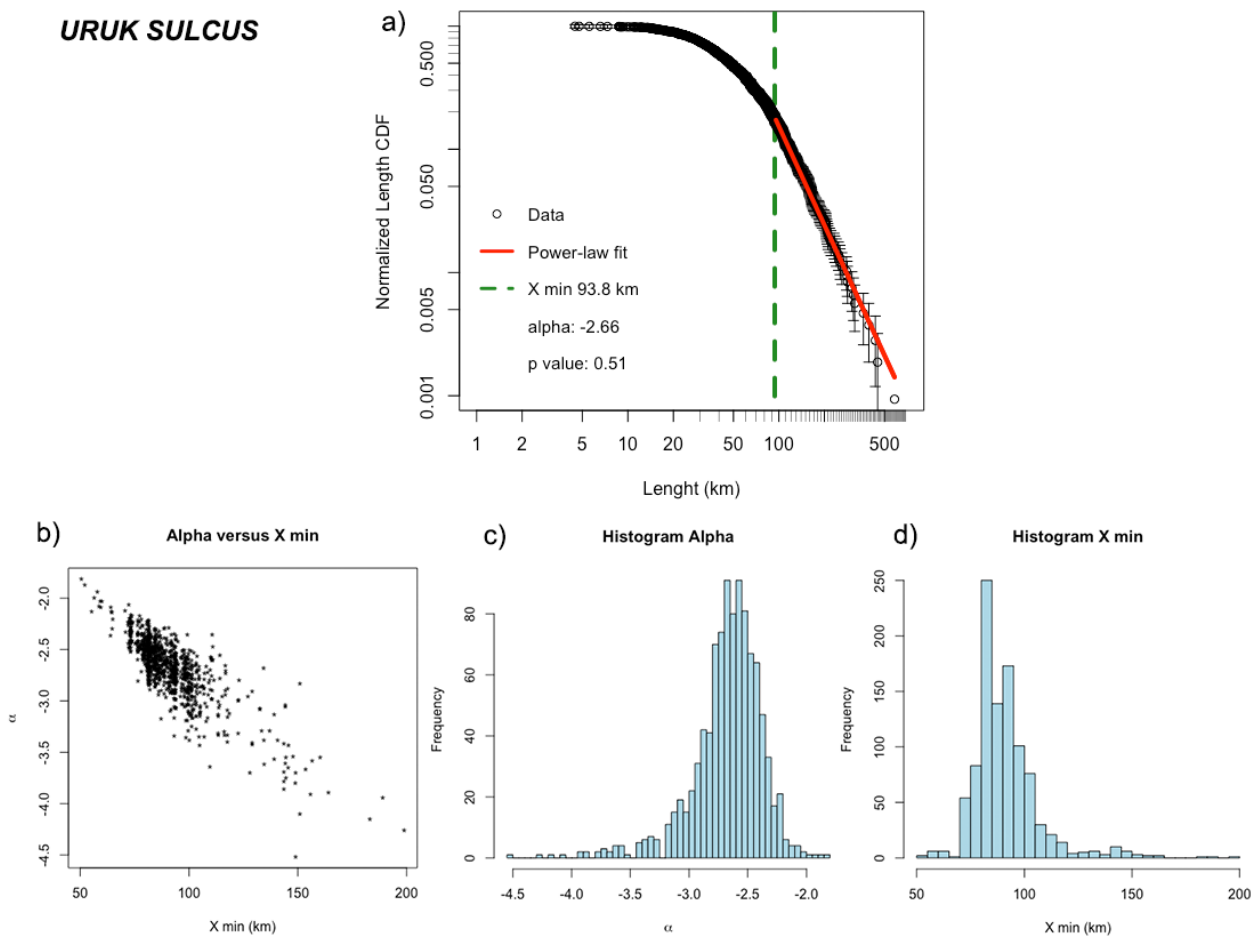

Figure S1: Results of Clauset et al., (2009) procedure on Uruk Sulcus dataset. a) Normalized cumulative distribution plot of the grooves' length with line of best fit (in red). Characterizing uncertainty in parameter values using 1000 thousand bootstraps: b) histogram of x_{min}, c) histogram of *alpha* and d) Scatter-plot of the x_{min} against *alpha*.

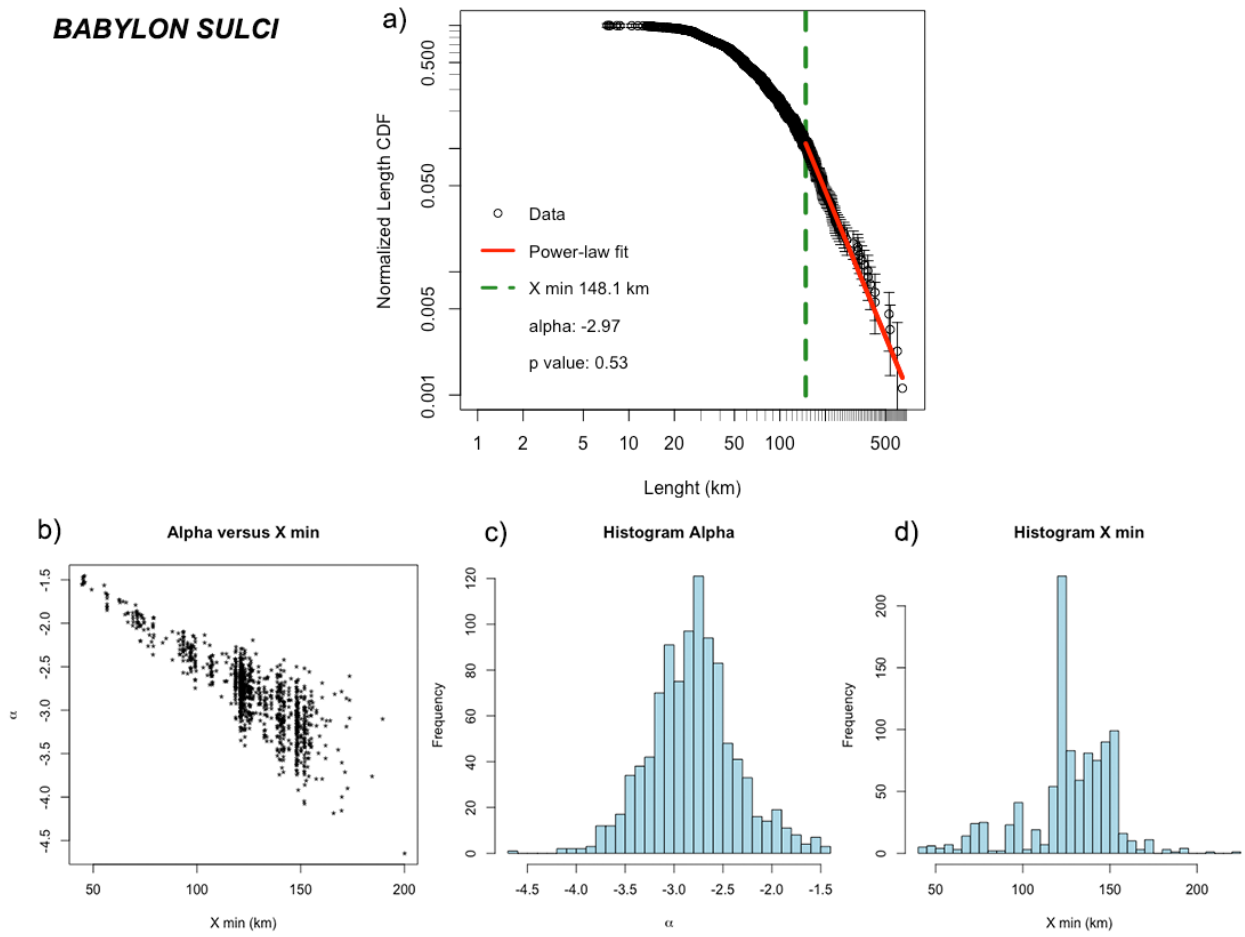

54

55 **Figure S2:** Results of Clauset et al., (2009) procedure on Babylon Sulci dataset. a) Normalized
56 cumulative distribution plot of the grooves' length with line of best fit (in red). Characterizing
57 uncertainty in parameter values using 1000 thousand bootstraps: b) histogram of x_{min}, c) histogram of
58 *alpha* and d) Scatter-plot of the x_{min} against *alpha*.

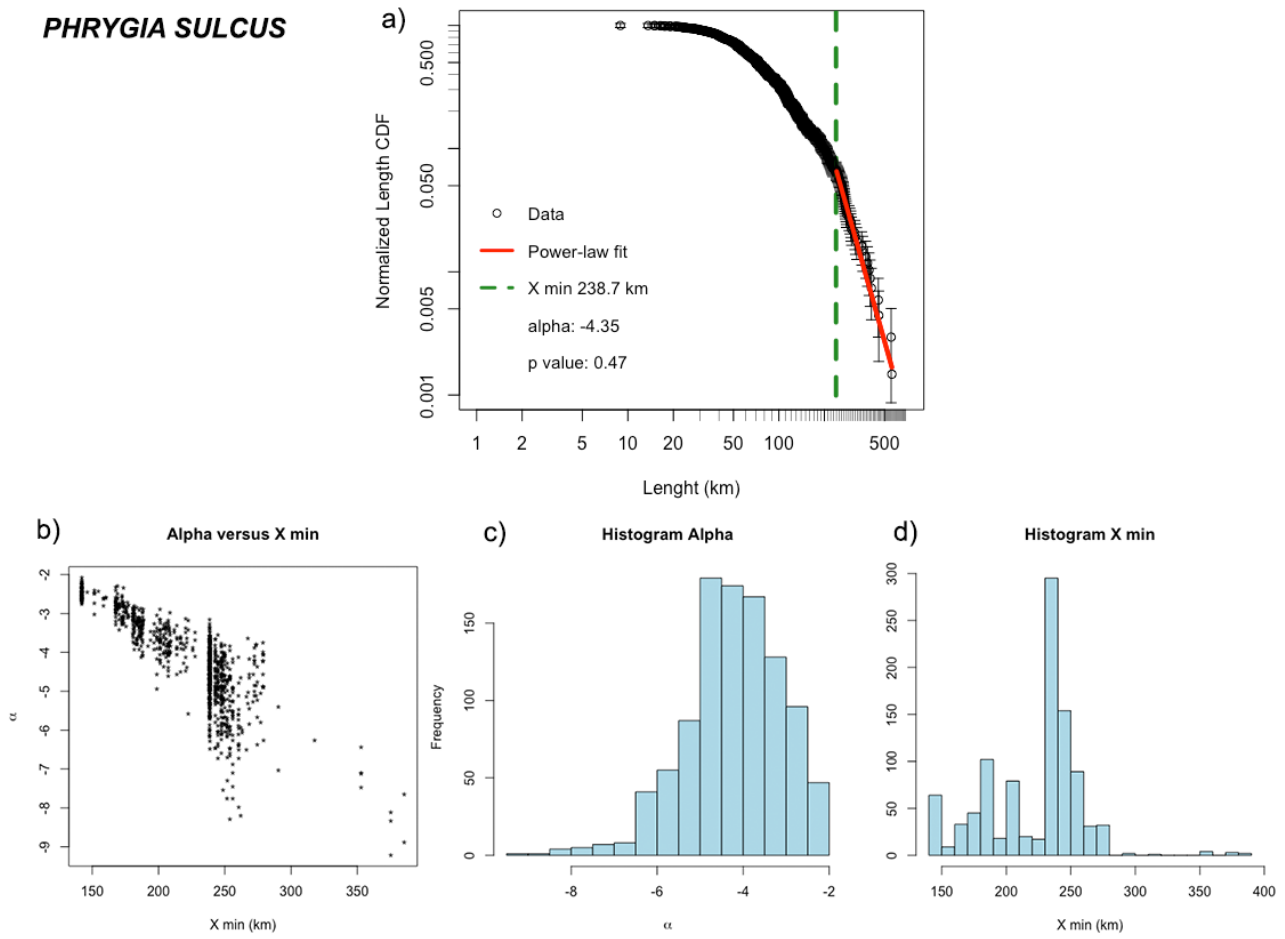

Figure S3: Results of Clauset et al., (2009) procedure on Phrygia Sulcus dataset. a) Normalized cumulative distribution plot of the grooves' length with line of best fit (in red). Characterizing uncertainty in parameter values using 1000 thousand bootstraps: b) histogram of x_{min}, c) histogram of *alpha* and d) Scatter-plot of the x_{min} against *alpha*.

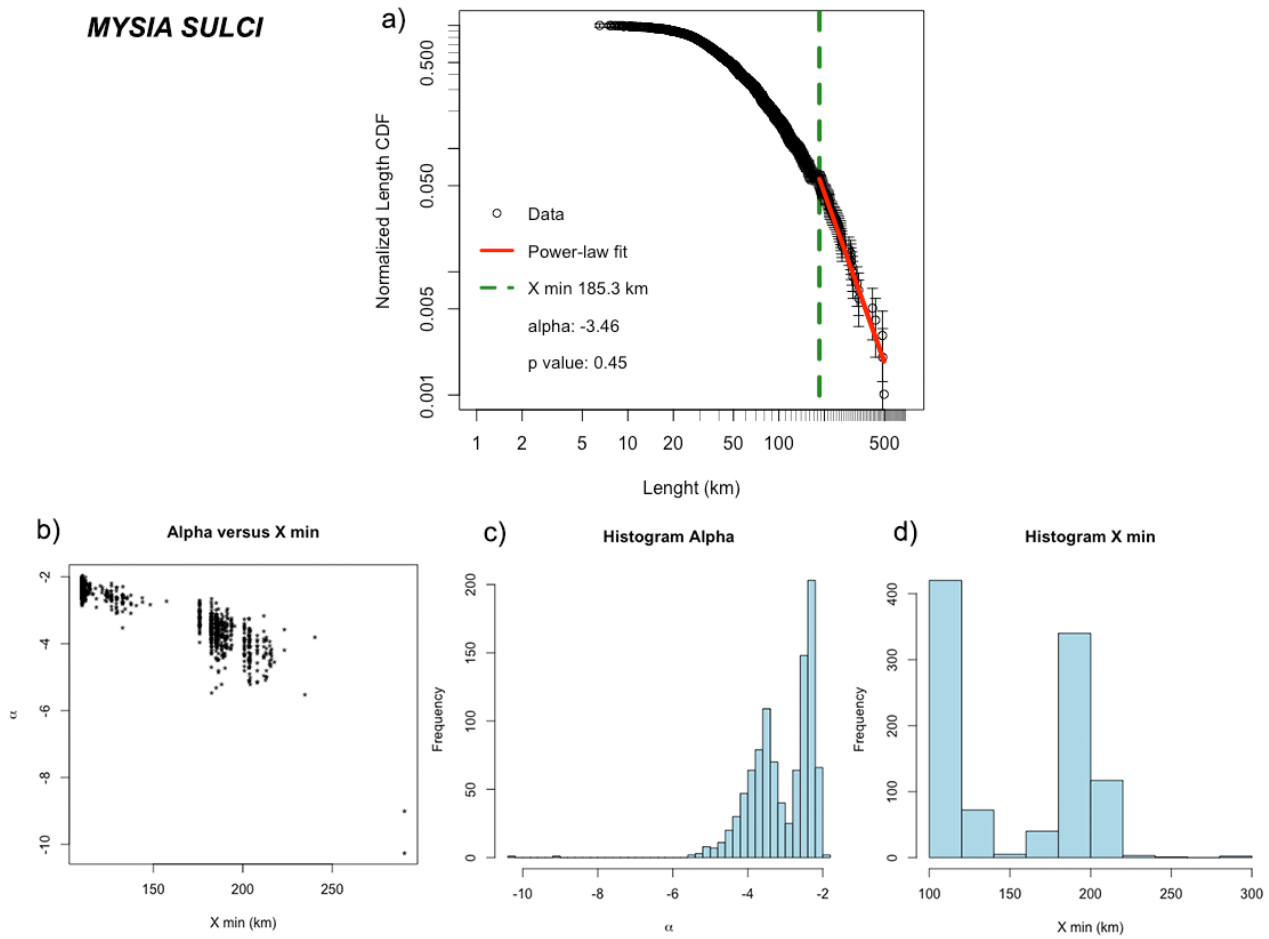

Figure S4: Results of Clauset et al., (2009) procedure on Mysia Sulci dataset. a) Normalized cumulative distribution plot of the grooves' length with line of best fit (in red). Characterizing uncertainty in parameter values using 1000 thousand bootstraps: b) histogram of x_{min}, c) histogram of *alpha* and d) Scatter-plot of the x_{min} against *alpha*.

References

Clauset, A., et al., 2009. Power-law distributions in empirical data. *SIAM review*, *51*(4), 661-703.

Mohajeri, N., and Gudmundsson, A., (2012). Entropies and Scaling Exponents of Street and Fracture Networks. Entropy, 14, 800-833.

Highlights

- Ganymede’s grooves are the representation of a hierarchical system
- Shorter grooves are vertically confined in the brittle icy crust
- Longer grooves are crustal-scale structures theoretically reaching the crust-ocean interface
- The icy shell thickness interested by grooves penetration is between 105 and 130 km

Equatorial grooves distribution on Ganymede: length and self-similar clustering analysis

A. Lucchetti[1], C. Rossi[2], F. Mazzarini[3], M. Pajola[1], R. Pozzobon[4], M. Massironi[4], G. Cremonese[1]

[1]INAF-Astronomical Observatory of Padova, Padova, Italy (alice.lucchetti@inaf.it); [2]INFN - Laboratori Nazionali di Frascati, Frascati (Roma), Italy; [3]INGV- National Institute of Geophysics and Volcanology, Pisa, Italy; [4] Geoscience Department, University of Padova, Padova, Italy.

Abstract

Grooves represent the evidence of tectonic activity that deformed Ganymede surface during its geologic evolution. In this work, we investigate the main characteristics of Ganymede's grooves populations on four different areas located at the equatorial region of the satellite (Uruk Sulcus, Babylon Sulci, Phrygia Sulcus and Mysia Sulci). Specifically, we analyse i) the grooves length distribution to provide a framework for their evolution and ii) the grooves self-similar clustering to infer their vertical penetration inside Ganymede icy shell. For each dataset, we find that the grooves distribution is well fitted by an exponential-law and a power-law distribution depending on the structure length. This implies the presence of confined structures in a shallow layer of the icy crust (relatively shorter, exponentially-fitted structures) and crustal-scale structures that could theoretically reach the crust-ocean interface (relatively longer, power law-fitted structures). In addition, the existence of two exponential distributions for few datasets suggest that there could be two differently systems of structure confined within specific mechanical crust layers.

The thickness of the penetrated icy shell is retrieved through the self-similar clustering analysis and ranges between 105 and 130 km for the examined datasets. This value agrees with independent estimates of the icy shell thickness, ranging between 80 and 150 km. Moreover, our results support the hypothesis that a large number of grooves penetrate the brittle icy crust, with sets of fractures

vertically confined in different mechanical layers, while the penetration of few interconnected faults underlying longer grooves may interest the whole icy crust above the liquid ocean.

1. Introduction

Ganymede is the largest of the four Jupiter's satellites with a diameter ~5262 km (Anderson et al., 2001). Its unique characteristics were first investigated by two flybys of Voyager 1 and 2 in 1979 (Smith et al., 1979a, 1979b) and subsequently, by the remote sensing instruments onboard Galileo between 1995 and 2003 (Russell et al., 2012). Ganymede was found to be the only solid body in the outer Solar System that owns an internal dynamo field (Kivelson et al., 1997). Moreover, it was discovered that Ganymede hosts a subsurface ocean (Kivelson et al., 2002). The thickness of the differentiated layers of the satellite's interior is still under investigation, even if the outer icy crust above the liquid ocean has been suggested to be 120-170 km thick (Kivelson et al., 2002; Sohl et al., 2002; Hussmann et al., 2007; Kuskov, 2010; Saur et al., 2015). The implication coming from the presence of an ocean are important for the evolution of the satellite, the tectonic activity shaping its surface and the stress mechanisms acting on it.

The uniqueness of this satellite was also revealed by its surface features. Indeed, Ganymede's surface is subdivided into two geological domains distinguishable by albedo, morphology and crater density: dark and light terrains (Smith et al., 1979a, 1979b; Shoemaker et al. 1982; Pappalardo et al., 2004; Patterson et al., 2010; Collins et al., 2013, Hargitai & Kereszturi, 2015). The heavily cratered dark terrain covers 35% of the surface of the satellite (Shoemaker et al., 1982; Murchie et al., 1986, 1989; Neukum, 1997; Neukum et al., 1998; Prockter et al., 1998; Zahnle et al., 2003; Schenk et al., 2004) and it is characterized by large-scale, arcuate fracture systems termed furrows, that have been hypothesized to be the remnants of former multiring basins (McKinnon & Melosh, 1980; Murchie et al., 1990; Prockter et al., 1998; Schenk & McKinnon, 1987, Hirata et al., 2020). A thin low albedo deposit overlying the bright icy material may be responsible for the darkness of the terrain (Casacchia and Strom, 1984; Croft and Strom, 1985, Allison and Clifford, 1987; Figueredo et al., 1999; Moore

et al., 1999; Prockter et al., 2000), that is estimated to be > 4 Gyr old (Zahnle et al., 2003). The remaining 65% of the surface is covered by bright terrains which are less densely cratered, younger, heavily tectonized and mainly constituted by longitudinal swaths termed "Sulci" and polygons several tens of kilometers across (Lucchitta, 1980; Patterson et al., 2010). The light terrain may have been emplaced between 2 Gyr or even up to 4 Gyr ago, depending on the cratering model chronology used (Zahnle et al., 2003), and it is characterized by the presence of linear features called grooves (Murchie et al., 1986; Pappalardo et al., 1998; Prockter et al., 2000; Collins, 2009). Grooves are regional-scale morphotectonic structures, from linear to curvilinear, that represent the manifestation of brittle deformation of the light terrain (i.e. fractures and faults) (Lucchitta, 1980; Bianchi et al., 1986; Pappalardo & Greeley, 1995; Pappalardo et al., 1998, 2004). The proposed tectonic processes responsible for the groove formation include extension, e.g. horst-and-graben normal faulting pulling the terrain apart (Shoemaker et al., 1982; Belton et al., 1996, Pappalardo et al., 1998; Dombard and McKinnon, 2001; Bland and Showman, 2007), and strike-slip kinematics (e.g. Pappalardo et al., 1998, Cameron et al., 2018). In addition to these processes, local resurfacing by tectonism (Head et al., 2002) and cryovolcanic flows (Schenk and McKinnon., 2001; Showman et al., 2004) may contribute to the actual groove morphology.

Grooves represent the evidence of tectonic activity that deformed the satellite surface during its geologic evolution and may have played a key role in the possible connection between surface and the subsurface ocean (Head et al., 2002). In this context, the analysis of Ganymede deformed surface could provide hints regarding its interior, as well as its ice shell's mechanical behaviour. Hereafter, since grooves are the surface expression of brittle deformation, we refer to them as faults. Indeed, faults distribution and fault populations on icy satellites can reveal insights into the evolution of their surface that cannot be gained with other techniques. In particular, statistical characterization of fault-population attributes, such as length and spatial clustering, are fundamental means to explore deformation rates, stress transmission modes, rheology of the medium, and mechanical layering (Benedicto et al. 2003; Soliva and Schultz, 2008; Gudmundsson et al. 2010, Gudmundsson et al.,

2011; Schultz et al. 2010; Gudmundsson et al. 2013). The fractal analysis has been used in terrestrial planets studies to infer the thickness of the fractured crust (e.g., Mazzarini and D' Orazio, 2003; Mazzarini, 2004; Soliva and Schultz, 2008; Mazzarini and Isola, 2010; Pozzobon et al. 2015). In the same fashion, on icy satellites the exploration of the depth at which fractures penetrate the icy layer could be constrained investigating the main characteristics of fault populations, such as length size-distribution and clustering (Lucchetti et al., 2017).

In this work, we analyse the the faults' length (i.e. the grooves' length) and spatial distribution (Bonnet et al., 2001; Bour et al., 1999; Bour et al., 2002 ; Gudmundsson et al., 2013) to estimate the potential thickness of the icy crust above the deep ocean required to develop densely populated structures at the surface of Ganymede (i.e. the grooves). After analysing the global faults distribution, we investigate the behaviour of four regions located on the equatorial area of the satellite. Then, we analyse the faults length distribution and self-similar spatial clustering providing the vertical extension of faults penetration inside Ganymede icy shell.

2. Dataset

Ganymede imagery coverage comes from the data acquired by both the Wide Angle Camera (WAC) and Narrow Angle Camera (NAC) onboard Voyager 1 and 2 and the Solid State Imaging (SSI, Belton et al., 1992) camera onboard Galileo spacecraft. Specifically, the subjovian hemisphere was imaged by Voyager 1 with a resolution up to 1 km/px, while the antijovian hemisphere was imaged by Voyager 2 with a resolution up to 500 m/px. The leading and trailing hemisphere were imaged with a resolution of 2 km/px and 3.6 km/px respectively by distant encounters of Ganymede during the Galileo Jupiter tour to fill the Voyager coverage gaps (Carr et al., 1995). In addition, the six Galileo close encounters with Ganymede allowed the acquisition of high-resolution images (100 m/px and higher) by the SSI camera. Based on these remote sensing data, the United States Geological Survey (USGS) Astrogeology Science Centre assembled a global image mosaic of the surface resampled at 1 km/px (Becker et al., 2001, Figure 1). The map was derived combining reasonable input resolution

images (from 20 km/px for gap fill to approximately 400 m/px) and works for the global mapping of grooves.

Ganymede grooves (faults) are located on four different types of light material units (Collins et al., 2013): light irregular material, light subdued material, light grooved material and undivided light material (Figure 1). The light irregular material exhibits a mixture of both smooth and grooved surfaces with a relatively high to moderate albedo and it is characterized by grooves with irregular orientation and spacing (Collins et al., 2013). The light subdued material is thought to be representative of the early stage grooved terrain formation, hence displaying smooth surface and faint lineaments with similar spacing and orientations (Collins et al., 2013). The light grooved material likely formed through the modification and deformation of pre-existing materials, such as the light subdued material or dark terrain and it is mainly characterized by similarly spaced and oriented areas of closely packed troughs and lineaments. Finally, the light undivided material is identified when the other three terrains cannot be discerned (Collins et al., 2013). Three different relative age domains have been identified for each light terrain, except for the undivided light terrain (Patterson et al., 2010; Collins et al., 2013).

Grooved terrains represent the deformation of Ganymede's light terrains: they exhibit two superposed scales of grooves with different structure, spacing and length (Patterson et al., 2010). The local scale allows the identification of structures spacing < 5 km and length < 50 km, while grooves identified at the regional scale are usually clustered in sets of grooves with length > 100 km and average spacing of about 10 km, often displaying parallel ordered patterns (Bianchi et al., 1984; Casacchia & Strom, 1984; Collins et al., 2000, 2013; Lucchitta, 1980; Pappalardo et al., 1998, 2004; Pappalardo & Greeley, 1995; Patterson et al., 2010).

Our analysis is based on the regional scale grooves mapping (Rossi et al., 2020) that represents a useful dataset to improve the knowledge of the tectonic evolution of the satellite and to recognize the main characteristics of these features (Figure 1). In particular, grooves on Ganymede were manually mapped on the global image mosaic (Becker et al., 2001) between 60°N and 60°S and

digitized in a geographic information system (GIS) geodatabase (Rossi et al., 2020). Due to the limitation of illumination and resolution conditions of the Ganymede mosaic, grooves were mapped on approximately 36% of the light terrain. As reported in Rossi et al., (2020), mapped grooves are considered as the topographic expression of trough structures recognizing their bottom thanks to the luminosity contrast resulting from the solar lighting conditions.

Thanks to these comprehensive grooves mapping dataset, we were able to select four different type-regions located on the equatorial belt of Ganymede. The choice is based on the high density and homogeneous spatial distribution of the grooves located on those regions, which is necessary for the following analysis. The four datasets are located in selected regions in Uruk Sulcus, Babylon Sulci, Phrygia Sulcus and Mysia Sulci, respectively (Figure 2-5). Uruk Sulcus is centered at 0.8°N, 200°E, and exhibits different intersecting bands of light units characterized by various tectonism mechanisms, such as normal faulting, graben, domino-style faulting (Pappalardo et al., 1998; Cameron et al., 2018) and transpressional strike-slip faulting (Rossi et al., 2018). The number of grooves of the selected area is 1068 (Figure 2). The area selected in Babylon Sulci is centered at 0°N, 290°E, as shown in Figure 3, and it includes 882 grooves. Babylon Sulci has been inferred as an example of strike-slip setting, where grooves super-system delineates longer and sub-parallel grooves that enclose shorter grooves with different directions (Rossi et al., 2020). A similar regional setting is found in Phrygia Sulcus. Here, the study area was centered at 15°N, 355°E and includes 678 grooves (Figure 4). Finally, the fourth dataset is located in Mysia Sulci and centered at 7°N, 20°E and it is constituted by 987 grooves (Figure 5).

Figure 1: A-B) Orthographic projection of the global image mosaic of Ganymede centered at 0°N, 0°E and at 0°N, 180°E, respectively (available at https://astrogeology.usgs.gov). C-D) The orthographic projection of the Collins et al. (2013) published global geological map of Ganymede. The legend refers to the light terrain units where grooves were mapped: light subdued unit (*ls1, ls2, ls3*), light irregular unit (*li1, li2, li3*), light grooved unit (*lg1, lg2, lg3*) and light undivided unit (*l*) (Collins et al., 2013). E-F) The orthographic projection of the mapped grooves performed on Ganymede image mosaic by Rossi et al., (2020). The total number of identified groove structures (in orange) is 14,707 between 60°N and 60°S region. All maps report the Sulci names of the selected regions used in our analysis.

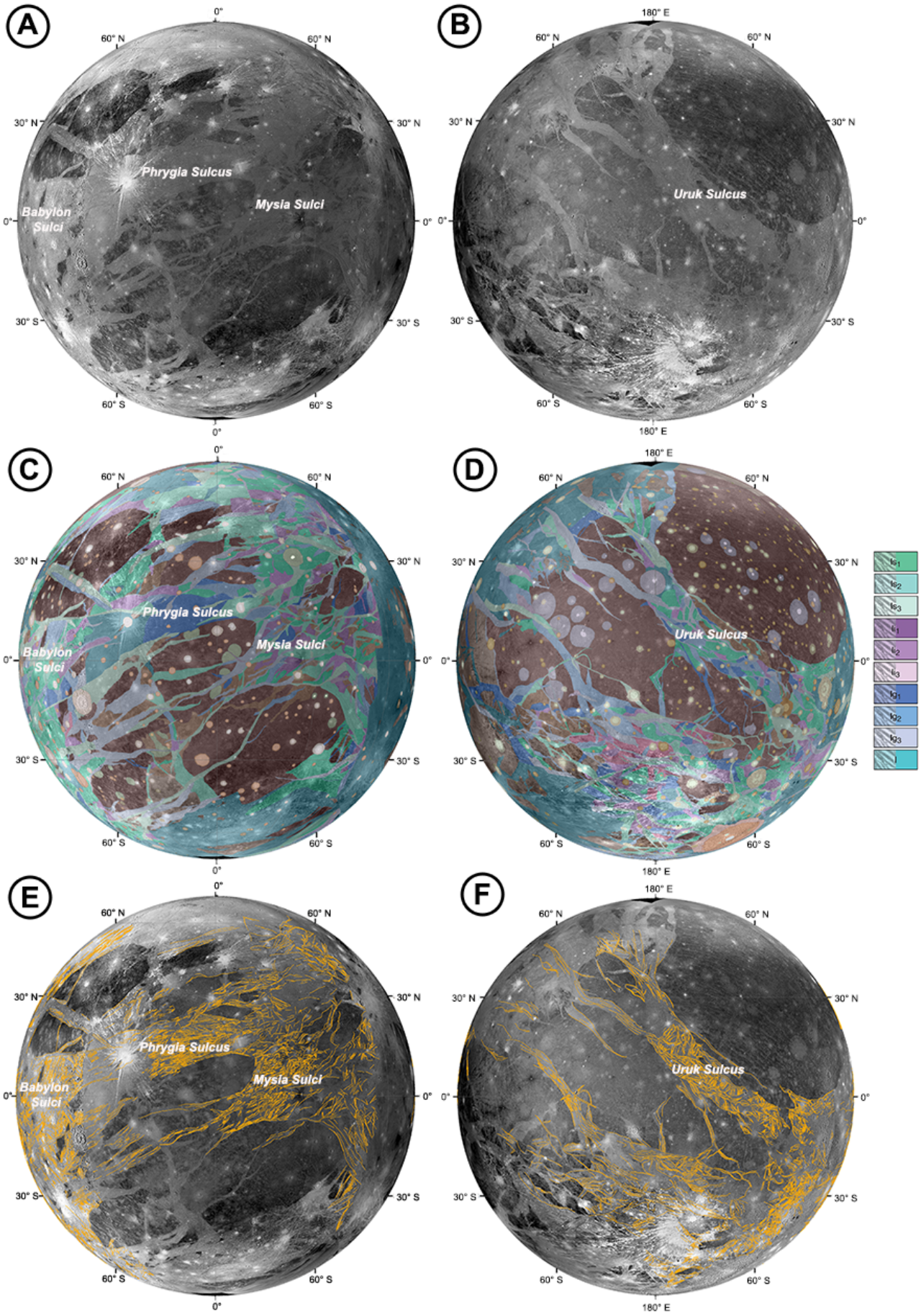
A
B
C
D
E
F
Phrygia Sulcus
Mysia Sulci
Babylon Sulci
Uruk Sulcus
0°
60° N
30° N
30° S
60° S
180° E

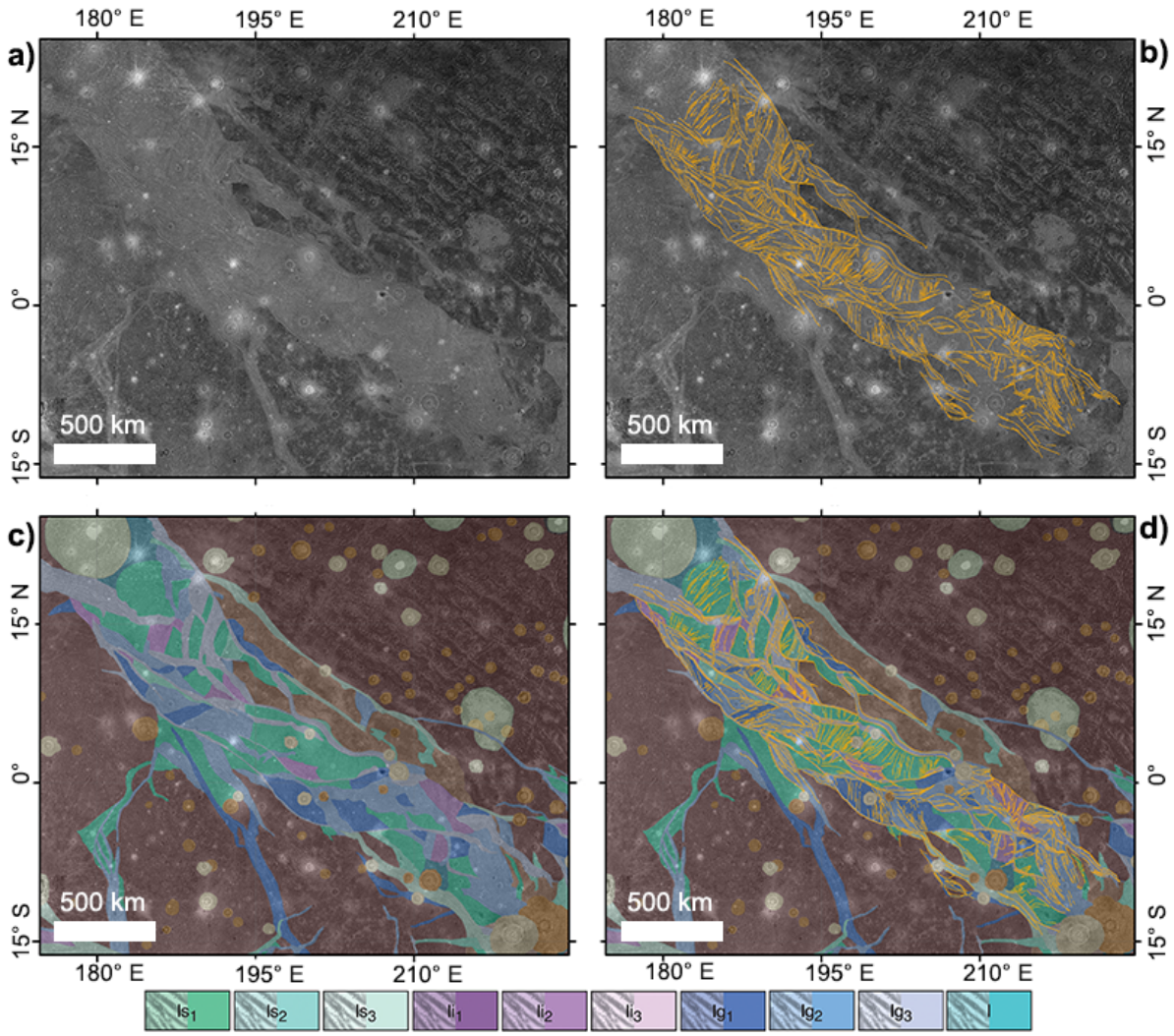

165

166 **Figure 2:** Grooves selected in Uruk Sulcus area in the region centered at 0.8°N, 200°E. A) Ganymede
167 base map (Ganymede Voyager - Galileo SSI Global Mosaic Ganymede, available at
168 https://astrogeology.usgs.gov) representing the area of Uruk Sulcus under study. B) The number of
169 grooves mapped (Rossi et al., 2020) and selected for the analysis is 1068. C) The geological map of
170 Collins et al., (2013) overlaid in transparency on the base map. D) The grooves mapped are overlaid
171 on the geological map. The legend represents the geological units corresponding to the light terrain
172 on which grooves were mapped (light subdued unit: *ls1, ls2, ls3*, light irregular unit: *li1, li2, li3*, light
173 grooved unit: *lg1, lg2, lg3* and light undivided unit *l*). For nomenclature and interpretation of the
174 geological units, we refer the reader to Collins et al., (2013).

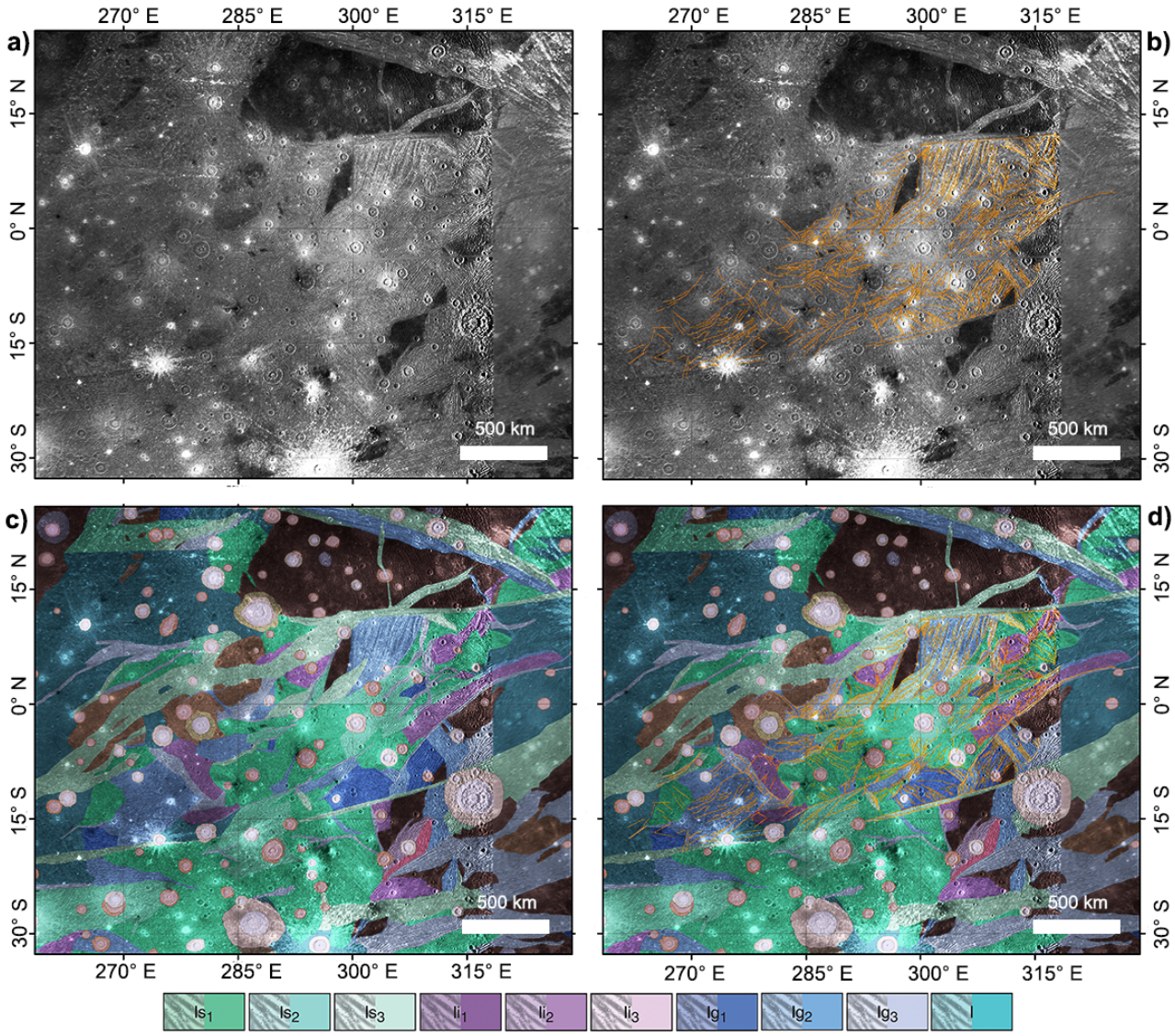

Figure 3: Grooves selected in Babylon Sulci area in the region centered at 0°N, 290°E. A) Ganymede base map (Ganymede Voyager - Galileo SSI Global Mosaic Ganymede, available at https://astrogeology.usgs.gov) representing the area of Babylon Sulci under study. B) The number of grooves mapped (Rossi et al., 2020) and selected for the analysis is 882. C) The geological map of Collins et al., (2013) overlaid in transparency on the base map. D) The grooves mapped are overlaid on the geological map. The legend represents the geological units corresponding to the light terrain on which grooves were mapped (light subdued unit: *ls1, ls2, ls3*, light irregular unit: *li1, li2, li3*, light grooved unit: *lg1, lg2, lg3* and light undivided unit *l*). For nomenclature and interpretation of the geological units, we refer the reader to Collins et al., (2013).

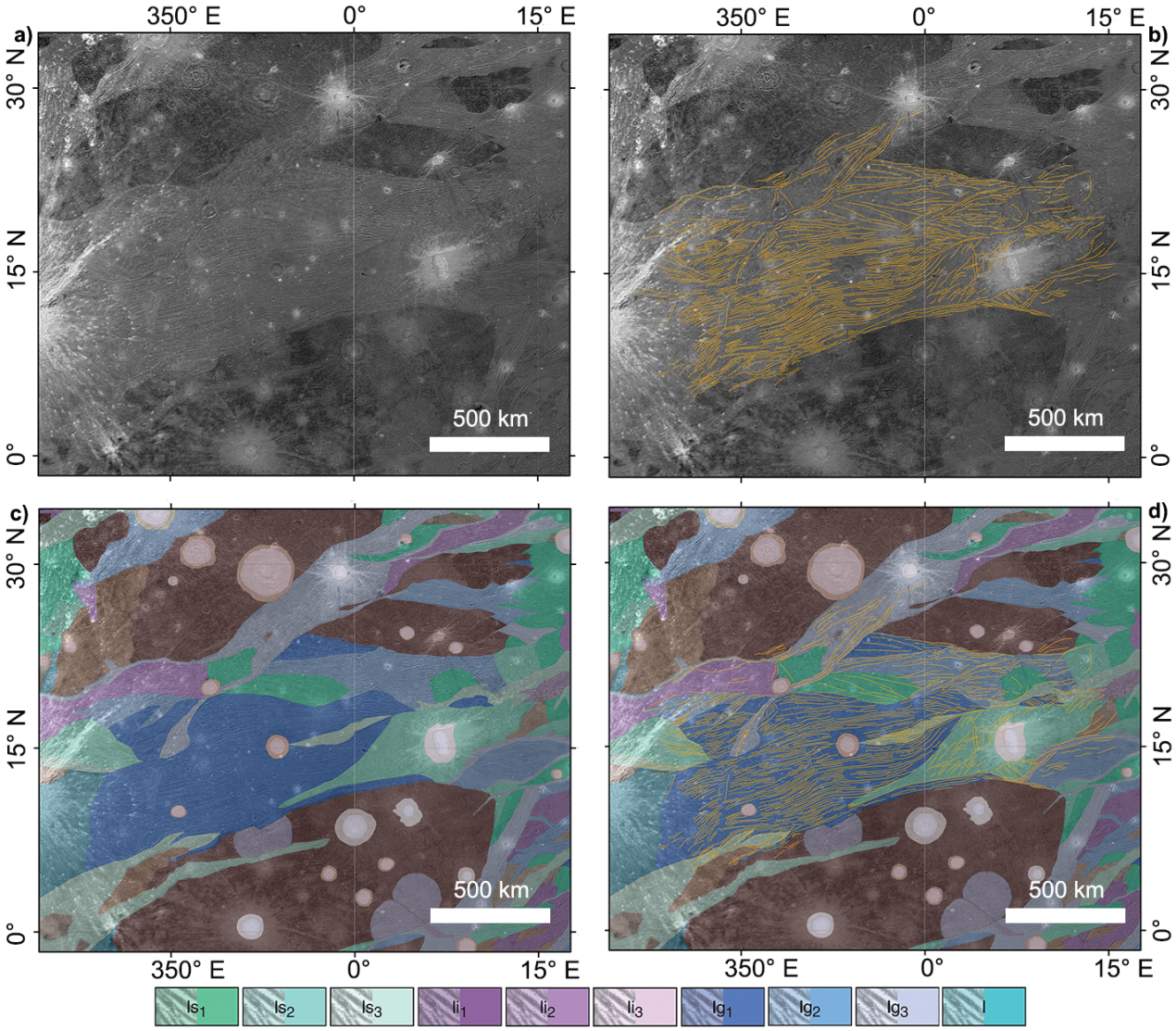

Figure 4: Grooves selected in Phrygia Sulcus area in the region centered at 15°N, 355°E. A) Ganymede base map (Ganymede Voyager - Galileo SSI Global Mosaic Ganymede, available at https://astrogeology.usgs.gov) representing the area of Phrygia Sulcus under study. B) The number of grooves mapped (Rossi et al., 2020) and selected for the analysis is 678. C) The geological map of Collins et al., (2013) overlaid in transparency on the base map. D) The grooves mapped are represented overlaid on the geological map. The legend represents the geological units corresponding to the light terrains on which grooves were mapped (light subdued unit: *ls1*, *ls2*, *ls3*, light irregular unit: *li1*, *li2*, *li3*, light grooved unit: *lg1*, *lg2*, *lg3* and light undivided unit *l*). For nomenclature and interpretation of the geological units, we refer the reader to Collins et al., (2013).

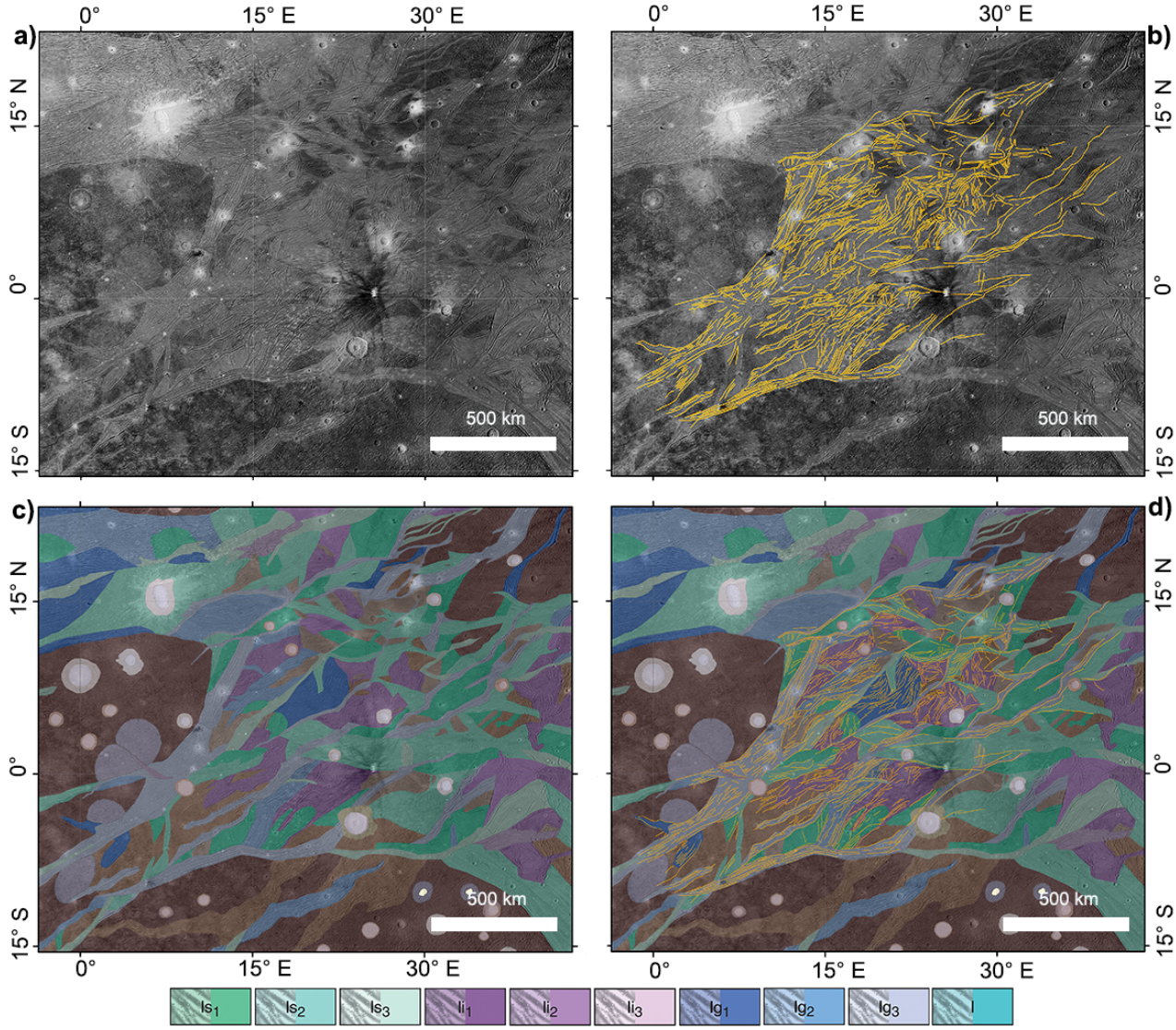

Figure 5: Grooves selected in Mysia Sulci area in the region centered at 7°N, 20°E. A) Ganymede base map (Ganymede Voyager - Galileo SSI Global Mosaic Ganymede, available at https://astrogeology.usgs.gov) representing the area of Mysia Sulci under study. B) The number of grooves mapped (Rossi et al., 2020) and selected for the analysis is 987. C) The geological map of Collins et al., (2013) overlaid in transparency on the base map. D) The grooves mapped are represented overlaid on the geological map. The legend represents the geological units corresponding to the light terrain on which grooves were mapped (light subdued unit: *ls1, ls2, ls3,* light irregular unit: *li1, li2, li3,* light grooved unit: *lg1, lg2, lg3* and light undivided unit *l*). For nomenclature and interpretation of the geological units, we refer the reader to Collins et al., (2013).

3. Methods

Fault populations statistic can be analysed in terms of its size and spatial distribution (e.g., Soliva and Schultz, 2008; Schultz et al., 2010; Mazzarini et al., 2013; Lucchetti et al., 2017). Size distribution focuses on the properties of geometric features such as fault length, spacing and displacement, while spatial distribution investigates the properties of the whole population such as fault density and spatial clustering. We here report the two approaches used in this work to analyse Ganymede's grooves.

3.1 Length Distribution analysis

The propagation and possible depth's confinement of a fault system is usually explored by the analysis of length distribution (e.g. Soliva and Schultz, 2008; Schultz et al., 2010; Mohajeri and Gudmundsson, 2012; Gudmundsson et al., 2013) that usually follow two different trends: negative exponential law distribution and negative power law distribution. The first one is represented by the following equation:

$$N(>l) = \beta e^{-\lambda l},$$

where $N(>l)$ is the number of faults whose length is longer than l, β and λ are the parameters of the exponential distribution and l the fault length, while the second one is represented by:

$$N(>l) = cl^{-\alpha},$$

where $N(>l)$ is the number of faults whose length is longer than l, c is the scaling factor, α the exponent of the power-law distribution and l is the fault length.

The mechanical layering of the crust, as well as a sufficiently large rheology contrast in material properties existing between layers, governs the vertical dimension of a fault (height) that is, in turn, nearly proportional to fault length (e.g., Benedicto et al., 2003; Gudmundsson et al., 2010; Soliva and Schultz, 2008). In this scenario, analysis of faults' length distribution usually identifies two end-members (e.g., Soliva and Schultz, 2008; Schultz et al., 2010): (i) fault populations of regularly spaced faults derived from strain partitioning within a single mechanical layer are confined in depth and are generally characterized by negative exponential distribution (e.g., Cowie et al., 1994;

232 Ackermann et al., 2001); (ii) fault systems, with few large well separated faults cutting across the
233 whole crust displaying a negative power-law distribution.
234 Planetary crusts often record long tectonic evolution, leading to complex structural settings indicating
235 multiple activation of former inherited structures as well as complex internal strain partitioning (Rossi
236 et al., 2018). This means that fractures formed at different stages of the whole deformation history
237 may respond to different fault length size distributions.
238
239 **3.2 Self-similar Clustering analysis**
240 A robust way to define how fractures (sensu National Research Council, 1996) fill space (i.e. fracture
241 spatial distribution) is to analyse their self-similar clustering (Bonnet et al., 2001). Through this
242 methodology it is possible to infer the vertical extension of the connected fractures network starting
243 from the observation of fractures and, then to evaluate the scaling properties of the system (Mazzarini
244 and Isola, 2010). The self-similar clustering of fractures is performed for a range of lengths (the size
245 range) between a lower and an upper cutoff (L_{co} and U_{co}, respectively) by applying the two-point
246 correlation function method to measure the fractal dimension of the fracture population.
247 For a population of N points (fracture's trace barycenter) the correlation integral *C(l)* is defined
248 as the correlation sum that accounts for all the points at a distance of less than a given length *l*
249 (Hentschel and Procaccia, 1983) by the following equation:
250 $C(l)=2N(l)/N(N-1)$,
251 where *N(l)* is the number of pairs of points whose distance is less than *l*. The self-similar clustering
252 exists if the following scaling law is satisfied:
253 $C(l) \sim l^D$,
254 where *D* is the fractal exponent defined as the slope of the tangent to the *log(C(l)) vs. log(l)* curve.
255 A higher value of the *D* exponent implies a more homogeneous distribution of fractures, while a
256 lower value of the *D* exponent means a higher fracture clustering (Figure 6).

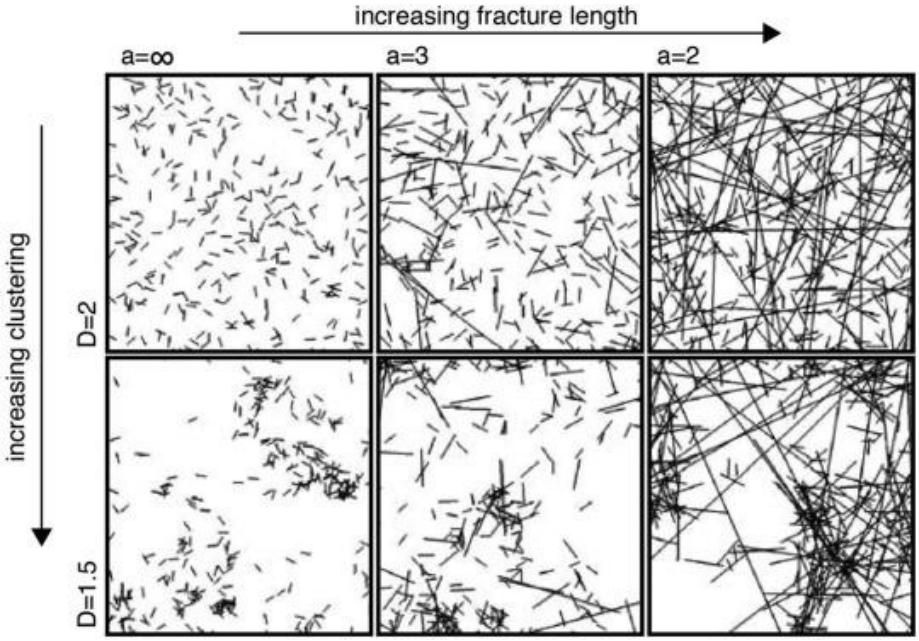

Figure 6: Simulations representing network connectivity controlled by fracture length and clustering. The parameters reported in the figure are the fractal exponent *D*, that controls the degree of self-similar clustering (D = 2 weakly clustered; D = 1.5 strongly clustered) and *a*, that controls the power-law distribution for fracture length (increasing lengths from a = ∞ -short- to a = 2 -long-). Adapted from Darcel et al. (2003) and Mazzarini and Isola, 2010.

The local slope is a point by point measure of the slope of the tangent to the curve):

local slope = $\Delta log(C(l))/\Delta log(l)$.

Self-similarity exists within a size range, bounded by a L_{co} and a U_{co}, and it is detectable as a linear fit (a plateau) in a *local slope* diagram: when the range is wider, the computation of the power-law distribution is better (Walsh and Watterson, 1993).

L_{co} and U_{co} are scale-invariant characteristics of fractures depending on both the resolution of the images used to map and detect fractures (L_{co}) and the mechanical layers and rock/ice properties (U_{co}) (Mandelbrot et al., 1982). Indeed, it has been validated that the thickness of the fractured/deformed layer is mirrored by the occurrence of a threshold value (U_{co}) in the size of the fracture network spatial organization (Pacheco et al., 1992; Davy, 1993; Ouillon et al., 1996; Mazzarini and D'Orazio, 2003;

Mazzarini and Isola, 2010; Gudmundsson et al., 2010; Gudmundsson et al., 2011, Mazzarini et al., 2013).

The derivation of the cut-offs defining the size range is not trivial, especially when the local slope does not show a regular and wide plateau. The choice of L_{co} and U_{co} was estimated by selecting the wider length range for which the correlation between *Log(C(l)) vs Log(l)* is greatest by applying the ordinary least squares fit method (Mazzarini, 2004). By knowing that the fractal behaviour is valid until a significant break in the local slope occurs, we estimate the R^2 value corresponding to the breaking point.

4. Results and Discussion

We analysed the mapped faults following the methodology explained in the previous section. Firstly, we obtained the length-frequency histograms for the faults of each analysed region, as shown in Fig. 6A-D.

The minimum and maximum length of the 1068 faults located in Uruk Sulcus are 0.47 km and 582 km, respectively. The mean is 62.7 km while the median length is 48 km (Figure 7A). The faults length size range for Babylon Sulci is between 7.2 and 656 km with a mean and a median length of 77.8 km and 57.9 km, respectively (Figure 7B). Phrygia Sulcus is characterized by a range size of 8.9 - 559 km and a mean and median length of 95.9 and 72.1 km, respectively (Figure 7C). The minimum and maximum length of Mysia Sulci are 6.5 and 496 km with an associated mean and median length of 66 km and 47 km (Figure 7D). As outlined in the histograms, there is a small number of faults with length < 20 km. This suggests that our datasets may be affected by truncation bias and implies that relatively short faults were hardly detectable on a regional scale with the present day available satellite images. Indeed, faults analyses are usually characterised by the presence of an upper and a lower bias affecting the measurements. The first is referred to as “censoring”, which occurs when the sample size exceeds the dimensions of the measurement area, hence implying the

underestimation of the sample size. On the other hand, the second is known as "truncation" and it is related to the image resolution that may lead to small samples undercounting (Bonnet et al., 2001).

After calculating the statistical attributes of faults, we obtained the length cumulative plot for each faults' network (Figure 7E-H). This analysis reveals that such distribution is characterized by different fitting curves. Indeed, the cumulative plot presents a single or multiple exponential distributions for lengths shorter than L_{th} (length threshold), while there is a power-law distribution for faults longer than L_{th}. The presence of both the exponential and power-law trends reflect the possible coexistence of (i) distributed fault systems, with strain regularly partitioned along evenly spaced faults and confined within specific layers in the crust with different mechanical properties (exponential fitting curve/curves) and (ii) localized fault systems, with few large faults cutting across the whole crust (power-law fitting curve) (e.g., Soliva and Schultz, 2008; Schultz et al., 2010). In addition, the existence of two exponential distributions for three datasets suggest that there could be two differently confined structure systems within specific mechanical crust layers.

We underline that, even if the number of samples (from 50 up to 200) fitted by a power-law is not as numerous as the ones characterized by the exponential fitting, we are confident about such distribution. Indeed, it is well known that even if the data follow a power-law distribution, it does not mean that the power-law necessarily provides the best model or fit for the data (Clauset et al., 2009; Mohajeri and Gudmundsson, 2012). For this reason, we tested the power-law distribution using the program Matlab and the statistical programing language R following the procedure of Clauset et al., (2009) (see Supplementary Material). This approach validates the existence of the power-law distribution, confirming the presence of a L_{th} separating the exponential and the power-law fitting models. The L_{th} is 93.8 km, 148 km, 238.7 km, 185 km for Uruk Sulcus, Babylon Sulci, Phrygia Sulcus and Mysia Sulci, respectively. The calculated distribution for each dataset is reported in Table 1.

These findings may represent the evolutional history of fault linkages underlying the Ganymede surface, where the transition between the exponential and power-law length-frequency

distributions is connected to the fault growth in a vertically confined medium. The faults (i.e. grooves) exponential behaviour is representative of both the nucleation of new faults during incipient phases of propagation (when mechanical layering does not have any influence) and the saturation of a vertical confined system of structures (Schultz et al., 2010; Cowie et al., 1994; Ackermann et al., 2001). On the contrary, the interaction of faults and the consequent linkage/growth process dominates over the nucleation of new faults providing a power-law distribution (Cowie et al., 1995).

Dataset	N	l range (km)	l_{th} (km)	Distribution (N>l)		
				Exponential ($l<l_{th}$)		Power-law ($l>l_{th}$)
Uruk Sulcus	1068	0.47 - 582	93.8	$\propto e^{-0.47\,l}$ $R^2 = 0.989$ N = 798		$\propto l^{-2.66}$ $R^2 = 0.998$ N = 194
Babylon Sulci	882	7.2 – 646	148	$\propto e^{-0.48\,l}$ $R^2 = 0.991$ (l < 80km) N = 536	$\propto e^{-0.37\,l}$ $R^2 = 0.994$ (l > 80km) N = 201	$\propto l^{-2.96}$ $R^2 = 0.996$ N = 97
Phrygia Sulcus	678	8.9 – 559	238.7	$\propto e^{-0.52\,l}$ $R^2 = 0.992$ (l < 140km) N = 525	$\propto e^{-0.2\,l}$ $R^2 = 0.993$ (l > 140km) N = 73	$\propto l^{-4.35}$ $R^2 = 0.986$ N = 46
Mysia Sulci	987	6.5 – 496	185	$\propto e^{-0.51\,l}$ $R^2 = 0.989$ (l < 90km) N = 688	$\propto e^{-0.22\,l}$ $R^2 = 0.985$ (l > 90km) N = 121	$\propto l^{-3.46}$ $R^2 = 0.992$ N = 56

Table 1: Parameters for each length size distribution of the selected area, where *N* is the total number of faults, *l range* is defined between the minimum and maximum length value in km and l_{th} the threshold length value discerning between the exponential and power-law distribution of length's faults. The last two columns reported the exponential and power-law fitting models found for the selected region, as shown in Figure 7.

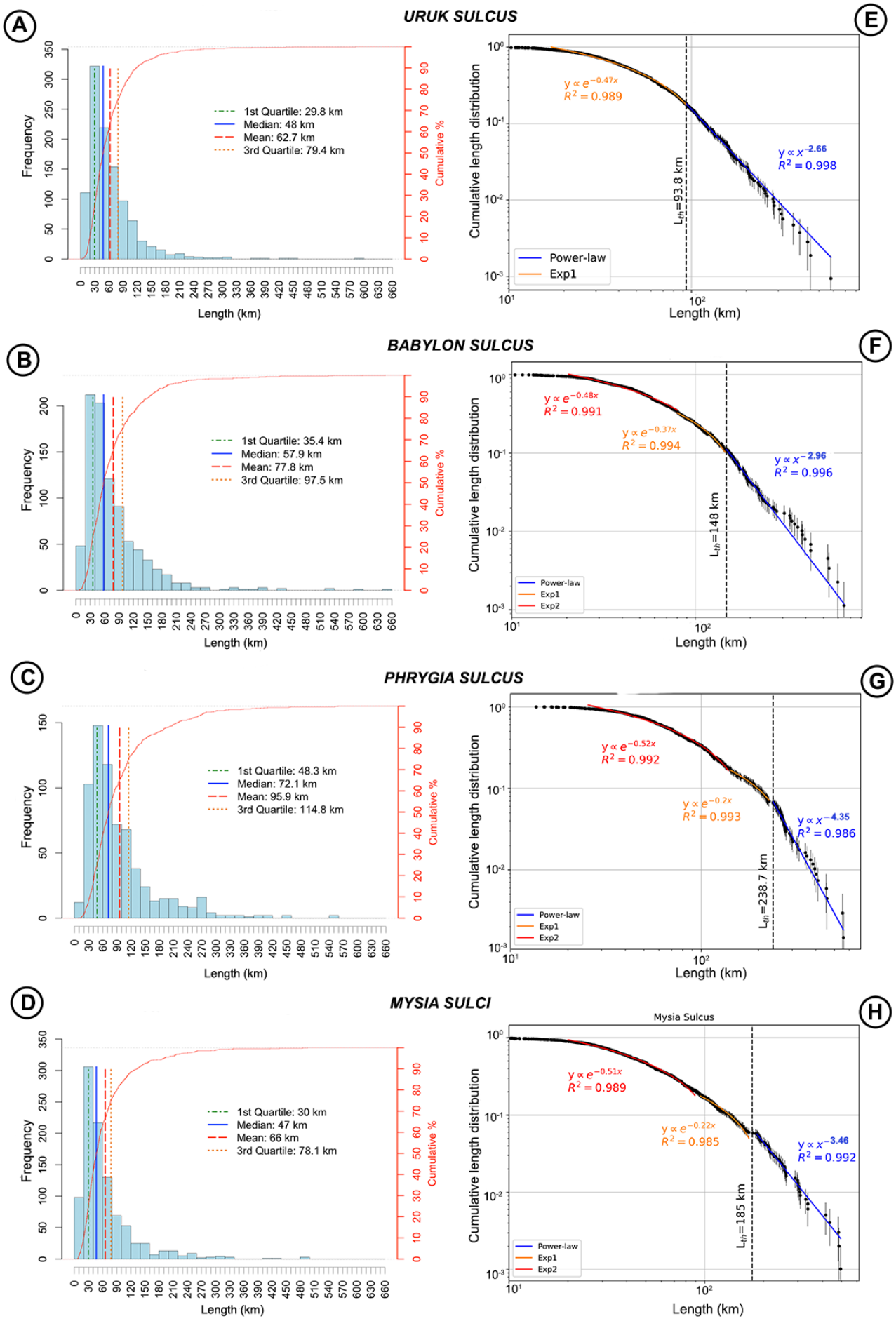
A
URUK SULCUS
E
Frequency
Cumulative %
1st Quartile: 29.8 km
Median: 48 km
Mean: 62.7 km
3rd Quartile: 79.4 km
Length (km)
Cumulative length distribution
$y \propto e^{-0.47x}$
$R^2 = 0.989$
$y \propto x^{-2.66}$
$R^2 = 0.998$
L_{th}=93.8 km
Power-law
Exp1
Length (km)
B
BABYLON SULCUS
F
1st Quartile: 35.4 km
Median: 57.9 km
Mean: 77.8 km
3rd Quartile: 97.5 km
$y \propto e^{-0.48x}$
$R^2 = 0.991$
$y \propto e^{-0.37x}$
$R^2 = 0.994$
$y \propto x^{-2.96}$
$R^2 = 0.996$
L_{th}=148 km
Power-law
Exp1
Exp2
C
PHRYGIA SULCUS
G
1st Quartile: 48.3 km
Median: 72.1 km
Mean: 95.9 km
3rd Quartile: 114.8 km
$y \propto e^{-0.52x}$
$R^2 = 0.992$
$y \propto e^{-0.2x}$
$R^2 = 0.993$
$y \propto x^{-4.35}$
$R^2 = 0.986$
L_{th}=238.7 km
D
MYSIA SULCI
H
Mysia Sulcus
1st Quartile: 30 km
Median: 47 km
Mean: 66 km
3rd Quartile: 78.1 km
$y \propto e^{-0.51x}$
$R^2 = 0.989$
$y \propto e^{-0.22x}$
$R^2 = 0.985$
$y \propto x^{-3.46}$
$R^2 = 0.992$
L_{th}=185 km

Figure 7: Length distribution analysis of A) Uruk Sulcus, B) Babylon Sulci, C) Phrygia Sulcus and D) Mysia Sulci. On the left column the length histograms (bin size =15 km) are reported, while on the right column the length cumulative plots for each dataset are presented. The statistical attributes, such 1st quartile, median, mean and 3rd quartile values, are defined for each histogram plot and outlined by green, blue, red and orange lines, respectively. The fitting models of cumulative length distribution are shown on the graphs (E-H) and reported in Table 1. Faults shorter than the threshold length L_{th} (black dashed line) are fitted by exponential distributions (red and orange curves), while faults longer than L_{th} are fitted by a power-law distribution (blue curve).

The self-similar clustering analysis indicates that the spatial organization of faults in each data sets is bounded in a size range with a well-defined upper cutoff. The plateau in the fractal distribution has been inferred from the analysis of the *Log(C(l)) vs Log(l)* diagram (Bonnet et al., 2001, Figure 8) and its validity is bounded by a size range (L_{co} and U_{co}) detectable as a linear fit (plateau) in the *local slope vs Log(l)* diagram (Walsh and Watterson, 1993, Figure 8). The choice of L_{co} and U_{co} was estimated by selecting the wider length range for which the linear correlation between *Log(C(l))* and *Log(l)* (black points in Figure 8) is greatest, by applying the ordinary least squares fit method. Hence, the quality of the correlation was assessed using the coefficient of R^2 determination detecting the size range corresponding to the higher value of R^2. To ensure the reliability of the results, we also cross check the *local slope vs Log(l)* (green points in Figure 8) diagram with R^2 values for all possible size range combination *ΔLog(l)*. Higher R^2 value results in higher reliability of the information. Hence, we detected the depth range corresponding to the higher values of R^2, thus describing the values of best-fit for the U_{co}, validating the robustness of the U_{co} estimates. Moreover, the large number of samples used ensures robust estimates of the parameters with an error < 1% (as reported in Mazzarini and Isola 2010). Nevertheless, the L_{co} is very sensitive to the measurement truncation bias, which is in turn correlated with the image resolution. Given that the plateau is rather noisy close to the L_{co}, we do not attribute a reliable significance on it. This is also supported by the fact that the histograms

(Figure 7) show a small number of short faults due to the truncation bias mentioned above. On the other hand, the U_{co} (i.e. the highest plateau breaking point) is defined by the maximum value of the size range and it is easily recognizable by a slope break in all considered grooves systems (Figure 8).

The fractal analysis applied on all study areas show a clear plateau in the diagrams (Figure 8), hence providing the identification of the size range where the fractal behaviour is valid. A size interval for both the L_{co} and U_{co} have been outlined through gray bands on Figure 8 and reported in Table 2. Uruk Sulcus reveals a fractal behaviour between 9-11 km and 105-120 km (Figure 8A), Babylon Sulci between 10-13 km and 115-130 km (Figure 8B), Phrygia Sulcus between 10-13 km and 115-130 km (Figure 8C), and Mysia Sulci between 10-13 km and 110-125 km (Figure 8D). As stated above, the values found for L_{co} are not reliable due to the noisy data. On the contrary, the values of U_{co} are reliable and comparable for all datasets. The U_{co} is the vertical maximum extension of the connected grooves network (Mazzarini and Isola, 2010, Mazzarini et al., 2013) and, hence, it is directly linked to the mechanical layering of the medium. This analysis reveals that this vertical extension ranges between 105 and 130 km for the four equatorial regions considered. Moreover, this suggests that this limit might be the potential thickness of the icy crust located above the deep ocean that during a phase of intense deformation and high strain rates may be cut across by very large faults.

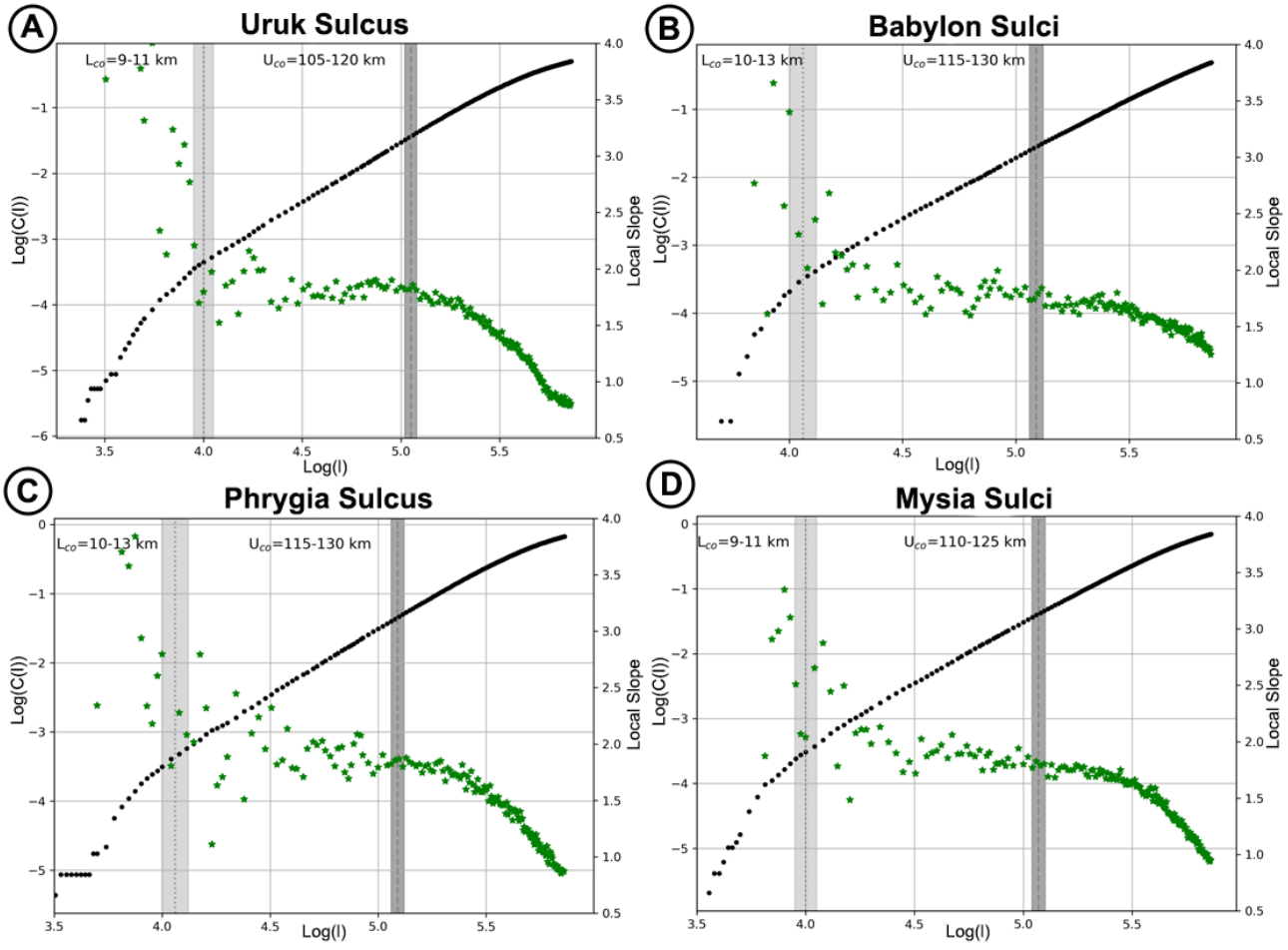

Figure 8: Self-similar clustering analysis for A) Uruk Sulcus, B) Babylon Sulci, C) Phrygia Sulcus and D) Mysia Sulci. For each dataset, it is reported the log plot of *C(l) vs l* (black points) and the *local slope vs Log(l)* plot (green points). The size range of interconnected faults are represented by the plateau stage of the local slope curve (green points). The gray stripes are the L_{co} and U_{co} intervals that define the size range of the fractal distribution. The slope of the curve (black points) is the fractal exponent *D* computed in the size range L_{co} - U_{co}. The distribution stops to be fractal when the local slope curve (green points) breaks. The breaking point may correspond to a *Log(l)* value (U_{co}) that represents the potential thickness of the icy crust above the deep ocean required for the development of densely populated structures at the surface (i.e. the grooves). U_{co} ranges between 105 km and 130 km, when considering all fault system analysed.

Dataset	Longitude	Latitude	N	D	R^2	U_{co}(km)
Uruk Sulcus	185°E - 220°E	15°S - 20°N	1068	1.877± 0.03	0.999	105-120
Babylon Sulci	260°E - 320°E	20°S - 15°N	882	1.847 ± 0.03	0.9991	115-130
Phrygia Sulcus	340°E - 15°E	5°N - 30°N	987	1.945 ± 0.01	0.9997	115-130
Mysia Sulci	10°E - 40°E	10°S - 20°N	678	1.95 ± 0.02	0.9991	110-125

Table 2: Parameters of spatial distribution analysis (self-similar clustering) of faults for each selected area with associated latitude and longitude range. *N* is the number of faults, *D* the fractal exponent of fractures self-similar clustering, R^2 the goodness of fit and U_{co} the upper cut-off.

We highlight that few grooves reaching this maximum depth (identified as U_{co}) are expected, while a larger number remain confined at much shallower depths, as suggested by the length distribution analysis reported above. Noteworthy, in all four data sets the faults fractal distribution is characterized by a well-defined single plateau, suggesting that the strain redistribution at the scale of the whole crust occurs by a hierarchical fracture network where few large faults control and distribute the crustal strain. Indeed, the large faults (i.e. grooves) characterised by the power-law fitting behaviour can be considered as crustal-scale structures, typically with a strike slip component (as shown in Cameron et al., 2018; Rossi et al., 2018) that localizes and accommodates most of the crustal strain. Specifically, these large structures can theoretically reach the crust-ocean interface. On the contrary, the shorter faults populations (exponentially-fitted) may act as confined structures as response to lower strain.

We underline that time evolution of faults cannot be retrieved by using self-similar clustering, which is representative of the whole deformation that interested the icy crust through time. Indeed, what we observe is that the actual fracture network presents a fractal behaviour, consistent with an actual mechanical stratigraphy. Hypothetically, we may forward that the main initial deformation of the crust occurred via large faults cutting across the whole crust thickness down to the crust-ocean

transition. With time, minor deformation provided the development of exponential distribution of fault cutting across the crust down to the brittle-ductile transition.

The vertical profile of the faults is expected to behave similarly to the Earth faults that become less tilted with the increase of the depth. Indeed, faults gradually transit from sharp geometries to gentle ones when plastic deformation zones are reached at depth. Faults (i.e. grooves) are suggested to be originated by extension and strike-slip regimes that imply different development at depth. On Earth, and hence on the icy crust of Ganymede, extensional deformation creates faults with high dip angle (ideally 60°) that can decrease up to sub-horizontal (i.e. listric faults, e.g. Walsh and Watterson, 1991). On the other hand, strike-slip activity form nearly vertical faults that reach high depths (e.g. Fossen, 2016). In this context, we suggest that the strike-slip faults represent the faults that penetrate deeper and follow the power-law behavior described by our analyses, by potentially reaching the bottom of the icy crust; while the extensional faults are represented by the shorter faults with exponential behavior, that remain at the top layers of the icy crust. It is possible that some of them could assume listric shape at the occurrence of ductile layers and cease to vertically develop at such depth.

In this context, it is also appropriate to clearly state that some extensional faults may show a power-law behavior and penetrate at high depth, and, vice-versa, some strike-slip faults can show exponential behavior by reaching shallow depths.

We expect exponentially-fitted length distribution grooves to be confined within the brittle portion of the crust, in particular when considering crustal rifting modes affecting the opening of the lithosphere in earlier Ganymede history (Pizzi et al., 2019), i.e. when the icy crust was thought to be thinner and most of the faults' nucleation took place. Moreover, the vertical extent of the second order structures may be controlled by necking instability (i.e. modelling Ganymede's lithosphere as a brittle surface layer underlain by a viscous half-space) occurring in Ganymede crust at shallow depth at 10^{-13} s^{-1} strain rate, as suggested by finite element method (FEM) simulations (e.g., Bland and Showman,

2007). However, the progressive thickening of Ganymede crust through time and the possible effects due to tidal stress (Cameron et al., 2019) may have contributed in localizing the strain within few large pre-existing structures, that may have recurrently reactivated, hence cross-cutting the entire crust.

The spatial distribution analysis shows that only a relatively small number of faults is able to penetrate the icy crust. Being, most of the longer structures recognized as the boundaries of strike-slip corridors often delimiting the transition between the dark and light terrains, they represent the lead candidates that could have penetrated the entire icy crust. On the other hand, since our data are affected by truncation bias and the analysis has been performed at a regional scale, we cannot infer about the behaviour of shorter faults nor observe the surface deformation of shorter structures induced by tidal stresses (Cameron et al., 2019).

The general framework presented above may suggest two possible tectonic scenarios for faults (i.e grooves) development: i) synchronous extension and strike-slip activities through time or ii) two distinct evolutionary phases with extension, followed by strike-slip faulting. The occurrence of a single plateau in all datasets could support the first tectonic scenario as the more plausible one. Nevertheless, to fully confirm one scenario over the other, a dedicated structural investigation at higher spatial resolution is needed.

The interpretation of few long faults propagating down to the liquid ocean is supported by the values of U_{co} (ranging between 105 and 130 km). Such values agree with independent estimates of Ganymede icy layer thickness. Through the interpretation of Galileo magnetic data, Kivelson et al., (2002) suggested the presence of a conducting layer at a depth of 150 km below the icy crust. Later, Saur et al., (2015) stated the presence of a saline conductive ocean at a depth of 150 km through the observation and modelling of Ganymede's auroral ovals dynamics. On the other hand, Schenk et

al., (2002) provides an estimate of at least 80 km for the icy shell thickness by analysing the transition between depth to diameter ratio of large impact craters.

To summarize, we found that (i) the grooves are the representation of a hierarchical system constituted by second order structures controlled by the rheological layering of the crust (i.e. faults fitted by exponential length distribution) and few major crustal-scale structures (i.e. faults fitted by power-law distribution) with possible prevalence of strike-slip kinematics, (ii) the occurrence of large first order tectonic structures cutting the whole icy crust that (even if limited in number) may control the crustal strain distribution and (iii) the presence of icy solid crust above the liquid ocean with thickness of 100-130 km along the equatorial belt of Ganymede which is in agreement with previous measurements.

5. Conclusion

In this work we analysed the length size-distribution and self-similar clustering of Ganymede's groove populations to estimate the potential thickness of the icy crust above the deep ocean and potential mechanical layering within the crust. Grooves (i.e. faults) represent the evidence of tectonic activity that deformed the surface of Ganymede during its geologic evolution and characterize the light material unit of the satellite. Specifically, we investigated four regions located on the Ganymede equatorial area by using the regional scale grooves mapping performed by Rossi et al., (2020). The four chosen datasets are selected from regions in Uruk Sulcus, Babylon Sulci, Phrygia Sulcus and Mysia Sulci centered at 0.8°N, 200°E, 0°N, 290°E, 15°N, 355°E and 7°N, 20°E and containing 1068, 882, 678 and 987 faults, respectively. On such datasets, we firstly performed a length distribution analysis to describe the depth propagation and growing evolution of the faults underlying grooves systems. Then, we investigated the faults spatial distribution (self-similar

clustering) in order to infer the vertical extension of the connected fractures network and, hence, evaluate the scaling properties of the system.

We found that the faults length distribution change from exponential (shorter faults) to power-law (longer faults) at a threshold length of 93.8 km, 148 km, 238.7 km, 185 km for Uruk Sulcus, Babylon Sulci, Phrygia Sulcus and Mysia Sulci, respectively.

This means that the shorter, exponentially-fitted populations may act as confined structures, while the large grooves fitted by power-law curves can be considered as crustal-scale structures theoretically reaching the crust-ocean interface. From the self-similar clustering analysis, we estimated the potential thickness of the icy crust above the liquid ocean ranging between 105 and 130 km for the datasets considered. This value agrees with independent estimates of the thickness of the icy shell (from 80 to 150 km, Schenk et al., (2002); Kivelson et al., 2002; Saur et al., 2015). Hence, our results support the hypothesis of shorter structures vertically confined in layers with different mechanical properties within the icy crust and few very long faults propagating down to the liquid ocean underneath. The latter are likely underlying the longer grooves often associated to strike slip kinematics at the dark/light terrain boundaries, thus representing important targets in the future Ganymede exploration as potential sites of surface-ocean connections.

The structural approach used in our analysis provides new insights into the depth of faults underlying grooves and the mechanical/rheological layering of Ganymede crust. In particular, we support the that the thickness of the Ganymede's icy crust ranges between 100 km and 130 km, which may be suggested as the depth at which a liquid water ocean is located.

Once future mission data will be available, this investigation will be largely improved with new measurements and analysis performed at mid and high latitudes. In particular, the upcoming ESA JUICE (Jupiter ICy moons Explorer, Grasset et al., 2013) mission will provide a global coverage of the surface of Ganymede with an average resolution of 100-150 m/px thanks to the JANUS camera (Jovis, Amorum ac Natorum Undique Scrutator, Palumbo et al., 2014). This instrument will provide

the possibility to easily detect grooves and related faults and fractures over the full body. Such images, coupled with digital terrain models will be pivotal to improve the knowledge of the satellite and will provide new insights into the formation and evolution of Ganymede grooves system.

In addition, the methodology presented in this work can be also applied to other icy bodies hosting a liquid ocean being interesting target for astrobiology, such as Europa (Kereszturi and Keszthelyi, 2013; Silber and Johnson, 2017; Domagal-Goldman et al., 2016).

Data availability

Data used in this work are those published by Rossi et al., (2020).

Acknowledgments

The activity has been realized under the ASI-INAF contract 2018-25-HH.0. This manuscript is part of a project that has received funding from the European Union's Horizon 2020 research and innovation programme under grant agreement Nº776276 (PLANMAP). We made use of the ArcGIS 10.5, Matlab and R softwares to perform the presented analysis.

References

Ackermann, R.V., et al., 2001. The geometric and statistical evolution of normal fault systems: An experimental study of the effects of mechanical layer thickness on scaling laws: Journal of Structural Geology, v. 23, p. 1803–1819, doi: 10.1016/S0191-8141(01)00028-1.

Anderson, J. Det al., 2001. Shape, mean radius, gravity field and interior structure of Ganymede. In *Bulletin of the American Astronomical Society* (Vol. 33, p. 1101).

Allison, M.L, Clifford, S. M., 1987. Ice-covered water volcanism on Ganymede. J. Geophys. Res., 92(B8), 7865-7876.

Becker, T. et al., 2001. Final digital global maps of Ganymede, Europa, and Callisto. Lunar Planet. Sci. Conf. XXXII, 2009.

543 Belton, M. J. S., et al., 1992. The Galileo solid-state imaging experiment. *Space Science*
544 *Reviews*, *60*(1-4), 413-455.
545 Belton, M. J. S., et al., 1996. Galileo's first images of Jupiter and the Galilean satellites. Science,
546 274(5286), 377.
547 Benedicto, A., et al., 2003. Layer thickness and shape of faults. Geophysical Research Letters, 30,
548 20, 2076, doi:10.1029/2003GL018237.
549 Bianchi, R., et al., 1984. Tectonics of the grooved terrain on Ganymede. Lunar and Planetary Science
550 Conference, 15, 54–55.
551 Bianchi, R., Casacchia, R., Lanciano, P., Pozio, S., & Strom, R. G., 1986. Tectonic framework of
552 grooved terrain on Ganymede. Icarus, *67*(2), 237-250.
553 Bland, M. T., Showman, A. P., 2007. The formation of Ganymede's grooved terrain: Numerical
554 modeling of extensional necking instabilities. Icarus, 189(2), 439-456.
555 Bonnet, E., et al., (2001), Scaling of fracture systems in geological media: Reviews of Geophysics,
556 v. 39, p. 347–383, doi: 10.1029/ 1999RG000074.
557 Bour, O., Davy, P., 1999. Clustering and size distribution of fault patterns: Theory and measurements:
558 Geophysical Research Letters, v. 26, p. 2001–2004, doi:10.1029/1999GL900419.
559 Bour, O., et al., 2002. A statistical scaling model for fracture network geometry, with validation on a
560 multiscale mapping of a joint network (Hornelen Basin, Norway): Journal of Geophysical
561 Research, v. 107, p. 2113, doi: 10.1029/2001JB000176.
562 Cameron, M.E., et al., 2018. Morphological mapping of Ganymede: Investigating the role of strike-
563 slip tectonics in the evolution of terrain types. Icarus 315, 92–114.
564 Cameron, M. E., et al., 2019. Tidal stress modeling of Ganymede: Strike-slip tectonism and Coulomb
565 failure. *Icarus*, *319*, 99-120.
566 Carr, M. H., et al., 1995. The Galileo Imaging Team plan for observing the satellites of Jupiter. J.
567 Geophys. Res. Planets, 100(E9), 18935-18955.

568 Casacchia, R., Strom, R. G., 1984. Geologic evolution of Galileo Regio, Ganymede. Lunar Planet.
569 Sci. Conf. XIV, 1028.
570 Clauset, A., et al., 2009. Power-law distributions in empirical data. *SIAM review*, *51*(4), 661-703.
571 Collins, G. C., et al., 2000. A global database of grooves and dark terrain on Ganymede, enabling
572 quantitative assessment of terrain features. Lunar Planet. Sci. Conf. XXXI, 1034.
573 Collins, G. C., 2009. The origin of grooved terrain on Ganymede. European Planetary Science
574 Congress, 4, 516.
575 Collins, G. C., et al., 2013. Global geologic map of Ganymede. US Department of the Interior, US
576 Geological Survey. doi:10.3133/sim3237.
577 Cowie, P. A., et al., 1994. Quantitative fault studies on the East Pacific Rise: A comparison of sonar
578 imaging techniques. *Journal of Geophysical Research: Solid Earth*, *99*(B8), 15205-15218.
579 Croft, S. K., Strom, R. G., 1985. Ganymede's crust: Structural indicators in the Tiamat Sulcus
580 quadrangle. Lunar Planet. Sci. Conf. XVI, 156-157.
581 Davy, P., 1993, On the frequency-length distribution of the San Andreas fault system: Journal of
582 Geophysical Research, v. 98, p. 12,141–12,151, doi:10.1029/93JB00372.
583 Domagal-Goldman, S. D., et al., 2016. The astrobiology primer v2. 0. Astrobiology, *16*(8), 561.
584 Dombard, A. J., McKinnon, W. B., 2001. Formation of grooved terrain on Ganymede: Extensional
585 instability mediated by cold, superplastic creep. Icarus, 154(2), 321-336.
586 Figueredo, P. H., et al., 1999. Fracture patterns on Ganymede and the initiation of tectonic
587 resurfacing. Lunar Planet. Sci. Conf. XXX, 1832.
588 Grasset, O., et al., 2013. JUpiter ICy moons Explorer (JUICE): An ESA mission to orbit Ganymede
589 and to characterise the Jupiter system. *Planetary and Space Science*, *78*, 1-21.
590 Gudmundsson, A., et al., 2010. Effects of internal structure and local stresses on fractyre propagation,
591 deflection and arrest in fault zones. Journal of Structural Geology, 32, 1643-1655.
592 Gudmundsson, A., 2011 Rock Fractures in Geological Processes. Cambridge University Press,
593 Cambridge, UK, pp 594.

Gudmundsson, A., Mohajeri, N., 2013. Relations between the scaling exponents, entropies, and energies of fracture networks. Bull. Géol. France, 2013, 184, 4, 377-387.

Gudmundsson, A., et al., 2013. Length-displacement scaling and fault growth. Tectonophysics, 608, 1298-1309.

Hargitai, H., & Kereszturi, Á. (Eds.), 2015. Encyclopedia of planetary landforms. Springer New York.

Head, J. W., et al., 2002. Evidence for Europa-like resurfacing styles on Ganymede. Geophys. Res. Lett. 29, 2151.

Hentschel, H. G. E., I. Proccacia, 1983. The infinite number of generalised dimensions of fractals and strange attractors, Physica D: Nonlinear Phenomena, 435-444.

Hirata, N., Suetsugu, R., & Ohtsuki, K., 2020. A global system of furrows on Ganymede indicative of their creation in a single impact event. *Icarus*, 113941.

Hussmann, H., et al., 2007. Interiors and evolution of icy satellites. In T. Spohn & G. Schubert (Eds.), Treatise on Geophysics. 10 (pp. 509–539).

Kereszturi, A., & Keszthelyi, Z., 2013. Astrobiological implications of chaos terrains on Europa to help targeting future missions. *Planetary and Space Science*, *77*, 74-90.

Kivelson, M.G., et al., 1997. The magnetic field and magnetosphere of Ganymede, Geophys. Res. Lett., 24, 2155-2158.

Kivelson, M. G., et al., 2002. The permanent and inductive magnetic moments of Ganymede. Icarus, 157(2), 507-522.

Kuskov, O. L., et al., 2010. Internal Structure of the Icy Satellites of Jupiter. In *Advances in Geosciences: Volume 19: Planetary Science (PS)* (pp. 365-376).

Lucchitta, B. K., 1980. Grooved terrain on Ganymede. Icarus, 44(2), 481-501.

Lucchetti, A., et al., 2017. Brittle ice shell thickness of Enceladus from fracture distribution analysis. *Icarus*, *297*, 252-264.

Mandelbrot, B.B., 1982, The Fractal Geometry of Nature: San Francisco, Freeman, 468 p.

620 Mazzarini F., D'Orazio, M., 2003. Spatial distribution of cones and satellite-detected lineaments in
621 the Pali Aike Volcanic Field (southernmost Patagonia): Insights into the tectonic setting of a
622 Neogene rift system: Journal of Volcanology and Geothermal Research, v. 125, p. 291–305, doi:
623 10.1016/S0377-0273(03)00120-3.
624 Mazzarini, F., 2004, Volcanic vent self-similar clustering and crustal thickness in the northern Main
625 Ethiopian Rift: Geophysical Research Letters, v. 31, p. L04604, doi: 10.1029/2003GL018574.
626 Mazzarini, F., Isola, I. 2010. Monogenetic vent self-similar clustering in extending continental crust:
627 Examples from the East African Rift System: Geosphere, v. 6, p. 567–582, doi: 10
628 .1130/GES00569 .1.
629 Mazzarini, F., et al., 2013 Spatial relationship between earthquakes and volcanic vents in the central-
630 northern Main Ethiopian Rift. *Journal of Volcanology and Geothermal Research* 262, 123–133.
631 McKinnon, W. B., Melosh, H. J., 1980. Evolution of planetary lithospheres: Evidence from
632 multiringed structures on Ganymede and Callisto. Icarus, 44(2), 454-471.
633 Mohajeri, N., and Gudmundsson, A., (2012). Entropies and Scaling Exponents of Street and Fracture
634 Networks. Entropy, 14, 800-833.
635 Moore, J. M., et al., 1999. Mass movement and landform degradation on the icy Galilean satellites:
636 Results of the Galileo nominal mission. Icarus, 140(2), 294-312.
637 Murchie, S. L., et al., 1986. Terrain types and local scale stratigraphy of grooved terrain on
638 Ganymede. Lunar Planet. Sci. Conf. Proceedings, 17.
639 Murchie, S. L., et al., 1989. Crater densities and crater ages of different terrain types on Ganymede.
640 Icarus, 81, 271-297.
641 Murchie, S. L., et al., 1990. Tectonic and volcanic evolution of dark terrain and its implications for
642 the internal structure and evolution of Ganymede. Journal of Geophysical Research: Solid Earth,
643 95(B7), 10743–10768. doi:10.1029/JB095iB07p10743.
644 National Research Council, 1996. Rock Fractures and Fluid Flow: Contemporary Understanding and
645 Applications. The National Academies Press, Washington, DC. https://doi.org/10.17226/2309.

646 Neukum, G., 1997. Bombardment history of the Jovian system. The Three Galileos: The Man, the
647 Spacecraft, the Telescope. Springer, Dordrecht, pp. 201–212.
648 Neukum, G., et al., 1998. Cratering chronology in the Jovian system and derivation of absolute ages.
649 Lunar Planet. Sci. Conf. XX IX, 1742.
650 Ouillon, G., et al., 1996. Hierarchical geometry of faulting: Journal of Geophysical Research, v. 101,
651 p. 5477–5487, doi:10.1029/95JB02242.
652 Pacheco, J.F., et al., 1992. Change in the frequency-size relationship from small to large earthquakes:
653 Nature, v. 355, p. 71–73, doi:10.1038/355071a0.
654 Palumbo, P., et al., 2014. JANUS: the visible camera onboard the ESA JUICE mission to the Jovian
655 system. In *EGU General Assembly Conference Abstracts* (Vol. 16).
656 Pappalardo, R. T., Greeley, R., 1995. A review of the origins of subparallel ridges and troughs:
657 Generalized morphological predictions from terrestrial models. J. Geophys. Res.: Planets,
658 100(E9), 18985-19007.
659 Pappalardo, R. T., et al., 1998. Grooved terrain on Ganymede: First results from Galileo high-
660 resolution imaging, Icarus, 135, 276-302.
661 Pappalardo, R. T., et al., 2004. Geology of Ganymede. Jupiter: Planet, Satellites, and Magnetosphere,
662 363-396.
663 Patterson, G. W., et al., 2010. Global geological mapping of Ganymede. Icarus, 207(2), 845- 867.
664 Pozzobon, R., et al., 2015. Self-similar clustering distribution of structural features on Ascraeus Mons
665 (Mars): implications for magma chamber depth. *Geological Society, London, Special*
666 *Publications*, *401*(1), 203-218.
667 Prockter, L. M., et al., 1998. Dark terrain on Ganymede: Geological mapping and interpretation of
668 Galileo Regio at high resolution. Icarus, 135(1), 317-344.
669 Prockter, L. M., et al., 2000. Geology and mapping of dark terrain on Ganymede and implications for
670 grooved terrain formation. J. Geophys. Res.: Planets, 105(E9), 22519-22540.

671 Rossi, C., et al., (2018). Evidence of transpressional tectonics on the Uruk Sulcus region,
672 Ganymede. *Tectonophysics*, *749*, 72-87.
673 Rossi, C., et al., (2020). Structural geology of Ganymede regional groove systems (60° N–60°
674 S). *Journal of Maps*, 1-11.
675 Russell, C. T. (Ed.), 2012. *The Galileo Mission*. Springer Science & Business Media.
676 Saur, J., et al., 2015. The search for a subsurface ocean in Ganymede with Hubble Space Telescope
677 observations of its auroral ovals. Journal of Geophysical Research: Space Physics, 120(3), 1715-
678 1737.
679 Schenk, P., McKinnon, W. B., 1987. Ring geometry on Ganymede and Callisto. Icarus, 72(1), 209–
680 234. doi:10. 1016/0019-1035(87)90126-6-
681 Schenk, P. et al., 2001. Flooding of Ganymede's bright terrains by low-viscosity water-ice lavas.
682 Nature, 410(6824), 57-60.
683 Schenk, P. M., 2002. Thickness constraints on the icy shells of the Galilean satellites from a
684 comparison of crater shapes. Nature 417, 419-421.
685 Schenk, P. M., et al., 2004. Ages and interiors: The cratering record of the Galilean satellites. Jupiter:
686 The planet, satellites and magnetosphere, 427-456.
687 Schultz, R.A., et al., 2010. Fault populationsons. In: *Planetary Tectonics*, edited by Thomas R.
688 Watters and Richard A. Schultz. Cambridge University Press, Cambridge, 457-510.
689 Shoemaker, E. M., et al., 1982. The geology of Ganymede. In Satellites of Jupiter, 1, 435-520.
690 Showman, A.P., et al., 2004. On the resurfacing of Ganymede by liquid water volcanism. Icarus 172,
691 625–640. doi: 10.1016/j.icarus.2004.07.011.
692 Silber, E. A., & Johnson, B. C., 2017. Impact crater morphology and the structure of Europa's ice
693 shell. Journal of Geophysical Research: Planets, *122*(12), 2685-2701.
694 Smith, B.A., et al., 1979a, The Jupiter system through the eyes of Voyager 1, Science, 204.
695 Smith, B. A., et al., 1979b. The Galilean satellites and Jupiter: Voyager 2 imaging science results.
696 Science, 206(4421), 927-950.

Sohl, F., et al., 2002. Implications from Galileo observations on the interior structure and chemistry of the Galilean satellites. *Icarus*, *157*(1), 104-119.

Soliva, R., Schultz, R.A., 2008. Distributed and localized faulting in extensional settings: Insight from the North Ethiopian Rift–Afar transition area. Tectonics, 27, TC2003, doi:10.1029/2007TC002148.

Walsh, J.J., Watterson, J., 1993. Fractal analysis of fracture pattern using the standard box-counting technique: Valid and invalid methodologies: Journal of Structural Geology, v. 15, p. 1509–1512, doi: 10.1016/0191- 8141(93)90010-8.

Zahnle, K., et al., 2003. Cratering rates in the outer Solar System. Icarus, 163(2). 263–289. doi:10.1016/S0019-1035(03)00048-4.

Declaration of Interest statement:

Padova, 11 May 2020

The Authors confirm that there are no interests to declare.

Alice Lucchetti

Digitally signed by Alice Lucchetti
Date: 2020.05.11 12:30:38 +02'00'

Alice Lucchetti on behalf of all Co-authors

CRediT author statement

Alice Lucchetti: Conceptualization, Methodology, Software, Investigation, Visualization, Formal analysis, Writing - original draft, , Writing - review & editing. **Costanza Rossi:** Investigation, Resources, Writing - Review & Editing **Francesco Mazzarini**: Methodology, Writing - Review & Editing. **Maurizio Pajola***:* Formal Analysis, Writing - Review & Editing. **Riccardo Pozzobon:** Writing - Review & Editing. **Matteo Massironi**: Writing - Review & Editing, Funding Acquisition. **Gabriele Cremonese:** Writing - Review & editing, Funding Acquisition.

Supplementary Files

Click here to access/download

Supplementary Material

Lucchetti_Ganymede_Supplementary_Material_11May.docx